

PhD Dissertation

Removal of CO₂ from flue-gas by innovative functionalized sorbents



Chemical Engineering–Cycle XXV

Dipartimento di Ingegneria Chimica,

dei Materiali e della Produzione Industriale

Università degli Studi di Napoli Federico II

Scientific Committee

Prof. Amedeo Lancia
Dr. Alessandro Erto
Dr. Fabio Montagnaro
Prof. Francisco Rodríguez-Reinoso

Thesis by

Marco Balsamo

Table of contents

CHAPTER 1 INTRODUCTION	4
CHAPTER 2 LITERATURE OVERVIEW	8
2.1 Utilization of activated carbons in CCS field	8
2.1.1 CO ₂ adsorption onto as-synthesized activated carbons	8
2.1.2 CO ₂ adsorption on functionalized activated carbons	10
2.2 Other classes of CO ₂ sorbents investigated	12
2.2.1 Zeolites	12
2.2.2 Ordered mesoporous silicas (OMS)	12
2.2.3 Calcium oxide	13
2.2.4 Metal-organic Frameworks (MOFs)	14
2.3 Ionic liquids (ILs)	15
2.3.1 ILs applications for CO ₂ capture	16
2.3.2 Functionalization of solids with ionic liquids (ILs)	17
CHAPTER 3 THEORETICAL FRAMEWORK OF THE ADSORPTION PROCESS	19
3.1 Adsorption equilibria	19
3.2 Dynamics of adsorption columns	21
CHAPTER 4 MATERIALS AND METHODS	28
4.1 Activated carbons, ionic liquids and impregnation protocols	28
4.2 Solids characterization techniques	29
4.2.1 CO ₂ /N ₂ porosimetric analyses	29
4.2.2 Thermogravimetric analyses (TGA)	30
4.3 Lab-scale plant for CO ₂ adsorption/regeneration tests	31
4.4 Experimental protocols for fixed bed dynamic experiments	33
4.4.1 Continuous CO ₂ adsorption tests	33
4.4.2 Adsorption/desorption cycles and regeneration tests	35
CHAPTER 5 RESULTS AND DISCUSSION	37
5.1 Adsorbents characterization	37
5.1.1 Porosimetric analyses for F600-900 raw and impregnated with [Hmim][BF ₄]/[Emim][Gly]	37
5.1.2 TGA analyses for F600-900 raw and impregnated with [Hmim][BF ₄]/[Emim][Gly]	41
5.1.3 Porosimetric analyses for N.RGC30 raw and impregnated with [Hmim][BF ₄]/[Emim][Gly]	43
5.1.4 TGA analyses for N.RGC30 raw and impregnated with [Hmim][BF ₄]/[Emim][Gly]	46

5.1.5 Comparison between TGA and porosimetric analyses for the investigated sorbents	48
5.2 CO ₂ capture performances on the investigated sorbents	51
5.2.1 CO ₂ adsorption tests onto raw F600-900 and N.RGC30	51
5.2.2 CO ₂ adsorption tests onto F600-900 raw and functionalized with [Hmim][BF ₄]/[Emim][Gly]	56
5.2.3 CO ₂ adsorption tests onto N.RGC30 raw and functionalized with [Hmim][BF ₄]/[Emim][Gly]	63
5.2.4 Intertwining among solids properties and CO ₂ capture performances	69
5.3 Adsorption/desorption cycles and regeneration experiments for F600-900 raw	73
5.4 Adsorption thermodynamics and kinetics modelling	79
5.4.1 Thermodynamic aspects	79
5.4.2 Kinetic aspects	86
CHAPTER 6 CONCLUSIONS AND FUTURE PERSPECTIVES	92
Bibliography	95

CHAPTER 1

INTRODUCTION

The increase in worldwide CO₂ emissions, mainly deriving from fossil fuels, is commonly believed to be among the main contributors to global warming (Metz et al., 2005; Figueroa et al., 2008). Currently, 85% of the global energy demand is supplied by fossil-fueled power plants accounting for about 40% of total CO₂ emissions (Yang et al., 2008). Nowadays, different options are available to mitigate CO₂ emissions deriving from power sector, including higher power generation efficiency, use of non-carbon fuels (hydrogen and renewable energy), development of new energy production systems, such as oxy-combustion and chemical-looping combustion, and the adoption of efficient technologies for CO₂ capture and storage (CCS) (Metz et al., 2005; Li and Fan, 2008).

The CCS approach has the potential to reduce overall mitigation costs and increase flexibility in achieving a reduction in greenhouse gas (GHG) emissions: according to the BLUE Map Scenario of the International Energy Agency (IEA), this route could contribute to a 19% cut in CO₂ emissions by 2050 (International Energy Agency (IEA), 2010). More specifically, CCS technologies involve the separation and concentration of CO₂ produced in large point sources, the transport of the gas to a suitable storage location and long term isolation from atmosphere (Metz et al., 2005). Main CO₂ sequestration routes include geological injection, ocean dump and mineral carbonation (Metz et al., 2005).

Three main technological pathways can be pursued for CO₂ capture from fossil-fueled power plants: post-combustion capture, pre-combustion capture and oxy-combustion (Figueroa et al., 2008; Li and Fan, 2008; Kanniche et al., 2010). Among them, post-combustion system has the greatest near-term potential for reducing GHG emissions, because it can be retrofitted to existing units thus providing a quicker solution to mitigate CO₂ environmental impacts (Figueroa et al., 2008; Lee et al., 2012). The main barrier to the implementation of this technology on industrial scale is related to the low thermodynamic driving force for CO₂ capture from flue-gas (gas partial pressure is usually less than 0.15 bar). Moreover, applying current state-of-the-art CO₂ separation processes (absorption, adsorption, membrane purification and cryogenic distillation) to existing coal-fired power plant would reduce the power generation capacity by roughly one-third (Figueroa et al., 2008). Post-combustion chemical absorption of CO₂ in aqueous amine solutions (mainly monoethanolamine, MEA) is the most widely used purification technology (Strube and Manfrida, 2011; Bröder and

Svendsen, 2012). The MEA process suffers many drawbacks related to the considerable amounts of thermal energy required for absorbent regeneration, the high equipment corrosion rate caused by contact with MEA solution and the solvent degradation caused by oxygen and oxygen-based compounds such as SO₂ and NO_x present in a typical flue-gas (Kittel et al., 2009; Strube and Manfrida, 2011). As a consequence of the aforementioned issues, several research groups are making great efforts to develop high-performance and cost-effective CO₂ advanced separation processes in order to accelerate the techno-economic feasibility of post-combustion capture systems.

In this scenario, adsorption seems to be a very promising technology, widely used for the treatment of gaseous and liquid effluents due to its potentially high removal efficiency and operating flexibility, general low maintenance costs and, if coupled with an effective regeneration process, for the absence of by-products (Abanades et al., 2004; Choi et al., 2009; Balsamo et al., 2010; Sayari et al., 2011; Sjostorm et al., 2011; Samanta et al., 2012; Balsamo et al., 2013). Many sorbents can be used on purpose either raw or functionalized. Activated carbons show high potentiality for application in CO₂ capture because they are generally less costly than other materials (e.g., ordered mesoporous silicas, metal organic frameworks, etc.) and have a complex structure characterized by high surface area and tunable porosity and surface properties (Marsh and Rodríguez-Reinoso, 2006; Whaby et al., 2010). In addition, carbon-based sorbents are easily regenerable allowing their use in processes such as pressure swing adsorption (PSA), temperature swing adsorption (TSA) and vacuum swing adsorption (VSA) (Gomes and Yee, 2002; Tlili et al., 2009). Despite these advantages, CO₂ removal performances and long-term stability of activated carbons under typical flue-gas conditions (CO₂ 1-15% by vol. and atmospheric pressure) have been poorly investigated.

Another widespread research line in the context of post-combustion purification systems concerns the investigation of ionic liquids (ILs) as innovative solvents for CO₂ capture. The ever-increasing interest for this class of compounds in different fields is justified by their unique characteristics such as extremely low vapor pressure, high thermo-chemical stability and tunable chemico-physical properties (Zhang et al., 2006a; Bourbigou et al., 2010; Hasib-ur-Rahman et al., 2010). In particular, the possibility of functionalizing ILs with basic groups (like amines) makes them very attractive for CO₂ capture processes (Zhang et al., 2011). Numerous literature studies are now focusing on the use of ILs supported on porous membranes in order to overcome the main limits in the industrial-scale application of ionic liquids for CO₂ capture, which are related to their high cost and viscosity (Hasib-ur-Rahman et al., 2010; Lemus et al., 2011; Kolding et al., 2012). Notwithstanding a huge number of

scientific papers deals with the utilization of different classes of ILs in CCS field, the following critical aspects can be highlighted:

- CO₂ absorption tests are generally carried out at high pressure and room temperature which are experimental conditions not representative of a real flue-gas;
- There is fragmentary information concerning the effect of confining ILs into nanoporous substrates, particularly activated carbons, on CO₂ capture performances with respect to their bulk solvent properties.

On the basis of the above-mentioned analysis, the aim of this work is to provide a contribution in elucidating CO₂ capture performances of ionic liquids supported on activated carbons characterized by different porosimetric properties. Specific thermodynamic and kinetic adsorption tests have been carried out on selected activated carbons, both as raw and impregnated with ILs at different concentrations. Experimental tests have been performed in a lab-scale reactor and under realistic operating conditions (e.g. typical flue-gas compositions and temperatures). Preliminary regeneration studies have been conducted on the sorbent which displayed the highest CO₂ capture capacity in order to determine its performances under consecutive adsorption-desorption cycles and assess the optimal operating conditions for CO₂ storage after desorption. The intertwining among raw solids properties-impregnation conditions-properties of the functionalized materials-solids capture capacity has been investigated by comparing CO₂ adsorption results with outcomes obtained from sorbents CO₂/N₂ porosimetric and thermogravimetric analyses. Adsorption isotherms have been interpreted in the light of theoretical models for a comprehension of the main mechanisms involved in the capture of CO₂ by the investigated solids. Breakthrough data have been modelled also in order to identify the rate-determining step of the adsorption process and the effect of operating parameters on mass transfer phenomena.

This PhD Dissertation is organized as follows. In Chapter 2 a literature survey is reported in order to analyse the main classes of sorbents employed for CO₂ capture with particular emphasis on activated carbons together with the main applications of ionic liquids in CCS field. Chapter 3 provides the main theoretical aspects concerning both thermodynamics and kinetics of the adsorption phenomenon. Chapter 4 describes the experimental protocols adopted for activated carbons impregnation with ionic liquids, solids characterizations and adsorption/regeneration experiments; a description of the lab-scale plant designed, built and optimized for the execution of adsorption experiments is also provided. In Chapter 5 the main results obtained from adsorbents characterizations and CO₂ capture/regeneration tests are

discussed together with the main aspects derived from thermodynamics and kinetics modelling. Finally, conclusions and future developments are reported in Chapter 6.

CHAPTER 2

LITERATURE OVERVIEW

In this Chapter the main adsorbent materials employed in CCS field are analysed with particular emphasis on the applications of activated carbons for CO₂ capture, as they are of major interest for this PhD project. The main applications of ionic liquids in this context are also discussed.

2.1 Utilization of activated carbons in CCS field

Activated carbons are carbonaceous materials with a common structure made up of an assembly of defective graphene layers that have high potentiality for CO₂ capture thanks to a complex structure characterized by micropores that determine high surface area for adsorption, but also meso- and macropores which can facilitate the diffusion (fast kinetics) of the adsorbate to the inner porosity (Marsh and Rodríguez-Reinoso, 2006; Whaby et al., 2010; Sayari et al., 2011). Activated carbons act as physisorbents towards CO₂, thus their adsorption capacity decreases rapidly as temperature increases (Choi et al., 2009; Sayari et al., 2011). Moreover, the mild adsorption strength in the low-pressure regime (<0.5 bar) makes activated carbons easily regenerable. In the following, main retrieved results for CO₂ adsorption on raw activated carbons will be discussed (Section 2.1.1); moreover, the main activation treatments aimed at the introduction of highly CO₂-affine functional groups on the carbon surface will be analysed (Section 2.1.2).

2.1.1 CO₂ adsorption onto as-synthesized activated carbons

The use of activated carbons for CO₂ capture is nowadays considered a viable route mainly for storage purposes because they can be efficiently used in pure CO₂ streams and at high pressures (Sayari et al., 2011). Nevertheless, the synthesis of tailored microporous structures can extend their use also for separation and purification fields by discriminating molecules on shape and/or size basis (Whaby et al., 2010).

Table 2.1 reports main literature data concerning CO₂ equilibrium adsorption capacity ω_{eq} on raw activated carbons and in pure CO₂ streams at different pressures and temperatures; it is underlined that the sorbent CO₂/N₂ selectivity (S) is evaluated as the ratio of the adsorbed amounts of the two gases obtained in single compound equilibrium tests.

Table 2.1 CO₂ equilibrium adsorption capacity in pure streams on as-synthesized activated carbons at different pressures and temperatures

Sorbent	T [°C]	P [bar]	ω_{eq} [mmol g⁻¹]	S (CO₂/N₂)	Reference
F30/470	24	0.16	0.65	n.a. [†]	(Berlier and Frère, 1996)
Ajax	25	0.2	0.75	n.a. [†]	(Do and Wang, 1998)
Salnchunri	25	0.1	0.60	1.2	(Na et al., 2001)
	55	0.1	0.25	1.3	
Filtrisorb 400	25	0.1	0.57	n.a. [†]	(Lu et al., 2008)
pitch-based activated carbon	30	1	1.9	5	(Shen et al., 2010)
	90	0.2	0.1	4	
pitch-based VR-5-M molecular sieve	0	1	8.6	2.8	(Whaby et al., 2010)
	25	1	4.2	n.a. [†]	
	50	1	2.3	n.a. [†]	
Maxsorb III	30	2.86	5.4	n.a. [†]	(Saha et al., 2011)
	50	2.57	3.4	n.a. [†]	

[†] not available

As expected, it can be evidenced a decrease of CO₂ adsorption capacity at higher temperatures. Whaby et al. (2010) compared zeolites 13X and 5A with carbon molecular sieves and observed that the latter show higher CO₂ adsorption capacity at 1 bar and 0°C. They also inferred that the presence of narrow micropores (diameter < 0.7 nm) plays a major role in determining the solid adsorption capacity. Noteworthy, Silvestre-Albero et al. (2011) showed that CO₂ adsorption on carbon molecular sieve monoliths is highly reversible, with no loss of adsorption capacity under three consecutive adsorption/desorption cycles, making them excellent candidates for pressure swing adsorption units.

An interesting experimental campaign concerning CO₂ capture in CO₂/H₂/N₂ (20/70/10% by vol.) mixtures on raw activated carbon was carried out by García et al. (2011). In particular, they studied the removal of CO₂ in a fixed bed apparatus and analysed the effect of the temperature and CO₂ partial pressures on the system dynamic performances. The main results showed that at each temperature and fixed carbon dioxide concentration, higher CO₂ partial pressures (obtained by increasing the system total gas pressure) determine longer breakpoint time, and this behaviour was imputed to a slower concentration front in the bed; moreover, at higher temperatures the process was faster but a parallel reduction in adsorption capacity was observed. Finally, Shen et al. (2011) studied the recovery of CO₂ from saturated pitch-based activated carbon by means of Vacuum Pressure Swing Adsorption after fixed-bed adsorption in a CO₂/N₂ mixture (15/85% by vol.): results showed that for a N₂ feed pressure of 2 bar, a CO₂ purity of 94% and 78% recovery could be obtained.

2.1.2 CO₂ adsorption on functionalized activated carbons

The main functionalization treatments of activated carbons investigated in the literature are the impregnation with amine-based compounds or alkali/alkaline earth metals and amination with gaseous ammonia. The main results are reported in the following.

Impregnation with amine-based compounds

The dispersion of compounds containing amine functionalities over the surface of activated carbons is a very attractive option to increase their capture performances towards CO₂ because amines are able to form either carbamate (in dry condition) or carbonate/bicarbonate (in humid condition), as evidenced in Figure 2.1 (Gray et al., 2005; Choi et al., 2009).

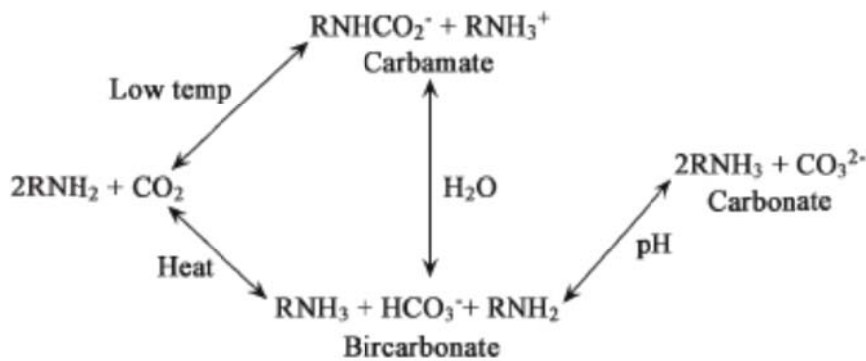


Figure 2.1 Reaction schemes of amine groups with CO₂ (Gray et al., 2005)

Aroua et al. (2008) used palm shell-based activated carbon as precursor in the production of molecular basket via impregnation with polyethyleneimine (PEI). Very interestingly, they showed that an increase of pure CO₂ adsorption capacity with respect to the virgin solid could be obtained at an optimal 0.26% wt. PEI loading. As a matter of fact, at low PEI loadings the increase in the solid capture performances was ascribed to the creation of additional meso- and micropores deriving from polymer constriction of larger pores as well as to an enhanced chemisorption effect induced by nitrogen groups present in the active phase; further increases in the charged-amount of PEI, likely constricted the pore accessibility to CO₂ molecules. Recently, an interesting study has been carried out by Khalil et al. (2012) which used microporous activated carbon beds impregnated with monoethanolamine (MEA) and 2-amino-2-methyl-1-propanol (AMP) for treating a 15% by vol. CO₂ gaseous stream (at room temperature and atmospheric pressure). The authors observed an increase of CO₂ removal

capacity for both functionalized sorbents (1.11 and 0.70 mmol g⁻¹ for MEA- and AMP-carbon, respectively) with respect to the raw material (0.41 mmol g⁻¹); the higher performances of MEA-carbon was ascribed to a more efficient dispersion of less sterically hindered MEA molecules over the support surface with respect to AMP, thus creating more accessible sites for CO₂ capture.

Impregnation with alkali/alkaline earth metals

Impregnation of activated carbons with calcium and magnesium oxide was investigated by Yong et al. (2001), since these metals have a high basic nature which favors the interaction with CO₂ acidic molecule. In particular, they observed that at low temperature (28°C) the raw materials exhibited higher pure-CO₂ adsorption capacity with respect to metal-doped materials: this was ascribed to the reduction in surface area occurring during the activation process. Conversely, at higher temperature (300°C) the activated materials showed improved performances because of the prevailing of chemisorption effects over physisorption, the latter being surface dependent and dominant at low temperatures.

Amination

Amination is a treatment usually referred to the reaction of gaseous ammonia with the surface of activated carbons, performed at high temperatures (ranging from 400 to 900°C), aimed at increasing the solid nitrogen content (Plaza et al., 2009; Shafeeyan et al., 2010; Plaza et al., 2011). Ammonia can react with surface oxides and active sites present at the edges of the graphene layers to form amines, amides, imides, lactams, nitriles, pyridine- or pyrrole-like functionalities. As an example of amination effect, Plaza et al. (2009) observed an enhancement of pure CO₂ adsorption capacities for almond shell-derived activated carbons aminated at temperatures greater than 600°C with respect to the parent carbon; moreover the authors observed that in the range 400-900°C the sample aminated at 800°C had the greatest CO₂ adsorption capacity due to a maximum nitrogen content, as confirmed by ultimate analyses. Plaza et al. (2011) investigated the use of aminated biomass-based carbon to capture CO₂ in a 17% by vol. gaseous stream (balance N₂) at 20°C and atmospheric pressure; in particular, they focused on the solid regenerability showing that Thermal Swing Adsorption carried out at 100°C allows an easy recovery of the pollutant and that after 40 cycles the adsorbent did not display relevant deactivation.

2.2 Other classes of CO₂ sorbents investigated

2.2.1 Zeolites

Zeolites are microporous crystalline aluminosilicates built of a periodic array of SiO₄ and AlO₄ tetrahedra (Ruthven, 1984). Their uniform pore size grants a unique ability as molecular sieves. CO₂ is captured by zeolites mainly via electrostatic interactions generated by the exchangeable cations in the pores and by hydrogen bonds with surface silanol groups (Choi et al., 2009). In particular, zeolites characterized by a low Si/Al ratio have a high content of extra-framework cations which favourably interact with CO₂ molecule (Sayari et al., 2011). Generally, CO₂ adsorption on zeolites is negatively affected by a temperature increase (Sayari et al., 2011). Tlili et al. (2009) observed a six-times reduction in CO₂ adsorption capacity on 5A zeolite by varying the operating temperature from 25 to 200°C. In addition, these solids show lower CO₂ adsorption capacity under humid conditions. Rege and Yang (2001) showed by means of FTIR analyses that there is a competition between water vapour and CO₂ for adsorption sites on NaX zeolite surface. It has been highlighted that zeolitic adsorbents have a stronger physical interaction with CO₂ and higher heats of adsorption compared to activated carbons, thus rendering the desorption process more energy intensive (Whaby et al., 2010). Moreover, the hydrophobic nature of most activated carbons makes them less sensitive to competitive adsorption effects between CO₂ and water vapour with respect to zeolites (Choi et al., 2009). In general, it is underlined that equilibrium adsorption experiments on zeolites are carried out in pure CO₂ in most of the cases investigated in the literature: typical reported adsorption capacity varies between 0.2-1.6 mmol g⁻¹ in the pressure range 0.1-0.4 bar and at a temperature of 60°C (Sayari et al., 2011). Finally, CO₂ adsorption kinetics on zeolites can be ranked among the fastest known, reaching an equilibrium condition within a few minutes in most cases (Choi et al., 2009).

2.2.2 Ordered mesoporous silicas (OMS)

Ordered mesoporous silicas (e.g., MCM-41, SBA-15, TUD-1, HMM-33 and FSM-16) are a class of silica materials characterized by different cage structures (such as hexagonal, cubic and lamellar) that have attracted attention in catalysis and separation due to their extremely high surface area and precise tuning of pore sizes (Chew et al., 2010).

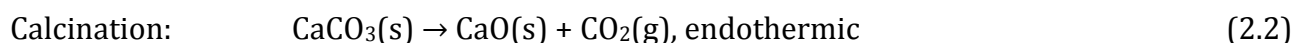
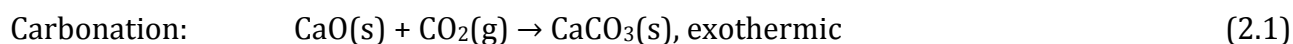
Generally, few studies are retrievable in the pertinent literature for CO₂ adsorption on as-synthesized ordered mesoporous silicas, but many concern the removal of carbon dioxide onto amine-modified OMS (Belmabkhout and Sayari, 2009; Jang et al., 2009; Devadas et al.,

2010). As a matter of fact, pure silica surfaces contain residual hydroxyl groups that are not able to interact strongly with CO₂ (Chew et al., 2010). Typical CO₂ adsorption capacity in flue-gas conditions (temperature 75°C, CO₂ 5-10% by vol.) reported for PEI-impregnated OMS varies in the range 2.1-3.8 mmol g⁻¹ (Sayari et al., 2011). Post synthesis grafting is a functionalization technique widely applied for the modification of ordered mesoporous silicas and involves a reaction between surface hydroxyl groups of OMS and the alkoxy ligands of an amino silane, determining a layer of tethered amine groups on the support surface (Chang et al., 2009; Serna-Guerrero and Sayari, 2010; Sayari et al., 2011). These adsorbents have a clear advantage over amine-impregnated silicas as they do not show any amines leaching (unless conditions are strong enough to break covalent bonds), thus determining potentially less problems of equipment corrosion, usually associated to liquid amines (Choi et al., 2009). Finally grafted OMS have shown great stability under thousands CO₂ adsorption-desorption cycles (Sayari et al., 2011).

2.2.3 Calcium oxide

Calcium minerals are the most abundant in nature among alkaline earth metal oxides, commonly found in the form of carbonates such as limestone or dolomite. When treated at high temperatures, calcium carbonates liberate CO₂ and generate calcium oxides.

The removal of CO₂ from flue gas by calcium oxide can be accomplished in two steps (see eqs. (2.1) and (2.2)):



a first reaction of the oxide with CO₂ to form calcium carbonate, performed in a carbonator at temperatures in the range 650-700°C, and a subsequent heating of the carbonate at temperatures higher than those of the carbonation step (calcination) to regenerate the calcium oxide and release concentrated CO₂ (Abanades and Alvarez, 2003; Choi et al., 2009; Blamey et al., 2010).

Hughes et al. (2005) explored the *in situ* CO₂ capture, at 700°C and atmospheric pressure, in a dual fluidized bed combustion system. The adsorption kinetics of CO₂ on calcium oxide adsorbents is much slower than on physisorbents such as zeolites and activated carbons, sometimes requiring several hours to achieve ca. 70% of the total adsorption capacity (Choi et al., 2009). Moreover, calcium oxide-based adsorbents suffer from a rapid degradation of CO₂ capture capability during the repetition of carbonation/calcination cycles: this reduction has

mainly been ascribed to pore blocking and adsorbent sintering (Abanades and Alvarez, 2003). Finally, material loss due to attrition and fragmentation in fluidized bed systems together with the sorbent deactivation produced by the sulphation reaction with SO₂ (always present in a typical flue-gas) are important issues related to Ca-based sorbents (Montagnaro et al., 2010; Coppola et al., 2012a and 2012b).

2.2.4 Metal-organic Frameworks (MOFs)

An emerging new class of crystalline solids called metal-organic frameworks (MOFs) has recently been investigated as sorbents for CO₂ capture. These materials generally consist of three-dimensional organic-inorganic hybrid networks formed by multiple metal-ligand bonds (Eddaoudi et al., 2002; Choi et al., 2009; An and Rosi, 2010; Saha et al., 2010; Sayari et al., 2011). These solids are highly versatile because the pore spaces of MOFs are tuneable over a substantial range by using ligands with different molecular dimensions (An and Rosi, 2010): with some of the larger ligands the materials even became mesoporous. MOFs have been developed for use as CO₂ physisorbents or storage materials, by optimizing the pores size for the carbon dioxide molecule. Even if they show good adsorption capacities towards CO₂ at high pressures (greater than 10 bar), it has been highlighted that for low pressure range (of practical interest for post-combustion capture) MOFs exhibit unfavourable adsorption isotherms (Sayari et al., 2011). Additionally, MOFs are usually unstable in humid conditions and high temperatures showing low CO₂ selectivity with respect to N₂ (Sayari et al., 2011). Finally, their performances over multiple adsorption and desorption cycles have to be tested (Choi et al., 2009).

In addition to MOFs, new type of solids are currently being investigated as CO₂ adsorbents but are still at early stage of development: poly(ionic liquid)s (see Section 2.3.1), zeolitic imidazolate frameworks (ZIFs) and carbon nanotubes (Choi et al., 2009; Herzog et al., 2009).

From the analysis of the aforementioned solids (either as synthesized or functionalized), recently reviewed by Choi et al. (2009), Sayari et al. (2011) and Samanta et al. (2012), the following aspects can be highlighted: i) zeolites and activated carbons are characterized by very fast CO₂ adsorption kinetics but their performances decrease at temperatures greater than 100°C and in the presence of moisture (always present in a flue gas); ii) calcium oxide provides high CO₂ adsorption capacities but requires high temperatures for regeneration, which determine structural changes with loss of activity during several carbonation/calcinations cycles; iii) amine-functionalized solids usually display an

enhancement of the CO₂ capture capacity in presence of moisture (related to the possibility of forming carbonate/bicarbonate), but their application at high temperatures is limited by amines degradability.

As a further remark, it should be noted that even if great efforts are currently devoted to the development of high-performance sorbents for CO₂ capture, their use in typical flue-gas conditions and for many adsorption/desorption cycles is still limited. Moreover, there is a lack of exhaustive information concerning their dynamic performances in different reactor configurations (e.g., fixed bed, fluidized-bed, circulating-bed etc.), this being a key aspect for the design of industrial-scale post-combustion purification systems.

In this scenario, the use of ionic liquids for porous solids functionalization is an interesting although limitedly explored research topic, in order to develop highly CO₂-affine sorbents. In the following, a brief overview on ionic liquids, their application and perspectives in CO₂ capture technologies is presented.

2.3 Ionic liquids (ILs)

Ionic liquids (ILs) are organic salts composed entirely by ions with melting point usually lower than 100°C; many ILs are liquids at room temperature and, for this reason, are commonly referred as Room Temperature Ionic Liquids (RTILs) (Zhang et al., 2006a; Bourbigou et al., 2010; Hasib-ur-Rahman et al., 2010). ILs are characterized by negligible vapour pressure at room temperature, a broad temperature range of liquid state (depending on the anionic/cationic couple), excellent thermal and chemical stabilities: these unique properties make them as optimal candidates as solvents and catalysts (Zhang et al., 2006a; Boschetti et al., 2007; Bourbigou et al., 2010). Their typical viscosity ranges from 50 to 1000 cP at room temperature (Figuerola et al., 2008). Some typical ILs cations and anions are reported in Figure 2.2: cations are usually organics such as imidazolium, pyridinium or ammonium while anions include halides and fluoro-borate/phosphate/sulphonate (Hasib-ur-Rahman, et al., 2010).

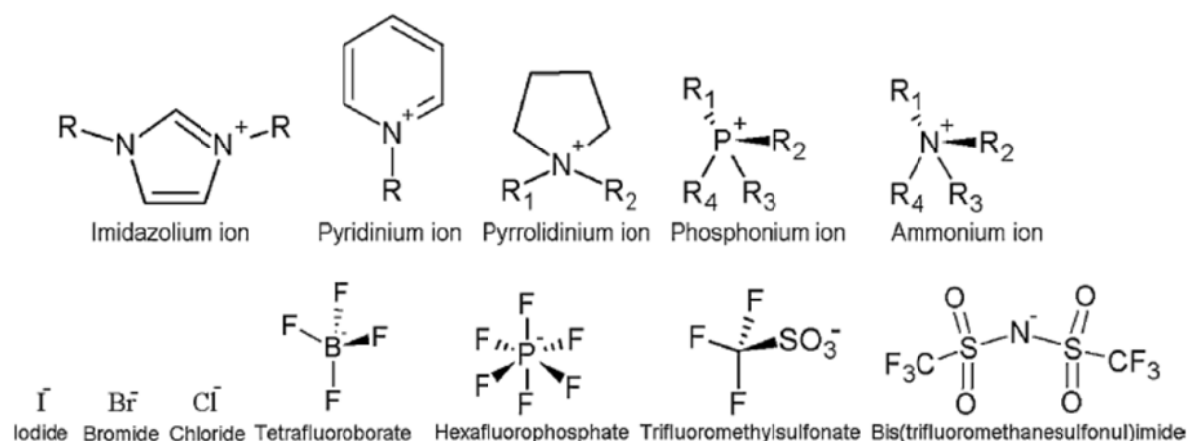


Figure 2.2 Typical cations and anions constituting ILs (Hasib-ur-Rahman et al., 2010)

ILs properties can be adequately tuned by introducing proper functional groups to obtain specific properties: this class of ionic liquids is commonly referred as Task-Specific Ionic Liquids (TSILs) (Zhang et al., 2006a; Bourbigou et al., 2010).

2.3.1 ILs applications for CO₂ capture

Use of ILs for CO₂ capture is gaining interest due to their unique properties that can overcome the problems associated with traditionally-employed liquid amines such as degradation and equipment corrosion (Zhang, et al. 2006a; Bourbigou et al., 2010): potentially it could be possible to recover CO₂ from flue gas without having to cool it first, thus reducing significantly the capture costs (Figueroa et al., 2008).

Many RTILs have been studied for CO₂ absorption (in particular imidazolium-type ILs) and the following aspects are here highlighted (Zhang et al., 2006a; Bourbigou et al., 2010): i) CO₂ solubility in RTILs is greater than that observed in common organic solvents (e.g., heptane, benzene) at the same pressure and temperature conditions; ii) the nature of the anion has a stronger influence on CO₂ solubility than that of the cation, because of weak Lewis acid-base interaction between the anion and the acidic CO₂ molecule. It should be underlined that most of the published research papers reports CO₂ solubility in RTILs at high pressures; CO₂ absorption capacity in imidazolium-based RTILs at lower pressures (2 bar) and 25°C is typically 0.05 mol_{CO₂}/mol_{IL}. Moreover, RTILs physically interact with CO₂, thus their absorption capacity strongly decreases with temperature (Soriano et al., 2009; Zhang et al., 2011).

Ionic liquid absorption properties towards CO₂ can be enhanced by functionalizing the IL with basic groups (like amines) to obtain task-specific ionic liquid (Zhang et al., 2006a and

2006b; Zhang et al., 2011). Bates et al. (2002) were the first to synthesize a TSIL ([Pabim][BF₄]) containing an amine group covalently tethered to an imidazolium cation; this IL is able to form carbamate with CO₂ following a reaction mechanism similar to that reported for amine solvents (Figure 2.3).

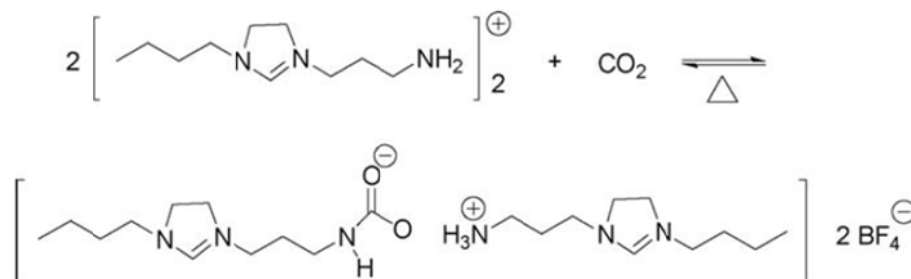


Figure 2.3 Proposed reaction mechanism between [Pabim][BF₄] and CO₂ (Bates et al., 2002)

Recently, Zhang et al. (2006b) synthesized a new class of amino-acid based ionic liquids, showing that in presence of small amount of water the CO₂ absorption capacity was double than in case of absence of water due to bicarbonate formation. Finally, Xue et al. (2011) explored the use of ionic liquids with amino-functionalized imidazolium cation and taurine anion as CO₂ solvent, showing absorption capacities up to 0.9 mol_{CO₂}/mol_{IL} at 25°C and 1 bar and an easy thermal regeneration of the solvent.

Another interesting approach related to ILs application in CCS field is the possibility of synthesizing solid membranes using polymerizable ionic liquids (Tang et al., 2005; Bara et al., 2008); this class of solids is termed poly(ionic liquid)s. Tang et al. (2005) observed that imidazolium-based poly(ionic liquid)s have enhanced CO₂ adsorption capacities compared to RTILs. Bara et al. (2008) showed that ionic liquid monomers modified with polar groups (such as nitrile-containing alkyl groups) can enhance the separation selectivity towards CO₂ of the polymeric membranes.

2.3.2 Functionalization of solids with ionic liquids (ILs)

Impregnation of ionic liquids onto solid supports is a suitable technique for those ILs which exhibit high viscosity (mainly TSILs), thus determining problems of applicability to industrial scale absorbers. Moreover, the IL dispersion on a solid support can potentially determine high liquid-gas contact surface and, consequently, greater external mass transfer coefficients (Hasib-ur-Rahman et al., 2010). The great interest for Supported Ionic Liquid Phase (SILP) materials is also justified by the possibility of minimizing the amount of IL used (smaller than the sorbent pore volume), providing important economic benefits for their

application (Lemus et al., 2011). Nevertheless, the behaviour of ILs confined in nanospaces in the context of CO₂ capture processes is only at a preliminary stage of investigation (Tanaka et al., 2011; Kolding et al., 2012). For example, Tanaka et al. (2011) observed that the dispersion of 1-hexadecyl-3-methylimidazolium chloride ionic liquid into nanoporous silica microspheres determines an enhancement of its CO₂ capture performances with respect to the bulk solvent properties. The authors ascribed this behaviour to the formation of ordered molecular domains, promoted by silica surface-IL interactions, in which CO₂ occupies specific positions. Zhang et al. (2006b) observed that for CO₂ adsorption by amino-acid based ionic liquids supported on porous silica gel, the equilibrium is reached faster than bubbling CO₂ through bulk ILs. In addition, ILs can be supported on porous alumina membranes or adsorbed on polymeric membranes to increase their selectivity with respect to CO₂ (Hasib-ur-Rahman et al., 2010). Finally, immobilization of imidazolium-type ionic liquids onto silica supports is gaining great interest also because ILs act as high-activity catalysts in the cycloaddition reaction between epoxides and CO₂ to produce five-membered cyclic carbonates (Shim et al., 2009; Udayakumar et al., 2009 and 2010). Cyclic carbonates are excellent aprotic polar solvents and intermediates commonly applied in the production of pharmaceuticals and fine chemicals.

CHAPTER 3

THEORETICAL FRAMEWORK OF THE ADSORPTION PROCESS

In this Chapter the main theoretical aspects concerning both thermodynamics and kinetics of the adsorption phenomenon will be discussed in order to provide a useful basis for a deep comprehension of the main mechanisms involved in the capture of CO₂ by the investigated solids.

3.1 Adsorption equilibria

The thermodynamic study of adsorption processes allows obtaining adsorption isotherms, i.e. experimental curves which establish a relationship between the solid specific adsorption capacity toward a target pollutant and the contaminant partial pressure in the gas phase at a fixed temperature and under equilibrium conditions. The evaluation of equilibrium adsorption capacity for a given gas-solid system is of great importance not only because it provides information about the amount of pollutant that can be loaded on the sorbent and the nature of interactions governing the process: the system thermodynamic behaviour, in fact, affects the dynamic performances of an adsorption process and consequently the size of an adsorber unit. The interpretation of experimental equilibrium adsorption data by means of an adequate theoretical model allows to define the solid affinity toward a specific pollutant (by evaluating the interaction energy between the sorbent and each gaseous species) and the capture mechanism involved in the process.

A simple model used in the literature for the interpretation of equilibrium adsorption data is Langmuir model, which is based on the following assumptions: i) each site can guest one adsorbate molecule (monolayer); ii) there is no mobility of adsorbed species on the surface; iii) the heat of adsorption is constant with loading; iv) all sites are energetically equivalent (Ruthven, 1984). The general form of the Langmuir isotherm can be expressed as:

$$\omega_{\text{eq}} = \frac{\omega_{\text{max}}K_L P_{\text{eq}}}{1+K_L P_{\text{eq}}} \quad (3.1)$$

where ω_{eq} [mmol g⁻¹] and P_{eq} [bar] are the adsorbent specific molar adsorption capacity and the equilibrium gas partial pressure of the adsorbate respectively; K_L [bar⁻¹] and ω_{max} [mmol g⁻¹] represent the Langmuir equilibrium constant and the maximum adsorption capacity of the adsorbed species respectively.

Alternatively, for low adsorbate partial pressures, the solid-fluid adsorption equilibrium can be expressed by the Henry's law:

$$\omega_{\text{eq}} = K_{\text{H}}P_{\text{eq}} \quad (3.2)$$

in which K_{H} [$\text{mmol g}^{-1} \text{bar}^{-1}$] is the Henry equilibrium constant.

The Freundlich isotherm can be applied to account for surface heterogeneity:

$$\omega_{\text{eq}} = K_{\text{F}}P_{\text{eq}}^{\frac{1}{n}} \quad (3.3)$$

In eq. (3.3), K_{F} [$\text{mmol g}^{-1} \text{bar}^{-1/n}$] and $1/n$ [-] are the Freundlich constant and the heterogeneity parameter respectively (both generally temperature-dependent) (Do, 1998).

The potential theory has been developed mainly by Dubinin and Polanyi to characterize the adsorption process in microporous solids (such as activated carbons) (Polanyi, 1932; Dubinin and Radushkevich, 1947; Ruthven, 1984; Do, 1998). In such solids, the pore dimension is comparable to that of the adsorbate molecule and the adsorption mechanism is due to filling because the adsorption field encompasses the entire micropore volume. In the micropore filling theory an adsorption potential A is defined as:

$$A = RT \ln \frac{P_0}{P_{\text{eq}}} \quad (3.4)$$

where P_0 and P_{eq} are the liquid sorbate vapour pressure and the pressure of the gas in equilibrium with the adsorbate phase respectively, at the same temperature T . An important feature of the micropore filling theory is that for a given adsorbent-adsorbate system there is a unique temperature-independent relationship between the adsorption potential and the adsorbate fractional loading referred as the characteristic curve (Ruthven, 1984; Do, 1998).

Dubinin and Radushkevich suggested the following Gaussian expression to relate the degree of micropore filling and the adsorption potential (Dubinin and Radushkevich., 1947):

$$\frac{V}{V_0} = \exp \left[- \left(\frac{A}{E} \right)^2 \right] \quad (3.5)$$

in which V is the volume of adsorbate in the micropores per unit mass of the solid, V_0 is the maximum specific volume that the adsorbate can occupy (obtainable from porosimetric analyses), and E is a characteristic energy (related to the adsorption strength between adsorbate and adsorbent). Once V and V_0 are known, the solid molar adsorption capacity ω

and the saturation uptake ω_{\max} can be calculated assuming a liquid-like adsorbed phase according to Gurvitsch as (Do, 1998):

$$\omega = \frac{V}{V_m} \quad (3.6)$$

$$\omega_{\max} = \frac{V_0}{V_m} \quad (3.7)$$

where V_m is the liquid molar volume.

It should be underlined that above the adsorbate critical temperature the concept of liquid ceases to exist. In this context, different methods have been proposed to evaluate V_m and replace the vapour pressure with a pseudo-vapour pressure; some of these expressions have been collected in (Do, 1998) and are not reported here for the sake of brevity.

Finally, the determination of the adsorption isotherms at different temperatures allows the estimation of the isosteric heat of adsorption (q_{st}), which is a useful parameter providing information on the degree of energetic heterogeneity of gas-solid interactions. It can be computed by applying the well-known Clausius-Clapeyron equation (Do, 1998):

$$q_{st} = RT^2 \left(\frac{\partial \ln P_{eq}}{\partial T} \right)_{\omega} \quad (3.8)$$

3.2 Dynamics of adsorption columns

Most of the adsorption processes are carried out in fixed bed adsorbers, typically tubular reactors packed with the adsorbent material which is contacted with a gaseous stream containing the pollutant to be removed. In such systems, the compositions of both the fluid and solid phases change with time as well as with the position in the bed (McCabe et al., 1993). In the common practice of adsorption experiments it is difficult to measure internal composition profiles for evaluating the dynamic performances of an adsorption column; thus, it is more convenient to monitor the concentration of the adsorbate at the column outlet as a function of time, obtaining the so-called breakthrough curve as reported in Figure 3.1. It is highlighted that the time evolution of the composition profile can be conveniently expressed in terms of the ratio between the volumetric flow rate of the adsorbed i species at the column outlet and the correspondent value of the feed ($Q_i^{\text{out}}(t)/Q_i^{\text{in}}$), if percentage volumetric concentrations can be experimentally obtained (as in the case of the NDIR analyzer adopted in this project, cf. Chapter 4).

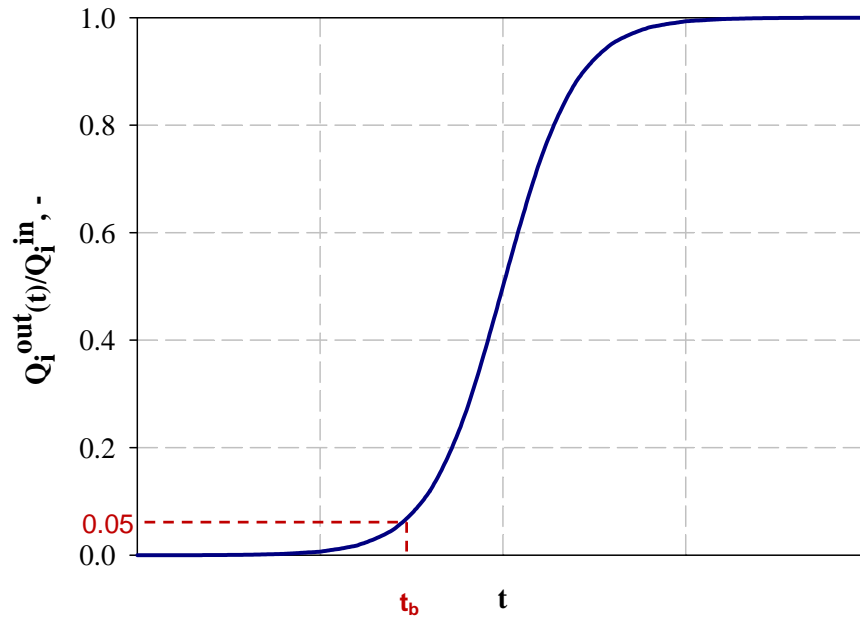


Figure 3.1 Characteristic breakthrough curve obtained from fixed-bed adsorption experiments

It can be observed that the curve is S-shaped: initially the pollutant is completely adsorbed, then its concentration at the outlet increases up to the inlet level when the solid is completely saturated. In general, for the breakthrough curve it is possible to define a characteristic breakpoint time t_b for which $Q_i^{out}(t)/Q_i^{in}=0.05$; in the industrial practice, it usually represents a limiting working condition for the adsorber corresponding to regulation emission limit (McCabe et al., 1993).

It can be demonstrated that the area above the breakthrough curve is proportional to the total amount of pollutant captured by the adsorbent; as a matter of fact, in order to evaluate the solid adsorption capacity, a material balance [mg] on i species over the adsorption column is required as reported in eq. (3.9):

$$Q_i^{in} \rho_i dt - Q_i^{out}(t) \rho_i dt = m d\omega \quad (3.9)$$

in which Q_i^{in} and $Q_i^{out}(t)$ [$L s^{-1}$] represent again the column inlet and outlet i species volumetric flow rates respectively, ρ_i [$mg L^{-1}$] is the pollutant density at the operative temperature and pressure, m [g] is the adsorbent mass and $d\omega$ [$mg g^{-1}$] the differential solid adsorption capacity. The mass balance equation (3.9) takes into account that, in the differential time dt , the pollutant mass adsorbed on the solid ($md\omega$) equals the same quantity lost by the gaseous phase (LHS in eq. (3.9)).

By rearranging eq. (3.9) and integrating between zero and time t^* for which $Q_i^{out}(t)/Q_i^{in}$ is practically unitary (complete solid saturation), it is possible to evaluate the solid total

adsorption capacity ω_{eq} , as reported in eq. (3.10):

$$\omega_{eq} = \frac{Q_i^{in} \rho_i}{m} \int_0^{t^*} \left(1 - \frac{Q_i^{out}(t)}{Q_i^{in}} \right) dt \quad (3.10)$$

The correct interpretation of the effects of the adsorption kinetics and the extent of the axial mixing in the column on the adsorbent dynamic performances requires an appropriate model that gives a theoretical breakthrough curve matching the experimental data. Moreover, the design of an adsorption column can be realized without the recourse to extensive experimentation by predicting *a priori* the kinetic response curve from equilibrium data and by estimating the mass transfer coefficients once the solid-sorbate properties are known and the system fluid dynamics is fixed. The rigorous mathematical model requires the solution of equations deriving from mass, momentum and energy balances. The hypotheses adopted in this work to describe the fixed bed dynamics are (Ruthven, 1984; Ding and Alpay, 2000; Delgado et al., 2006; Serna-Guerrero and Sayari, 2010; Shen et al., 2010):

- the flow pattern is described with the axially dispersed flow model;
- the mass transfer rate is governed by a linear driving force (LDF);
- the gas phase behaves as an ideal gas mixture;
- radial concentration and temperature gradients are negligible;
- the system is isothermal.

It should be noted that even if a typical industrial-scale adsorption column is operated adiabatically, lab-scale experiments are usually carried out in a temperature-controlled environment which leads to the useful approximation of an isothermal fixed-bed adsorber that simplifies the system mathematical modelling (Serna-Guerrero and Sayari, 2010). In addition, typically employed physisorbents (such as activated carbons) show low adsorption heat which determines a negligible effect on the gas temperature, thus supporting the hypothesis of an isothermal process.

Mass and momentum balances

On the basis of the above-mentioned assumptions, the mass balance for the adsorbate i species in a differential element of the column dz (total length L) is given by:

$$-\varepsilon D_{ax} \frac{\partial^2 C_i}{\partial z^2} + \frac{\partial u C_i}{\partial z} + \varepsilon \frac{\partial C_i}{\partial t} + (1 - \varepsilon) \rho_p \frac{\partial \omega_i}{\partial t} = 0 \quad (3.11)$$

where C_i is the adsorbate concentration in the gaseous stream, t the time, ε the bed voidage fraction, u the gas superficial velocity, ρ_p is the adsorbent particle density and D_{ax} represents the axial dispersion coefficient. The resolution of the mass balance equation (3.11) can be obtained by fixing the following initial and boundary conditions:

$$\triangleright t = 0 \quad \omega_i = 0 \quad \forall z \quad (3.12a)$$

$$\triangleright t = 0 \quad C_i = 0 \quad 0 < z \leq L \quad (3.12b)$$

$$\triangleright z = 0 \quad C_i = C_i^{in} \quad \forall t \quad (3.12c)$$

$$\triangleright \left. \frac{\partial C_i}{\partial z} \right|_L = 0 \quad \forall t \quad (3.12d)$$

in which C_i^{in} is the pollutant concentration in the gaseous phase at the column inlet. It should be noted that in eq. (3.12a) it has been assumed that the adsorbent is initially free of adsorbate ($\omega_i=0$).

The rate of adsorption for the adsorbate is expressed as:

$$(1 - \varepsilon)\rho_p \frac{\partial \omega_i}{\partial t} = (1 - \varepsilon)\rho_p k_{s,i}(\omega_i^* - \omega_i) \quad (3.13)$$

where $k_{s,i}$ is a lumped mass transfer coefficient and ω_i^* the solid adsorption capacity for i component which would be in equilibrium with its concentration in the gaseous phase (C_i). In this context, it is underlined that the resolution of eq. (3.13) requires an appropriate equilibrium expression $\omega_i^*=f(C_i,T)$ which can be obtained from one of the adsorption isotherms discussed in Section 3.1.

The relationship between the total pressure gradient and the gas superficial velocity can be derived from the Ergun's equation:

$$\frac{\partial P}{\partial z} = \frac{150\mu(1-\varepsilon)^2}{\varepsilon^3 d_p^2} u + \frac{1.75(1-\varepsilon)\rho_g}{\varepsilon^3 d_p} u^2 \quad (3.14)$$

where μ and ρ_g are the viscosity and density of the gas respectively, while d_p represents the mean Sauter particle diameter.

Evaluation of axial dispersion and mass transfer coefficients

The resolution of the equations relative to the rate of adsorption and mass balance for i component of the system expressed in eqs. (3.11 and 3.13), requires an estimation of the effect of the axial dispersion (D_{ax}) and the global mass transfer coefficient $k_{s,i}$.

In general for a porous adsorbent material the adsorption process is characterized by a complex mechanism which involves (Ruthven, 1984; Perry and Green, 1997):

- external mass transfer of the pollutant in the fluid film layer surrounding the solid particle;
- macropore and micropore diffusion of the adsorbate within the adsorbent;
- adsorption on the solid active sites.

The pseudo-reaction between the pollutant and the solid sorbent is usually fast for physical adsorption, thus the evaluation of diffusion resistances allows the identification of the rate-determining step of the process.

The global mass transfer resistance is commonly expressed as a linear combination of the film, macropore and micropore diffusion resistances as (Ruthven, 1984; Perry and Green, 1997):

$$\frac{1}{k_{s,i}H_i} = \frac{d_p}{6k_{ext,i}} + \frac{d_p^2}{60\varepsilon_p D_{macro,i}} + \frac{d_p^2}{60H_i D_{micro,i}} \quad (3.15)$$

where $k_{ext,i}$ is the external fluid film mass transfer coefficient for i , $D_{macro,i}$ and $D_{micro,i}$ its macropore and micropore diffusivities, ε_p represents the particle porosity, H_i is the dimensionless Henry constant for i obtained from the slope of the linear part of the adsorption isotherm (by expressing the solid adsorption capacity in terms of volumetric concentration as a function of the concentration of i in the gaseous phase).

In order to evaluate the film mass transfer coefficient, it is useful to define the dimensionless Reynolds (Re), Sherwood (Sh) and Schmidt (Sc) numbers as:

$$Re = \frac{d_p \rho_g u}{\mu}; \quad Sh = \frac{d_p k_{ext,i}}{D_{ij}}; \quad Sc = \frac{\mu}{\rho_g D_{ij}}$$

in which D_{ij} is the i molecular diffusivity into the gas matrix (i.e. CO₂/N₂ mixtures in this project), which can be evaluated according to the Chapman-Enskog equation (Perry and Green, 1997):

$$D_{ij} = 1.858 * 10^{-3} \frac{T^{1.5} \left(\frac{1}{M_i} + \frac{1}{M_j} \right)^{0.5}}{P \sigma_{ij}^2 \Omega_D} \quad (3.16)$$

where M_i and M_j are the molecular weights for i and j species, σ_{ij} the average collision

diameter and Ω_D a temperature-dependent collision integral (tabulated).

The value of $k_{\text{ext},i}$ can be obtained according to the Wakao and Funazkri correlation (Perry and Green, 1997; Shen et al., 2010):

$$\text{Sh} = 2 + 1.1\text{Re}^{0.6}\text{Sc}^{\frac{1}{3}} \quad (3.17)$$

The macropore diffusivity $D_{\text{macro},i}$ can be evaluated as (Shen et al., 2010):

$$\frac{1}{D_{\text{macro},i}} = \tau_p \left(\frac{1}{D_{ij}} + \frac{1}{D_{k,i}} \right) \quad (3.18)$$

where τ_p is the pore tortuosity. The Knudsen diffusivity $D_{k,i}$ is given by (Ruthven, 1984):

$$D_{k,i} = 48.50d_{\text{pore}} \left(\frac{T}{M_i} \right)^{0.5} \quad (3.19)$$

with d_{pore} [m] representing the mean pore diameter.

The micropore diffusion is an activated process and exhibits an Arrhenius dependence from temperature (Ruthven, 1984):

$$D_{\text{micro},i} = D_{\text{micro},i}^0 \exp\left(-\frac{E_a}{RT}\right) \quad (3.20)$$

in which $D_{\text{micro},i}^0$ is the limiting diffusivity at infinite temperature and E_a the activation energy; $D_{\text{micro},i}$ is usually evaluated from chromatographic and NMR studies or from separate batch adsorption experiments (Ruthven, 1984).

The axial dispersion in packed beds usually derives from two main mechanisms: molecular diffusion and turbulent mixing arising from splitting and recombination of flows around the adsorbent particle (Ruthven, 1984). These effects can be considered additive, thus the axial dispersion coefficient can be expressed as:

$$D_{\text{ax}} = \gamma_1 D_{ij} + \frac{\gamma_2 d_p u}{\varepsilon} \quad (3.21)$$

with γ_1 and γ_2 constants; the values proposed for $\gamma_1=0.73$ and $\gamma_2 = 0.5 \left(1 + \frac{13\gamma_1 \varepsilon}{\text{ReSc}}\right)^{-1}$ by Edwards and Richardson have been used in this work (Perry and Green, 1997).

Finally, the effect of axial dispersion can be evaluated by computing the fixed-bed Péclet number defined as:

$$Pe = \frac{uL}{\varepsilon D_{ax}}$$

Typically, for $Pe > 100$ it is possible to consider an ideal plug-flow for the system (i.e. negligible axial dispersion) (Inglezakis and Pouloupoulos, 2006).

The numerical resolution of mass and momentum balance equations (3.11), (3.13) and (3.14) was obtained in this work with Aspen AdsimTM modelling environment adopting the method of lines: a Taylor-based Upwind Differencing Scheme was used for the discretization of first-order spatial derivatives and a second-order Central Differencing Scheme for the discretization of the second-order term (axial dispersion in eq. (3.11)). The aim of the mathematical modelling was to provide an estimation of the micropore diffusivity $D_{micro,i}$ (for each investigated gas-solid adsorption system) which is the only parameter not directly computable ($k_{ext,i}$ and $D_{macro,i}$ values can be determined once the adsorbent properties are known and the system fluid dynamics is fixed). To this end, Aspen AdsimTM software enables the evaluation of $D_{micro,i}$ as a fitting parameter by minimizing the sum of the squared differences between numerically calculated and experimentally observed values of the gaseous phase composition at the fixed-bed outlet (least squares method). The comparison of mass transfer resistances in eq. (3.15) allowed the determination of the rate-limiting step of the adsorption process.

CHAPTER 4

MATERIALS AND METHODS

In this Chapter the experimental protocols applied for activated carbons impregnation with ionic liquids, solids characterizations and adsorption/regeneration experiments are discussed. A description of the lab-scale plant designed for the execution of adsorption experiments is also provided.

4.1 Activated carbons, ionic liquids and impregnation protocols

Two activated carbons were selected for the experimental campaign carried out in this work in order to assess the effect of different porosimetric structures on CO₂ capture efficiency for both raw and ILs impregnated materials: Calgon Carbon Filtrasorb 400 (particle size 600-900 μm, F600-900) and Mead Westvaco Nuchar RGC30 (granulometric range 600-1000 μm, N.RGC30).

Two different ionic liquids were tested as impregnating agents of the selected solids (supplied by Sigma Aldrich): 1-hexyl-3-methylimidazolium tetrafluoroborate [Hmim][BF₄] (molecular weight: 254 g mol⁻¹) which is a typical physical solvent towards CO₂ and 1-ethyl-3-methylimidazolium glycine [Emim][Gly] (molecular weight: 185 g mol⁻¹) an amino acid-based IL which is able to form carbamate with carbon dioxide (Zhang et al., 2006a; Kasahara et al., 2012). The ILs molecular structures are reported in Figure 4.1.



Figure 4.1 Molecular structures of (a) [Hmim][BF₄] and (b) [Emim][Gly] ILs

The adsorbents impregnation was carried out as follows: the substrate was contacted in a batch stirred system with an IL solution (liquid to solid ratio equal to 5.4 mL g⁻¹) at two different active phase initial concentrations (5.6×10⁻³ and 2.2×10⁻² M). After 1 week the solid was separated from the liquid solution by filtration and oven dried at 100°C overnight. In order to completely remove the solvent, ethyl acetate in the case of [Hmim][BF₄] and methanol for [Emim][Gly], a further evaporation step was required. In particular, for [Hmim][BF₄] impregnated activated carbons, the solvent was removed by feeding pure N₂

(flow rate equal to 60 NL h⁻¹, for 1 h) at 180°C into a column packed with the impregnated solid while in the case of [Emim][Gly] functionalized sorbents, methanol removal was achieved in an oven at 100°C under vacuum for 5 h. It is underlined that the adopted operating conditions for the evaporation stage were chosen on the basis of the different thermal stabilities of the two ILs (lower decomposition temperature for [Emim][Gly], cf. Chapter 5). Moreover, the effectiveness of the evaporation step was validated from previous experiments in which the solids were impregnated only with the solvents: complete solvent removal was verified by weighing the sorbent before and after thermal treatment. For an easy identification, the functionalized solids were labelled according to the adopted activated carbon, IL and impregnation concentration as:

- F600-900 and N.RGC30 for raw activated carbons;
- F600-900 [Hmim][BF₄] 10⁻³ M and 10⁻² M, N.RGC30 [Hmim][BF₄] 10⁻³ M and 10⁻² M for activated carbons impregnated with [Hmim][BF₄] and adopting IL initial impregnation concentrations of 5.6×10⁻³ and 2.2×10⁻² M;
- F600-900 [Emim][Gly] 10⁻³ M and 10⁻² M, N.RGC30 [Emim][Gly] 10⁻³ M and 10⁻² M for activated carbons functionalized with [Emim][Gly] under IL initial impregnation conditions of 5.6×10⁻³ and 2.2×10⁻² M.

4.2 Solids characterization techniques

The solids tested in this work for CO₂ capture experiments were characterized adopting the following techniques: i) CO₂/N₂ porosimetric analyses to determine the solids textural parameters; ii) thermogravimetric analyses (TGA) to evaluate the amount of ionic liquid loaded on each sorbent after the impregnation treatment and for assessing the thermal stability of the active phase confined in the porous substrates. All the analyses have been carried out at the Laboratorio de Materiales Avanzados (LMA), Department of Inorganic Chemistry of Universidad de Alicante (Spain).

4.2.1 CO₂/N₂ porosimetric analyses

Porosimetric analyses were carried out in a home-made fully automated equipment designed and constructed by the Advanced Materials group (LMA), now commercialized as N₂Gsorb-6 (Gas to Materials Technology; www.g2mtech.com), working at -196 and 0°C for N₂ and CO₂ respectively. Adsorption measurements were recorded in the relative pressure (P/P₀) range of 10⁻⁷-1 for nitrogen and 10⁻⁷-0.03 for carbon dioxide. Prior to adsorption runs

each sample was degassed under vacuum at 100°C in order to remove humidity or other volatile impurities. Noteworthy, the degassing procedure did not determine desorption of the ionic liquid from the substrate, as confirmed by TGA analyses carried out on functionalized sorbents before and after vacuum application. Moreover, it is highlighted that CO₂ measurements were conducted only for raw F600-900 and N.RGC30 activated carbons. The reason for this choice is related to the specific interactions establishing between the probe CO₂ gaseous molecules and the ionic liquid dispersed onto the substrate (with a chemical conversion into carbamate occurring in the case of [Emim][Gly]), which could modify the distribution of the active phase inside the sorbent pores, thus leading to a possible incorrect evaluation of the narrow microporosity of the impregnated samples.

The raw N₂/CO₂ adsorption data were processed according to the common models retrievable from literature in order to evaluate the solid microstructural parameters, and in particular:

- the sorbents total pore volume was derived from N₂ adsorption isotherms by applying the Gurvitsch rule for the volume of nitrogen adsorbed at P/P₀=0.97 (Leofanti et al., 1998);
- the total micropore volume was evaluated with Dubinin-Radushkevich (DR) equation (applied in the N₂ isotherm region P/P₀=10⁻⁴-10⁻²) (Morlay and Joly, 2010);
- the apparent surface area was obtained from N₂ adsorption data by means of BET equation applied in the relative pressure range P/P₀=0.01-0.15, which best agreed with criteria proposed by Roquerol et al. (2007) for the applicability of BET method to microporous sorbents;
- the volume of narrow micropores (pore diameter up to 0.7 nm) was evaluated from CO₂ adsorption isotherm at 0°C using the DR equation;
- the absolute pore size distributions were obtained by applying the Quenched-Solid Density Functional Theory (QSDFT) to N₂ adsorption data (Neimark et al., 2009; Silvestre-Albero et al., 2012).

4.2.2 Thermogravimetric analyses (TGA)

Thermogravimetric analyses on both raw and IL-impregnated solids were performed using a TA Instrument SDT 2960 operated in the temperature range 25-400°C under a N₂ inert atmosphere (flow rate 95 mL min⁻¹) at 5°C min⁻¹ scan rate. TGA measurements allowed to follow the sample mass % evolution as a function of the temperature. The comparison of

the thermograms obtained for raw and impregnated materials provided information on the amount of IL loaded on the activated carbons, at each initial active phase concentration adopted for the impregnation procedure. More specifically, a quantitative estimation of the IL adsorbed on the substrate was derived according to the following expression:

$$\%wt_{IL-ads} = \Delta wt.\%_{impr}(\Delta T_{dec-IL}) - \Delta wt.\%_{raw}(\Delta T_{dec-IL}) \quad (4.1)$$

in which $\%wt_{IL-ads}$ is the mass percentage of the IL in the impregnated sorbent, $\Delta wt.\%_{impr}(\Delta T_{dec-IL})$ and $\Delta wt.\%_{raw}(\Delta T_{dec-IL})$ represent the mass percentage losses of the impregnated and raw materials, respectively, in the temperature range in which the pure ionic liquid decomposes ΔT_{dec-IL} (that can be roughly identified from literature data). In particular, the mass loss of the raw material is subtracted to eliminate any contribution determined by volatile matter or humidity desorbing from the substrate during the test.

4.3 Lab-scale plant for CO₂ adsorption/regeneration tests

Figures 4.2 and 4.3 show a schematic representation and a picture of the experimental apparatus designed and built during this PhD project for the execution of dynamic adsorption/regeneration runs.

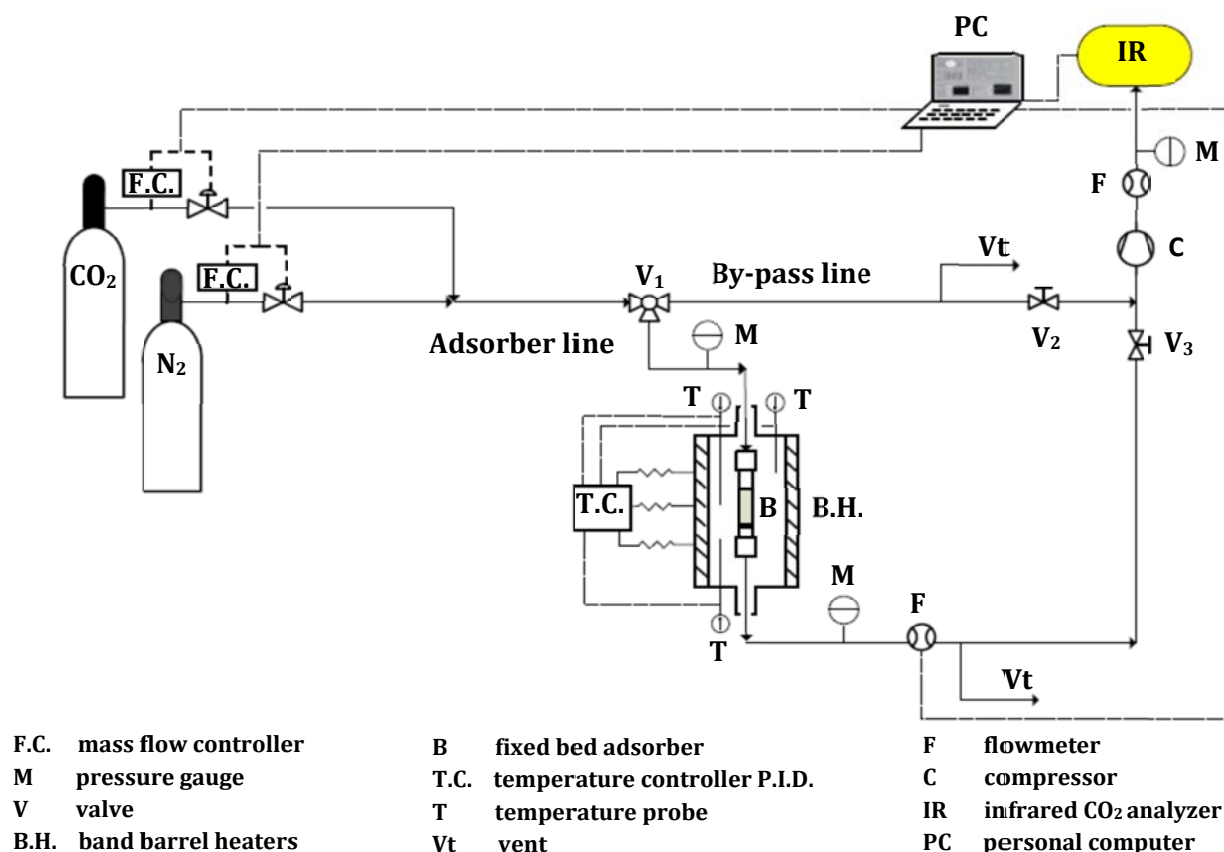


Figure 4.2 Layout of the experimental apparatus

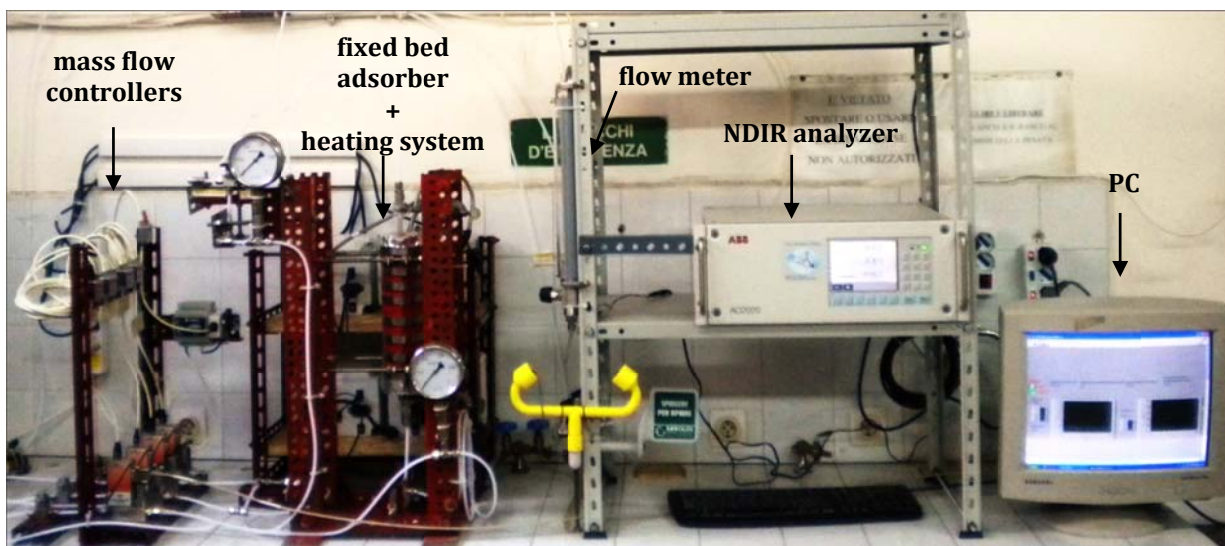


Figure 4.3 Picture of the lab-scale plant for CO₂ adsorption/regeneration tests

The feed gas composition (N₂+CO₂) was determined via mass flow controllers (series El Flow Bronkhorst 201-CV), which allow to generate gaseous streams simulating typical flue-gas compositions (1-15% CO₂ by vol.).

CO₂ adsorption/regeneration tests on the investigated sorbents were carried out in a fixed bed column (length=0.13 m; inner diameter=0.02 m) made up of Pyrex glass, equipped with a 45 μm porous septum and composed of two units for adsorbent charging/discharging operations. The fixed bed temperature was controlled by means of an *ad hoc* heating system, arranged coaxially with the adsorber unit: it consists of three 500 W cylindrical shell Watlow band heaters, enveloped in a thermal insulating layer of ceramic fibers, and connected to EZ-PM[®] PID controllers (Watlow). Before dynamic tests, a calibration curve was built to establish a relationship among band heater surface-band heater/fixed bed interspace-adsorbent granular bed temperatures. Once the thermal profile was known, the fixed bed temperature was defined during adsorption tests by setting and controlling the band heater/fixed bed interspace temperature by means of type J thermocouples.

CO₂ concentration measurements during adsorption/regeneration tests were carried out by a continuous ABB NDIR (non-dispersive infrared) A02020 Uras 26 gas analyzer. Data acquisition and elaboration were performed by interfacing the analyzer with a PC unit via LabView[™] software. Gas volumetric flow rate variations, occurring in the fixed bed, were monitored by means of a mass flow controller series El Flow Bronkhorst 201-CV, set at the exit of the adsorption column, and digitally interfaced with the PC unit for an on-line data acquisition.

A by-pass line was also implemented in the lab-scale apparatus in order to verify the feed composition prior to adsorption experiments: a three way ball valve (V_1) allows to adequately switch the gas flow while two ball valves (V_2 and V_3) are devoted to avoid back flow towards the excluded line.

4.4 Experimental protocols for fixed bed dynamic experiments

In this Section a description of the experimental protocols and conditions adopted for CO_2 adsorption experiments, adsorption/desorption cycles and regeneration tests will be provided.

4.4.1 Continuous CO_2 adsorption tests

CO_2 continuous adsorption runs required two different steps: a) plant preparation; b) test execution. A schematic description of the experimental protocol is provided in the following.

a) Plant preparation

- Charge of reactor (column) with a known adsorbent amount previously heated overnight at 105°C to remove humidity;
- Fill of the remaining part of the column with inert glass beads to uniform the gaseous flow at the column inlet;
- Check of the defined CO_2 concentration by NDIR analyzer, directing the gaseous stream through the by-pass line with valve V_3 closed to avoid back flow in the adsorber line;
- Flush of all plant pipelines with nitrogen to eliminate the presence of atmospheric air;
- Check of gas leakage for all pipelines connections in presence of a nitrogen gas stream;
- Check of column leakage by closing the solenoid valve of the mass flow controller placed at the adsorber outlet, pressurizing with N_2 and monitoring the pressure with pressure gauges.

b) Test execution

- Injection of the defined N_2 and CO_2 volumetric flow rates via mass flow controllers through the by-pass line for 30 s and venting to the atmosphere with valve V_2 closed to reach a stationary value of concentration;
- Switching of the gaseous stream toward the adsorber line via three way valve V_1 and simultaneously acquiring the NDIR concentration signal.

The sorbents CO₂ capture performances have been investigated under the following experimental conditions adopted for the fixed-bed reactor:

- Sorbent dose: 15 g for F600-900 derived sorbents and 13 g for N.RGC30 based materials;
- Total gas flow rate: 2.5×10^{-2} L s⁻¹ (evaluated at T=20°C and P=1 bar);
- CO₂ initial concentration: 1-30% by vol., balance N₂;
- Temperature: 30, 50 and 80°C;
- Total gas pressure: 1 bar.

It is underlined that for N.RGC30 sorbents (raw and ILS-impregnated) experiments were conducted using a lower solid amount because of the lower density of this substrate (13 g of solid completely filled the column). In addition, CO₂ capture tests at initial pollutant concentrations greater than typical 15% flue-gas (namely 25 and 30%) were performed in order to better interpret the qualitative trend of the adsorption isotherms.

The dynamic behavior of the gas-solid adsorption system was followed by monitoring the concentration of the adsorbate at the column outlet as a function of time, obtaining the breakthrough curves. In particular the time evolution of the composition profile was expressed in terms of the ratio of the volumetric flow rates of CO₂ species at the bed outlet relative to that in the feed $Q_{CO_2}^{out}(t)/Q_{CO_2}^{in}$.

CO₂ kinetic adsorption results at 30, 50 and 80°C were processed to obtain the corresponding adsorption isotherms. The material balance on CO₂ over the adsorption column, leads to the following expression for the equilibrium CO₂ specific adsorption capacity ω_{eq} [mmol g⁻¹] (see Section 3.2):

$$\omega_{eq} = \frac{Q_{CO_2}^{in} \rho_{CO_2}}{m M_{CO_2}} \int_0^{t^*} \left(1 - \frac{Q_{CO_2}^{out}(t)}{Q_{CO_2}^{in}} \right) dt \quad (4.2)$$

where ρ_{CO_2} [mg L⁻¹] represents the pollutant density (evaluated at 20°C and 1 bar) while M_{CO_2} [mg mmol⁻¹] is its molecular weight; m [g] is the sorbent dose and t^* [s] represents the time required for reaching complete solid saturation. The time evolution of the CO₂ volumetric flow rate at the column outlet $Q_{CO_2}^{out}(t)$ was obtained from NDIR analyzer which provides this measure by following the temporal variations of the gaseous composition as reported in eq. (4.3):

$$Q_{\text{CO}_2}^{\text{out}}(t) = \frac{Q_{\text{N}_2} \frac{C_{\text{CO}_2}^{\text{out}}(t)}{100}}{\left(1 - \frac{C_{\text{CO}_2}^{\text{out}}(t)}{100}\right)} \quad (4.3)$$

in which $C_{\text{CO}_2}^{\text{out}}(t)$ represents the CO_2 time-dependent percentage volumetric concentration in the gaseous stream at the column outlet.

The resolution of the integral in eq. (4.2) for each investigated inlet CO_2 concentration, was obtained by applying the trapezoidal rule to the experimental kinetic data.

It should be observed that in eq. (4.3) it is assumed that the N_2 volumetric flow rate Q_{N_2} is practically constant during the test: this means that N_2 adsorption on all the tested sorbents is negligible. This hypothesis was experimentally verified, prior to CO_2 adsorption tests, by injecting pure N_2 ($2.5 \times 10^{-2} \text{ L s}^{-1}$) through the adsorber charged with each investigated sorbent and measuring the gas flow rate at the column outlet by means of a mass flow meter.

4.4.2 Adsorption/desorption cycles and regeneration tests

Adsorption/desorption cycles and preliminary regeneration tests were carried out on the sorbent which displayed the highest CO_2 capture capacity among the investigated experimental conditions (namely raw F600-900, cf. Chapter 5).

For adsorption/desorption cycles realization, F600-900 raw was first saturated with a 15% CO_2 in N_2 gas mixture under the same conditions of total gas flow rate, pressure and sorbent dosage previously described (adsorption step). Subsequently, the packed column was flushed with pure N_2 to remove adsorbed CO_2 (desorption step), until its concentration reached the NDIR analyzer low detection limit (0.1% by vol.). This procedure was reiterated for 10 consecutive adsorption/desorption cycles at 30°C .

Regeneration tests were conducted in order to define the optimal operating conditions for CO_2 recovery from the spent activated carbon. To this end, a gaseous stream containing CO_2 at 15% by vol. (total flow rate = $2.5 \times 10^{-2} \text{ L s}^{-1}$, $P=1 \text{ bar}$) was continuously fed to the adsorber ($m=15 \text{ g}$, $T=30^\circ\text{C}$) until equilibrium conditions were reached. After, the packed bed was heated up to the defined temperature for the desorption step (approximately 1 h required to reach thermal equilibrium conditions), a fixed amount of pure N_2 as desorbing agent was sent through the column and CO_2 concentration was monitored by means of the NDIR analyzer. This desorption step was carried out at 60 and 100°C and, for each temperature level, three N_2 flow rates were tested ($6.95 \times 10^{-3} \text{ L s}^{-1}$, $1.11 \times 10^{-2} \text{ L s}^{-1}$ and $1.39 \times 10^{-2} \text{ L s}^{-1}$, evaluated at $T=20^\circ\text{C}$ and $P=1 \text{ bar}$).

The regeneration profiles were elaborated to obtain the total specific amount of CO₂ desorbed from the activated carbon ω_{des} [mmol g⁻¹], through a material balance similar to that reported in Eq. (4.2):

$$\omega_{\text{des}} = \frac{\rho_{\text{CO}_2}}{mM_{\text{CO}_2}} \int_0^{t_{0.1}} Q_{\text{CO}_2}^{\text{out}}(t) dt \quad (4.4)$$

in which $t_{0.1}$ is the time required to complete the desorption process, assumed as the one corresponding to the NDIR low detection limit (0.1% CO₂ by vol.).

CO₂ concentration profiles were also quantitatively analysed to define the best experimental conditions for an efficient regeneration process in terms of CO₂ recovery amount, time required for the desorption process (at a fixed regeneration level) and CO₂ concentration in the desorbing flow, the latter being a critical aspect for CO₂ storage purposes. To this aim, four different characteristic desorption times (t_{50} , t_{70} , t_{80} , t_{90}) have been considered, each corresponding to a different CO₂ recovery percentage of the total adsorbed amount (e.g. t_{50} corresponds to a 50% of total CO₂ recovered by desorption). Consequently, the mean CO₂ concentration in the desorbing flow ($\bar{C}_{\text{CO}_2}^i$) up to the time t_i can be expressed as:

$$\bar{C}_{\text{CO}_2}^i = \frac{V_{\text{CO}_2}^i}{V_{\text{CO}_2}^i + V_{\text{N}_2}^i} = \frac{\int_0^{t_i} Q_{\text{CO}_2}^{\text{out}}(t) dt}{\int_0^{t_i} Q_{\text{CO}_2}^{\text{out}}(t) dt + Q_{\text{N}_2}^{\text{des}} t_i} \quad (4.5)$$

in which $V_{\text{CO}_2}^i$ and $V_{\text{N}_2}^i$ represent the CO₂ total volume desorbed and the purge gas volume fed to the column up to time t_i , respectively. The values of $V_{\text{N}_2}^i$ and $\bar{C}_{\text{CO}_2}^i$ were computed for variable CO₂ recovery percentage i.e. $i=50\%$, 70% , 80% and 90% for each investigated N₂ purge flow rate ($Q_{\text{N}_2}^{\text{des}}$) and desorption temperature ($T_{60^\circ\text{C}}^{\text{des}}$ and $T_{100^\circ\text{C}}^{\text{des}}$).

CHAPTER 5

RESULTS AND DISCUSSION

In this Chapter the main results obtained from solids characterization techniques and adsorption/regeneration experiments will be discussed with a particular emphasis on the intertwining among adsorbents microstructural properties and their CO₂ capture performances. Finally, the results derived from both thermodynamic and kinetic modelling of adsorption data will be analysed.

5.1 Adsorbents characterization

5.1.1 Porosimetric analyses for F600-900 raw and impregnated with [Hmim][BF₄]/[Emim][Gly]

Figures 5.1 and 5.2 show the N₂ adsorption-desorption isotherms at -196°C obtained for the sorbents F600-900 raw and impregnated with [Hmim][BF₄]/[Emim][Gly] ILs at initial active phase concentrations $C^{\circ}=5.6\times 10^{-3}$ and 2.2×10^{-2} M. As a general consideration, it can be observed that the isotherms for all the samples are very similar and they are type I according to IUPAC classification (Patrick, 1995) and the strong adsorption observed at very low relative pressures (i.e. $P/P_0 < 10^{-3}$) testifies the presence of a highly developed microporous structure (Morlay and Joly, 2010). A comparison between the adsorption and desorption branches testifies the non-negligible presence of mesopores: the narrow hysteresis loop observed from isotherms is of type H4 according to IUPAC, commonly associated with the presence of slit-shaped pores (Morlay and Joly, 2010). In addition, it can be observed that the volume of N₂ adsorbed reduces as the IL concentration increases for both active phases with respect to the parent material above all in the “knee” region of the adsorption isotherms ($P/P_0 < 0.1$): this is a clue of the preferential adsorption of both ILs in the substrate micropores.

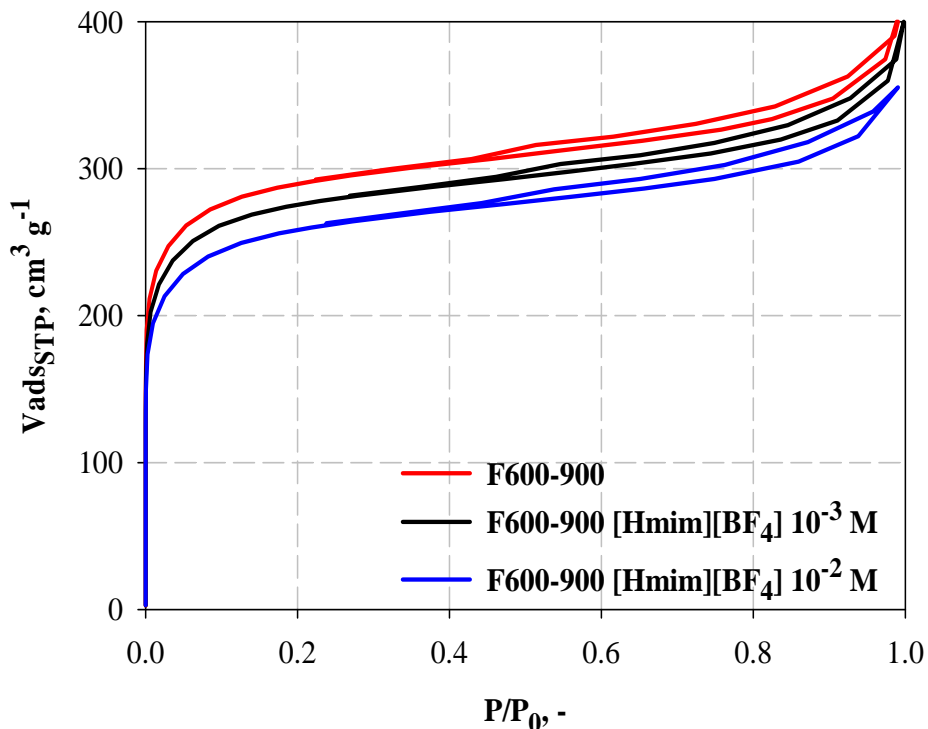


Figure 5.1 N₂ adsorption-desorption isotherms at -196°C for F600-900 raw and impregnated with [Hmim][BF₄] at C°=5.6×10⁻³ and 2.2×10⁻² M

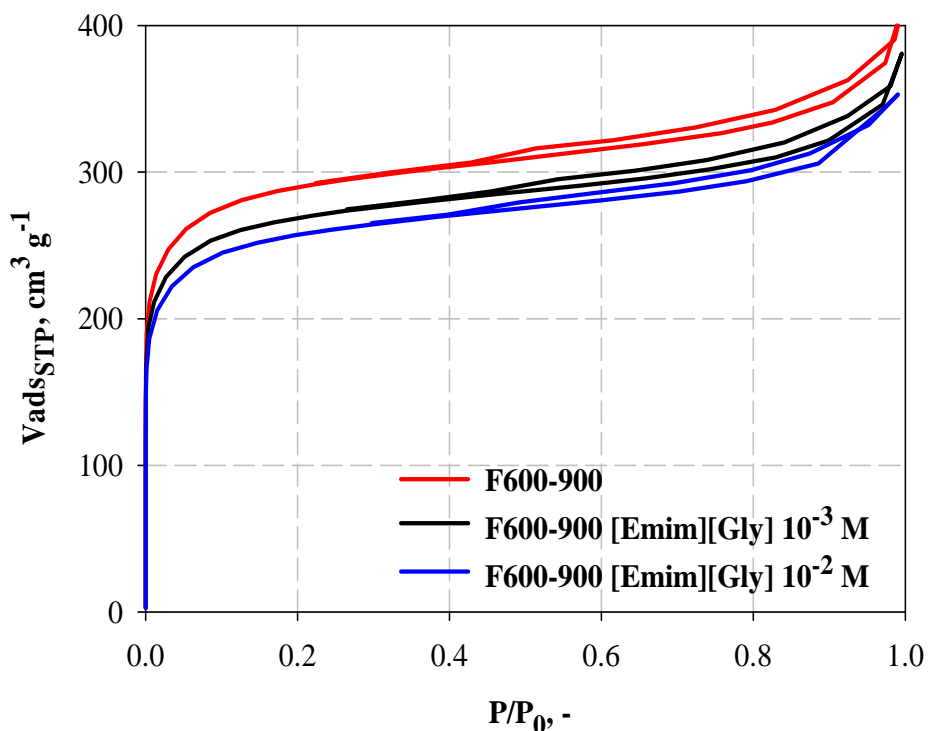


Figure 5.2 N₂ adsorption-desorption isotherms at -196°C for F600-900 raw and impregnated with [Emim][Gly] at C°=5.6×10⁻³ and 2.2×10⁻² M

Table 5.1 reports the apparent surface area (S_{BET}), the total specific pore volume (V_t), the specific micropore volume (V_0) and the specific mesopore volume ($V_{meso} = V_t - V_0$) determined for both raw and [Hmim][BF₄]/[Emim][Gly] impregnated sorbents by applying the models

indicated in Section 4.2.1 to N₂ adsorption data at -196°C. The volume of narrow micropores (V_n) derived for raw F600-900 from CO₂ adsorption isotherm at 0°C is also included.

Table 5.1 Textural parameters obtained for F600-900 raw and impregnated with [Hmim][BF₄]/[Emim][Gly] ILs

Sample	S _{BET} [m ² g ⁻¹]	V _t [cm ³ g ⁻¹]	V ₀ [cm ³ g ⁻¹]	V _n [cm ³ g ⁻¹]	V _{meso} [cm ³ g ⁻¹]
F600-900	1076	0.58	0.41	0.32	0.17
F600-900 [Hmim][BF₄] 10⁻³ M	1018	0.55	0.39	n.a.†	0.16
F600-900 [Hmim][BF₄] 10⁻² M	961	0.52	0.36	n.a.†	0.16
F600-900 [Emim][Gly] 10⁻³ M	1029	0.55	0.39	n.a.†	0.16
F600-900 [Emim][Gly] 10⁻² M	971	0.52	0.36	n.a.†	0.16

† not available

Results highlight a prevailing microporous nature for all the investigated sorbents (for F600-900 raw micropores contribute to a nearly 70% of the total pore volume), thus confirming the observations derived from the analysis of the N₂ adsorption isotherms. Moreover, a comparison between the microstructural parameters of raw and ILs functionalized F600-900 shows a decrease of both S_{BET} and V₀ values when the initial concentration of each ionic liquid increases, while the mesopore volume reduction is not significant. These observations confirm that both ILs partially obstruct only the micropores of the raw material. Finally, at fixed impregnation condition [Hmim][BF₄] and [Emim][Gly] ILs determine the same micropore volume reduction.

Figures 5.3 and 5.4 depict the absolute pore size distributions (PSD) obtained for F600-900 raw and functionalized with [Hmim][BF₄]/[Emim][Gly] ionic liquids by applying the QSDFT method to N₂ adsorption data at -196°C and assuming a slit-shape geometry for pores. The plots are expressed in terms of the ratio between the differential variation of the specific pore volume relative to that of the pore diameter (dV_p(d)) as a function of the pore diameter (d). Results confirm the highly microporous nature of all the samples analysed with a prevailing contribution of pores smaller than 10 Å. The pore size distributions for ILs-impregnated F600-900 adsorbents show similar qualitative patterns with respect to the raw material except for a slight reduction of dV_p(d) values in the pore diameter region smaller than 10 Å and due to the already described partial micropore clogging.

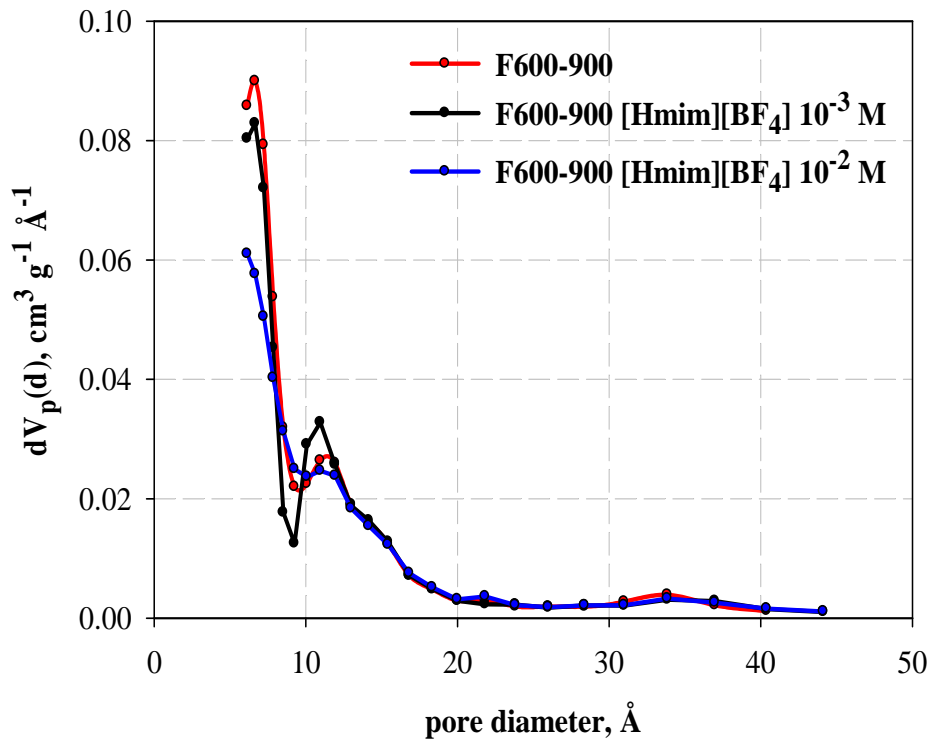


Figure 5.3 Absolute pore size distributions for F600-900 raw and impregnated with [Hmim][BF₄] at $C^\circ=5.6 \times 10^{-3}$ and 2.2×10^{-2} M

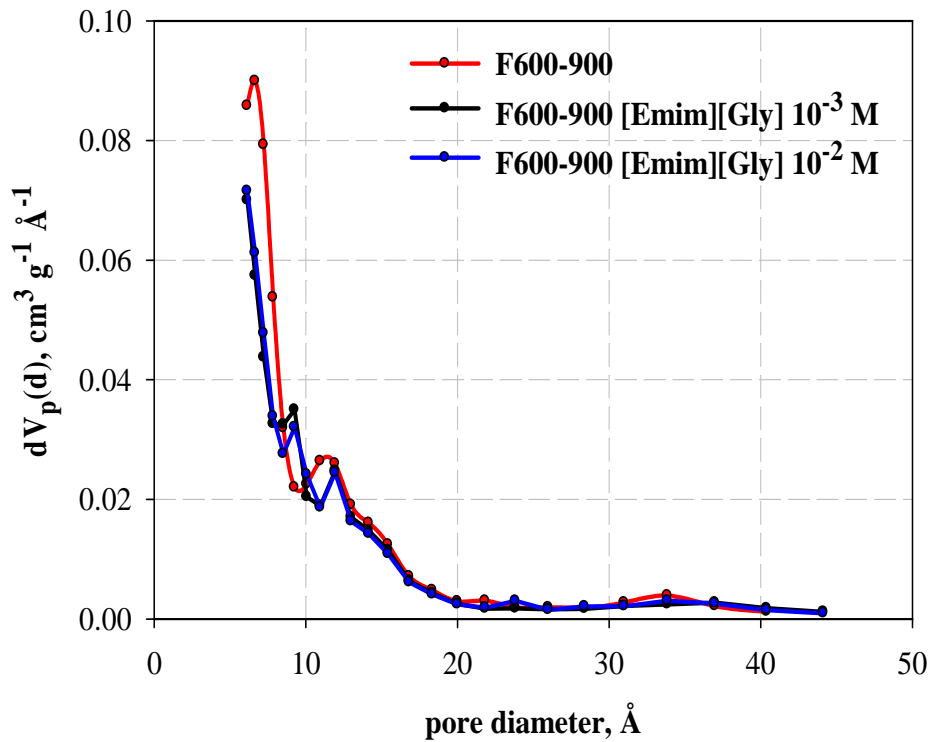


Figure 5.4 Absolute pore size distributions for F600-900 raw and impregnated with [Emim][Gly] at $C^\circ=5.6 \times 10^{-3}$ and 2.2×10^{-2} M

5.1.2 TGA analyses for F600-900 raw and impregnated with [Hmim][BF₄]/[Emim][Gly]

Figures 5.5 and 5.6 show the results obtained from thermogravimetric analyses carried out on raw and ILs-impregnated F600-900 in terms of sample mass percentage as a function of the temperature. Thermograms show for all materials a weight loss (1-3%) for temperatures lower than 100°C which can be likely ascribed to the desorption of humidity or other volatile impurities. Moreover, for F600-900 [Hmim][BF₄] solids the mass loss detectable in the temperature range 280-380°C (clearly identifiable for the sample impregnated under more concentrated conditions, Figure 5.5) can be ascribed to the IL decomposition, in accordance with published research findings concerning TGA analyses for the pure ionic liquid (Crosthwaite et al., 2005). Finally, for [Emim][Gly] impregnated adsorbents the ionic liquid decomposition can be approximately located in the T-range 170-330°C (Muhammad et al., 2011), as confirmed by the different slopes of the thermograms for these materials with respect to raw F600-900 in the same temperature range.

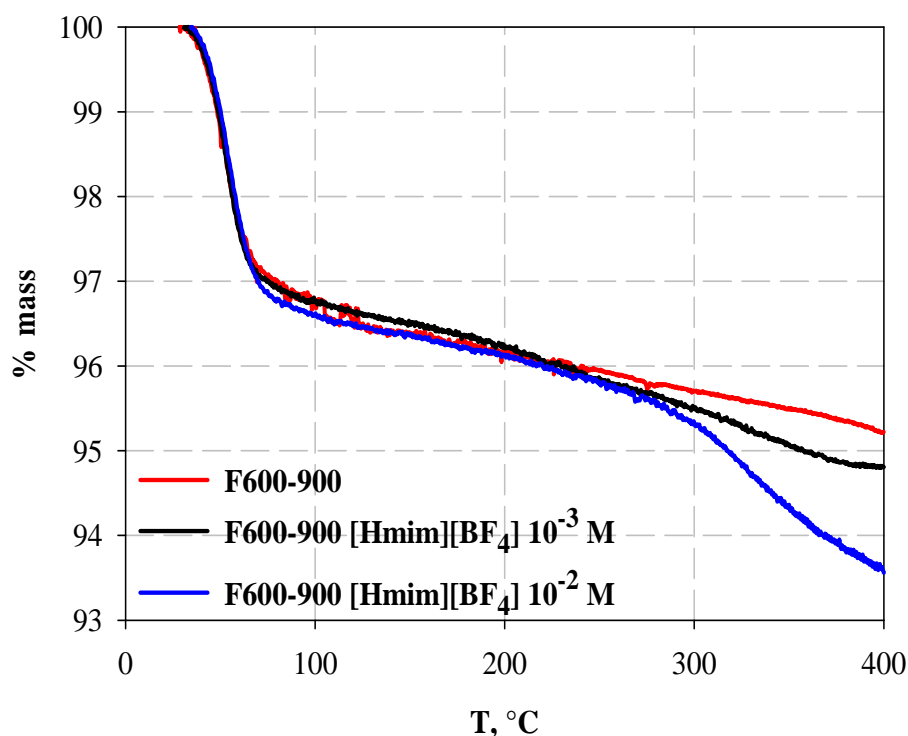


Figure 5.5 Thermogravimetric analyses for F600-900 raw and impregnated with [Hmim][BF₄] at C°=5.6×10⁻³ and 2.2×10⁻² M

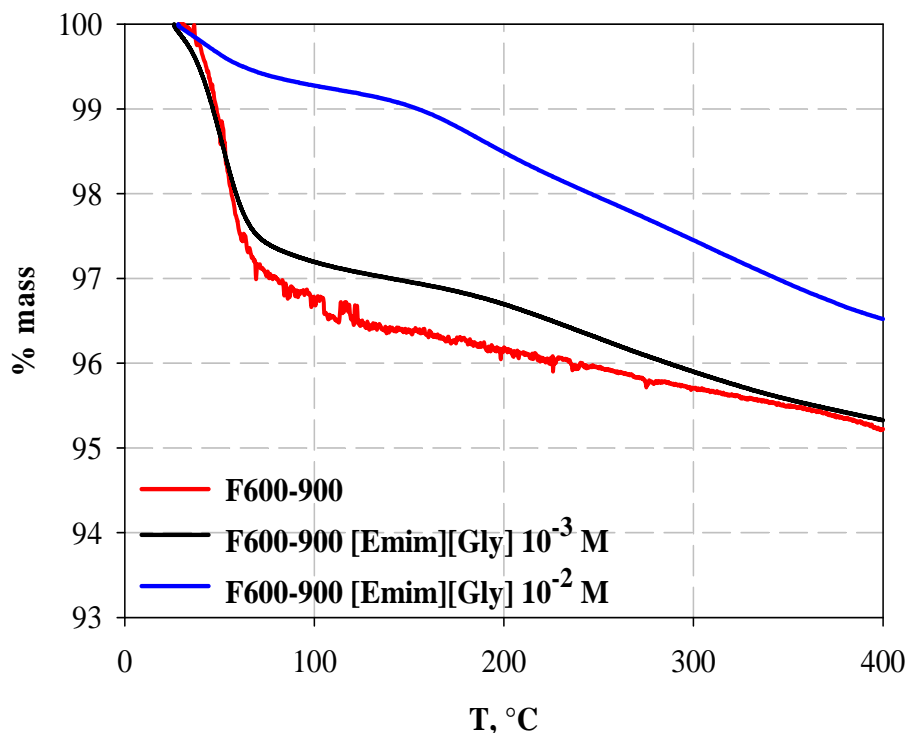


Figure 5.6 Thermogravimetric analyses for F600-900 raw and impregnated with [Emim][Gly] at $C^{\circ}=5.6 \times 10^{-3}$ and 2.2×10^{-2} M

The comparison of the mass loss profiles for each impregnated sorbent with respect to raw F600-900 allowed to estimate the amount of ionic liquid adsorbed on the substrate according to the numerical procedure described in Section 4.2.2 (eq. (4.1)). Table 5.2 reports a comparison of the active phase mass percentage adsorbed on the substrate ($\%wt_{IL-ads}$) with respect to the one initially used for the impregnation procedure ($\%wt_{IL-load}$) for both [Hmim][BF₄] and [Emim][Gly] ILs. Quantitative results are also conveniently expressed in terms of both IL specific molar amount initially loaded ($mmol_{IL-load} g^{-1}AC$) and the IL molar specific adsorption capacity of F600-900 (AC) ($mmol_{IL-ads} g^{-1}AC$).

Table 5.2 Quantitative parameters derived from TGA analyses for F600-900 impregnated with [Hmim][BF₄] and [Emim][Gly] ILs

Sample	$\%wt_{IL-load}$	$\%wt_{IL-ads}$	$mmol_{IL-load} g^{-1}AC$	$mmol_{IL-ads} g^{-1}AC$
F600-900 [Hmim][BF₄] 10^{-3} M	0.76	0.38	0.030	0.015
F600-900 [Hmim][BF₄] 10^{-2} M	2.98	1.29	0.121	0.052
F600-900 [Emim][Gly] 10^{-3} M	0.56	0.51	0.030	0.028
F600-900 [Emim][Gly] 10^{-2} M	2.19	1.04	0.121	0.057

Results evidence that for [Hmim][BF₄]-adsorbents nearly 50% and 43% of the initial amount of IL used for the impregnation is adsorbed on the substrate for $C^{\circ}=5.6 \times 10^{-3}$ and 2.2×10^{-2} M,

respectively. The estimated adsorption efficiencies are 93% and 47% for F600-900 [Emim][Gly] 10^{-3} M and 10^{-2} M respectively. Finally, under more concentrated conditions the amount of [Emim][Gly] adsorbed is slightly higher than in the case of [Hmim][BF₄] (0.057 vs. 0.052 mmol g⁻¹) while it is almost double for C°=5.6×10⁻³ M (0.028 vs. 0.015 mmol g⁻¹).

5.1.3 Porosimetric analyses for N.RGC30 raw and impregnated with [Hmim][BF₄]/[Emim][Gly]

N₂ porosimetric results at -196°C for N.RGC30 raw and functionalized with [Hmim][BF₄] and [Emim][Gly] ionic liquids are depicted in Figures 5.7 and 5.8.

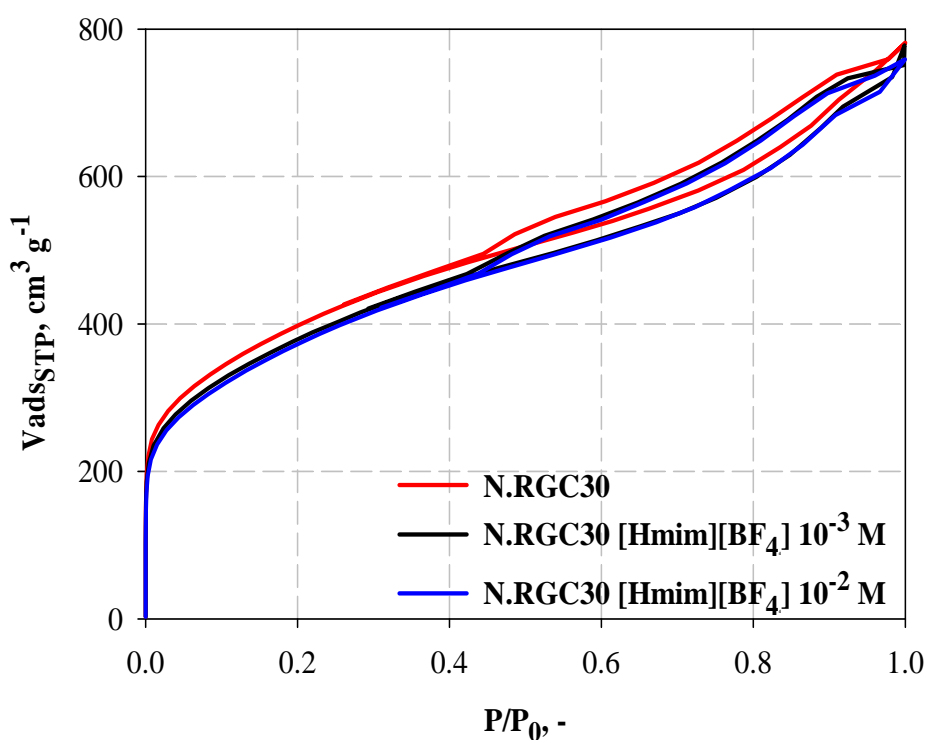


Figure 5.7 N₂ adsorption-desorption isotherms at -196°C for N.RGC30 raw and impregnated with [Hmim][BF₄] at C°=5.6×10⁻³ and 2.2×10⁻² M

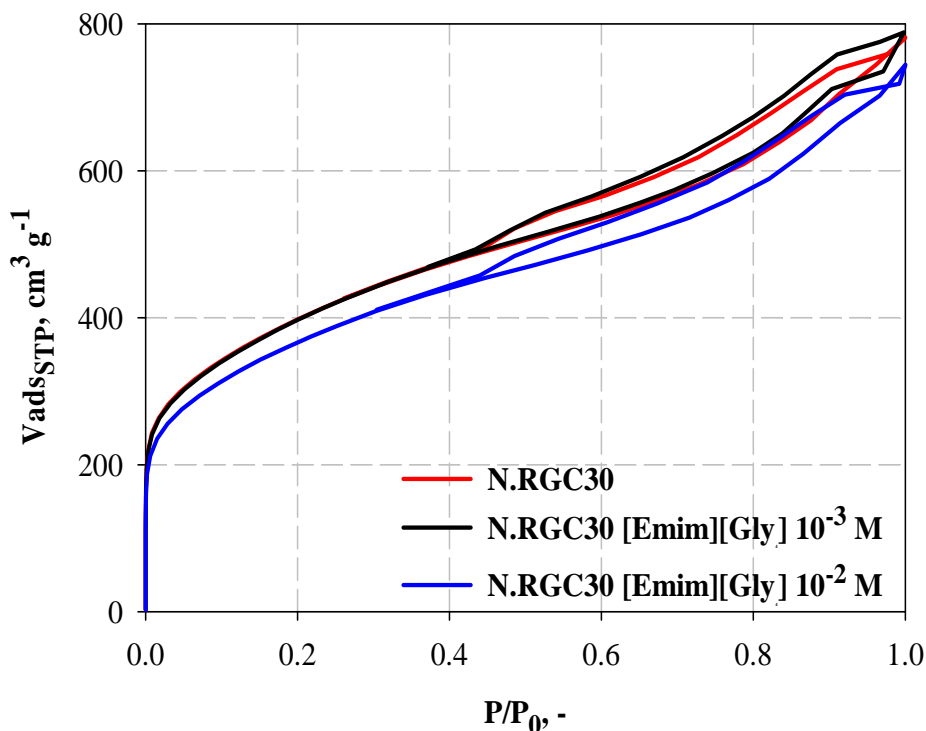


Figure 5.8 N_2 adsorption-desorption isotherms at -196°C for N.RGC30 raw and impregnated with [Emim][Gly] at $C^\circ=5.6\times 10^{-3}$ and 2.2×10^{-2} M

Isotherms are mixed type I and IV and in all the cases with a high adsorption capacity at low relative pressures which testifies the significant presence of micropores, while the observed hysteresis loops indicate a well-developed mesoporosity for all the investigated samples. In addition, for both [Hmim][BF₄] adsorbents it can be observed a reduction of N_2 adsorbed volume with respect to the parent activated carbon, and their adsorption isotherms almost overlap (a slightly higher adsorption capacity for the sample impregnated under more diluted conditions is detected for $P/P_0 < 10^{-3}$). In the case of [Emim][Gly] materials, a more marked reduction of N_2 adsorption capacity is observed under more concentrated impregnation conditions, while for the sample obtained at $C^\circ=5.6\times 10^{-3}$ M differences with raw N.RGC30 can be detected only at low relative pressures (with a slight decrease of N_2 adsorbed volume for the impregnated material at $P/P_0 < 10^{-2}$).

The main microstructural parameters obtained from CO_2 porosimetric analysis at 0°C (only raw N.RGC30) and N_2 adsorption data at -196°C are summarized in Table 5.3. Results underline a prevailing mesoporous nature for N.RGC30 activated carbon with a 57% contribution to the overall porosity; moreover, the significant difference between V_0 and V_n values suggests the presence of a broad micropore size distribution for this sample (Krutyeva et al., 2009). A comparison between V_0 and V_{meso} values indicates the preferential micropore occlusion induced by each IL, this being more important as the initial concentration of active

phase used for the impregnation process increases. Finally, it can be observed that under more diluted conditions [Hmim][BF₄] IL determines a higher micropore volume reduction, while this effect is comparable for both ionic liquids at C°=2.2x10⁻² M.

Table 5.3 Textural parameters obtained for N.RGC30 raw and impregnated with [Hmim][BF₄]/[Emim][Gly] ILs

Sample	S _{BET} [m ² g ⁻¹]	V _t [cm ³ g ⁻¹]	V ₀ [cm ³ g ⁻¹]	V _n [cm ³ g ⁻¹]	V _{meso} [cm ³ g ⁻¹]
N.RGC30	1427	1.15	0.50	0.32	0.65
N.RGC30 [Hmim][BF ₄] 10 ⁻³ M	1350	1.12	0.47	n.a.†	0.65
N.RGC30 [Hmim][BF ₄] 10 ⁻² M	1318	1.11	0.46	n.a.†	0.65
N.RGC30 [Emim][Gly] 10 ⁻³ M	1418	1.14	0.49	n.a.†	0.65
N.RGC30 [Emim][Gly] 10 ⁻² M	1307	1.11	0.46	n.a.†	0.65

† not available

Pore size distributions obtained for N.RGC30 raw and functionalized with [Hmim][BF₄]/[Emim][Gly] ionic liquids are reported in Figures 5.9 and 5.10. Results confirm the presence of a broad micropore size distribution and a significant contribution of mesopores with a mesopores-peak centred approximately at 35 Å. In addition, both ionic liquids do not affect remarkably the raw material PSD, apart from little differences for pore diameters lower than 10 Å which can be ascribed to the already observed pore occlusion effect (Table 5.3).

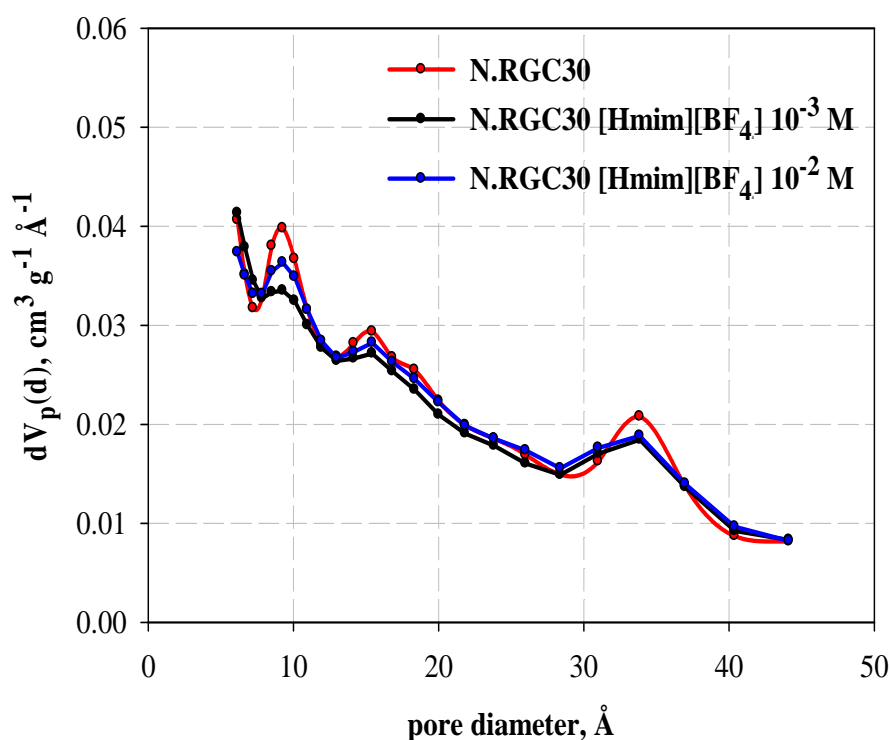


Figure 5.9 Absolute pore size distributions for N.RGC30 raw and impregnated with [Hmim][BF₄] at C°=5.6x10⁻³ and 2.2x10⁻² M

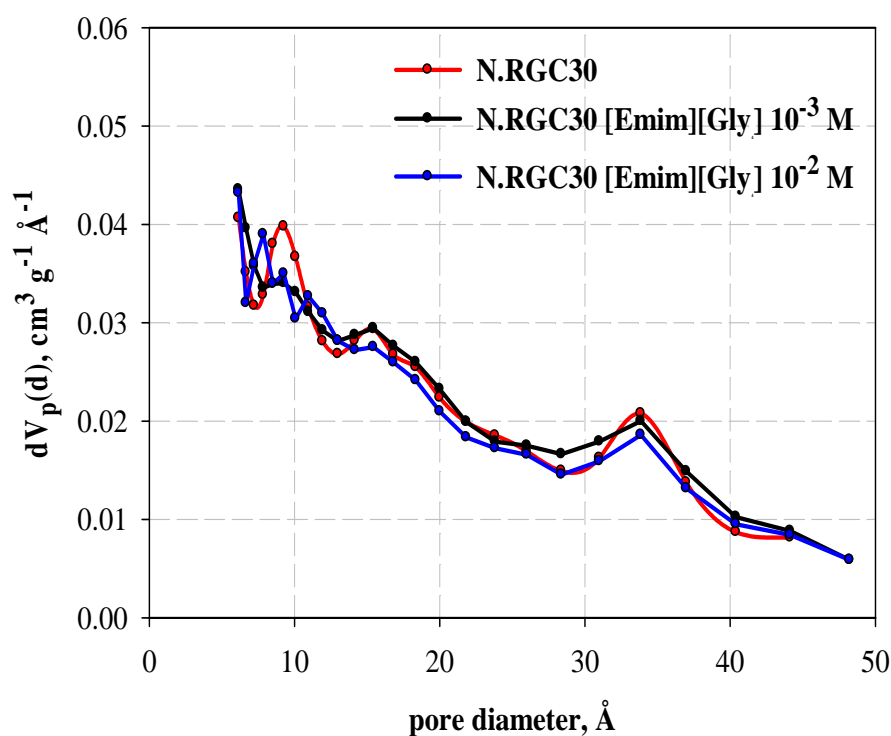


Figure 5.10 Absolute pore size distributions for N.RGC30 raw and impregnated with [Emim][Gly] at $C^\circ=5.6\times 10^{-3}$ and 2.2×10^{-2} M

5.1.4 TGA analyses for N.RGC30 raw and impregnated with [Hmim][BF₄]/[Emim][Gly]

Thermogravimetric patterns derived for N.RGC30 both raw and impregnated with [Hmim][BF₄] and [Emim][Gly] ILs at $C^\circ=5.6\times 10^{-3}$ and 2.2×10^{-2} M are shown in Figures 5.11 and 5.12. Experimental results show that apart from the desorption of humidity and volatile matter observed for temperature lower than 100°C, the thermal decomposition range for each ionic liquid practically coincides with that observed for F600-900 functionalized sorbents (cf. Figures 5.5 and 5.6): 280-380°C and 170-330°C for [Hmim][BF₄] and [Emim][Gly] respectively. This observation leads to the conclusion that the different microstructural properties of F600-900 and N.RGC30 activated carbons do not affect remarkably the thermal stability of the ionic liquids investigated.

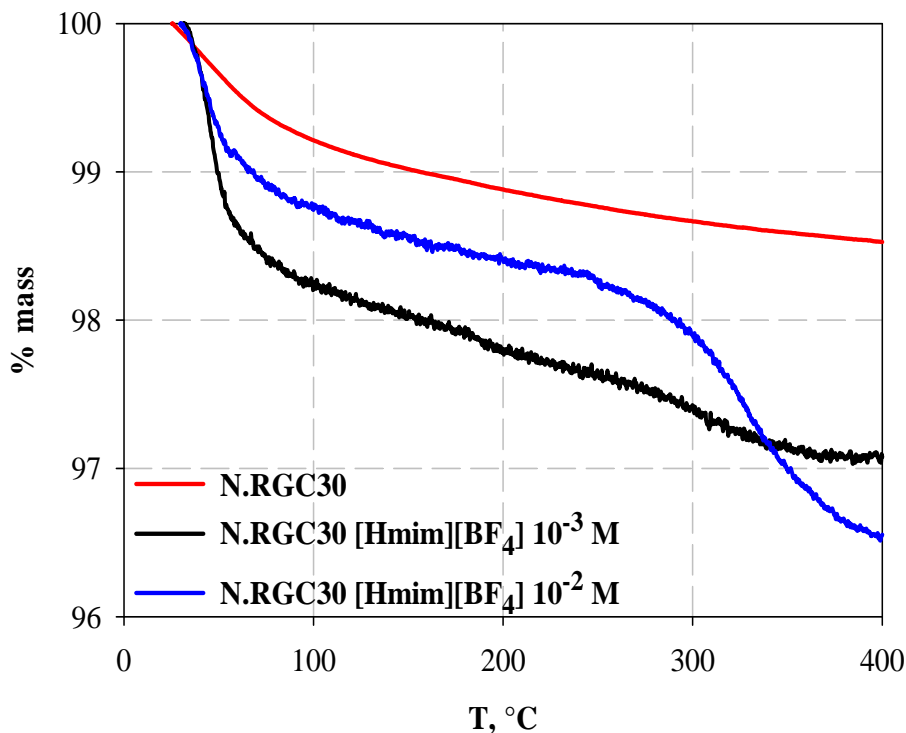


Figure 5.11 Thermogravimetric analyses for N.RGC30 raw and impregnated with [Hmim][BF₄] at C°=5.6×10⁻³ and 2.2×10⁻² M

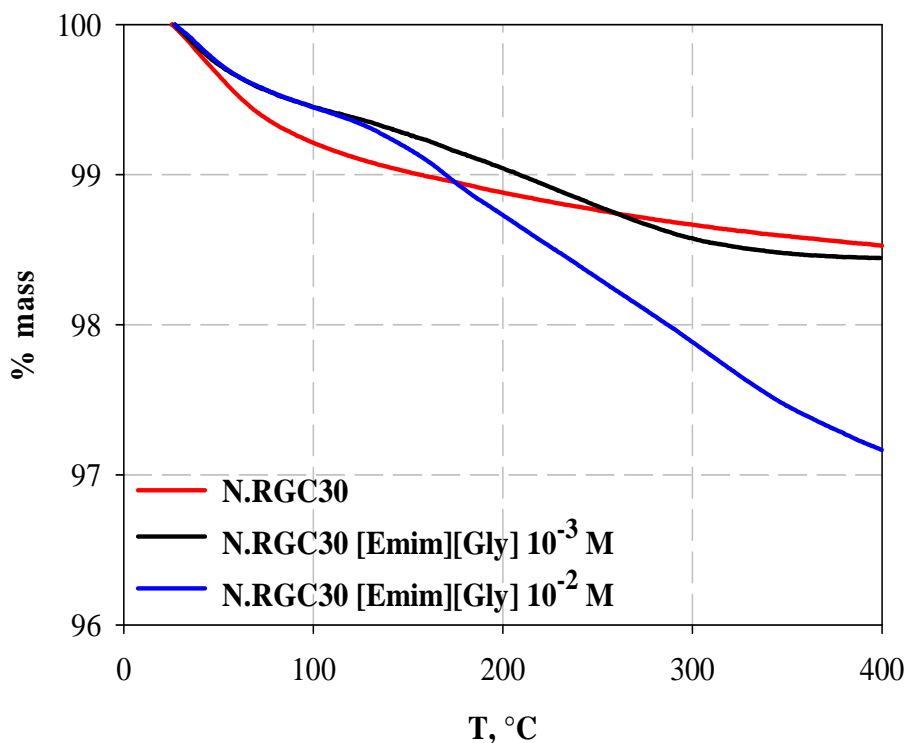


Figure 5.12 Thermogravimetric analyses for N.RGC30 raw and impregnated with [Emim][Gly] at C°=5.6×10⁻³ and 2.2×10⁻² M

The comparison of the mass loss profiles between the raw material and the impregnated ones allowed an estimation of the amounts of each ionic liquid adsorbed on N.RGC30 sorbents; the main derived parameters are schematically reported in Table 5.4. In general, it

can be observed that the adsorption efficiencies are higher in the case of [Emim][Gly] ionic liquid (90% and 47% for $C^{\circ}=5.6 \times 10^{-3}$ and 2.2×10^{-2} M, respectively), while similar active phase uptake efficiencies were recorded for N.RGC30 [Hmim][BF₄] 10^{-3} and 10^{-2} M (43% and 42% under more diluted and concentrated impregnation conditions, respectively).

Table 5.4 Quantitative parameters derived from TGA analyses for N.RGC30 impregnated with [Hmim][BF₄] and [Emim][Gly] ILs

Sample	%wt_{IL-load}	%wt_{IL-ads}	mmol_{IL-load} g⁻¹AC	mmol_{IL-ads} g⁻¹AC
N.RGC30 [Hmim][BF₄] 10⁻³ M	0.76	0.32	0.030	0.013
N.RGC30 [Hmim][BF₄] 10⁻² M	2.98	1.28	0.121	0.051
N.RGC30 [Emim][Gly] 10⁻³ M	0.56	0.49	0.030	0.027
N.RGC30 [Emim][Gly] 10⁻² M	2.19	1.04	0.121	0.057

5.1.5 Comparison between TGA and porosimetric analyses for the investigated sorbents

The main parameters derived from thermogravimetric and porosimetric analyses for F600-900 and N.RGC30 both raw and impregnated with [Hmim][BF₄]/[Emim][Gly] ionic liquids are summarized in Table 5.5. The percentage reduction of the total micropore volume derived for each impregnated material with respect to the parent one $(V_{0\text{-raw}} - V_{0\text{-impr}}) / V_{0\text{-raw}}$ (with $V_{0\text{-raw}}$ and $V_{0\text{-impr}}$ representing the total micropore volume of the parent and functionalized sorbent, respectively) is also reported for a better understanding of the effect of the impregnation treatment conditions on the microstructural properties of each investigated sorbent. The most interesting aspects deduced from the data analysis are highlighted in the following.

- Raw N.RGC30 is characterized by a broader micropore size distribution with respect to F600-900, as confirmed by the higher difference between V_0 and V_n values (Kruttyeva et al., 2009), and displays a remarkably higher contribution of mesopores (V_{meso} is nearly fourfold the value obtained for F600-900).
- [Hmim][BF₄] and [Emim][Gly] ILs preferentially adsorb in micropores for both substrates and in general the higher the IL loading, the greater the micropore occlusion.
- For F600-900 impregnated sorbents, even if the specific amount of [Emim][Gly] adsorbed on the substrate is higher than in the case of [Hmim][BF₄] (almost double under more diluted impregnation conditions) the micropore volume reduction is the

same at fixed initial active phase concentration. A similar situation occurs for N.RGC30 materials functionalized at $C^{\circ}=2.2\times 10^{-2}$ M, while at lower initial active phase concentration (5.6×10^{-3} M) [Emim][Gly] produces a micropore volume reduction that is one-third the one observed in the case of [Hmim][BF₄], despite of a double specific amount adsorbed. The described trends can be related to the more branched shape of [Hmim][BF₄] imidazolium ring which is characterized by a C6 side chain (C2 for [Emim][Gly], cf. Section 4.1): the larger cationic size of this ionic liquid determines a similar (or even higher) pore occlusion effect with respect to [Emim][Gly] for lower adsorbed amount.

- A comparison between F600-900 and N.RGC30 impregnated with [Hmim][BF₄] reveals that similar specific amounts of ionic liquid are adsorbed at fixed initial active phase concentration: under more diluted impregnation conditions the micropore volume reduction is comparable for both substrates (4.9 and 6% for F600-900 and N.RGC30 respectively), while the pore clogging effect is more significant for F600-900 at higher IL concentration. Likewise for [Emim][Gly] adsorbents, a similar IL adsorbed amount for both substrates at fixed impregnation condition determines a higher micropore volume reduction for F600-900 activated carbon. These results should be interpreted in the light of the different textural properties of F600-900 and N.RGC30 activated carbons. As a matter of fact, the presence of a narrower micropore size distribution with a prevailing contribution of very small pore diameters (<10 Å, cf. also Figures 5.3 and 5.4) for F600-900 determines a more relevant occlusion effect for each IL and at fixed impregnation condition than in the case of N.RGC30 adsorbent which exhibits a greater contribution of wider pores in the micropores range (cf. Figures 5.9 and 5.10).

The aforementioned analysis is considered to be an important reference for the subsequent discussion concerning the effects of the different adsorbents microstructural properties on their CO₂ capture performances.

Table 5.5 Main parameters derived from porosimetric and TGA analyses for F600-900 and N.RGC30 raw and impregnated with [Hmim][BF₄] and [Emim][Gly] ILs

Sample	S _{BET} [m ² g ⁻¹]	V ₀ [cm ³ g ⁻¹]	V _n [cm ³ g ⁻¹]	V _{meso} [cm ³ g ⁻¹]	(V _{0-raw} - V _{0-impr}) / V _{0-raw} %	mmol _{IL-ads} g ⁻¹ _{AC} (TGA)
F600-900	1076	0.41	0.32	0.17		
F600-900 [Hmim][BF₄] 10⁻³ M	1018	0.39	n.a.†	0.16	4.9	0.015
F600-900 [Hmim][BF₄] 10⁻² M	961	0.36	n.a.†	0.16	12.2	0.052
F600-900 [Emim][Gly] 10⁻³ M	1029	0.39	n.a.†	0.16	4.9	0.028
F600-900 [Emim][Gly] 10⁻² M	971	0.36	n.a.†	0.16	12.2	0.057
N.RGC30	1427	0.50	0.32	0.65		
N.RGC30 [Hmim][BF₄] 10⁻³ M	1350	0.47	n.a.†	0.65	6	0.013
N.RGC30 [Hmim][BF₄] 10⁻² M	1318	0.46	n.a.†	0.65	8	0.051
N.RGC30 [Emim][Gly] 10⁻³ M	1418	0.49	n.a.†	0.65	2	0.027
N.RGC30 [Emim][Gly] 10⁻² M	1307	0.46	n.a.†	0.65	8	0.057

† not available

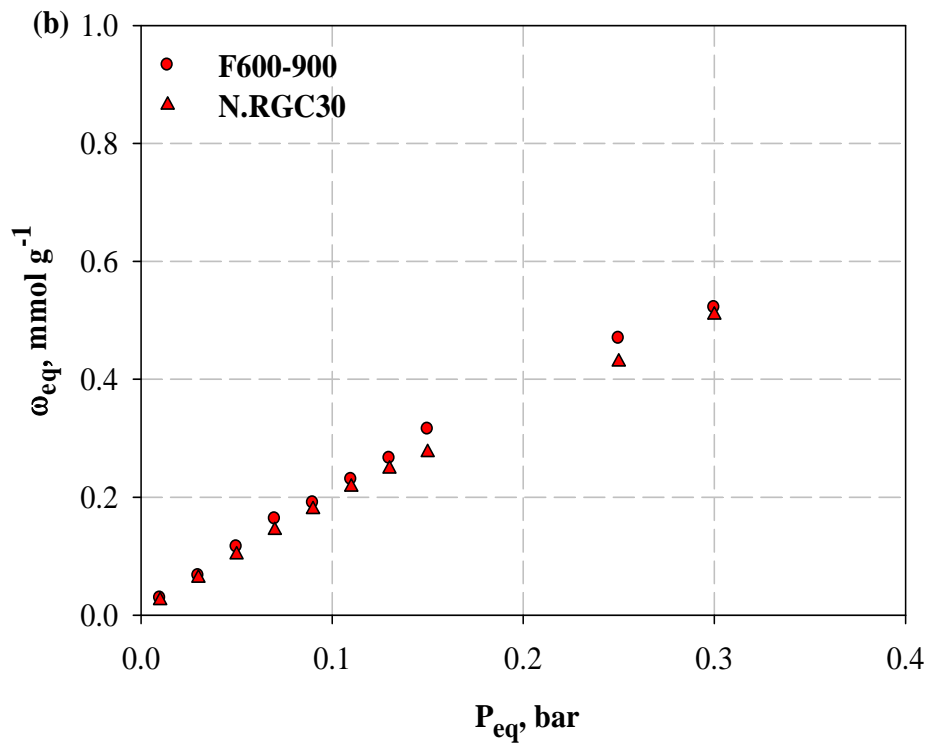
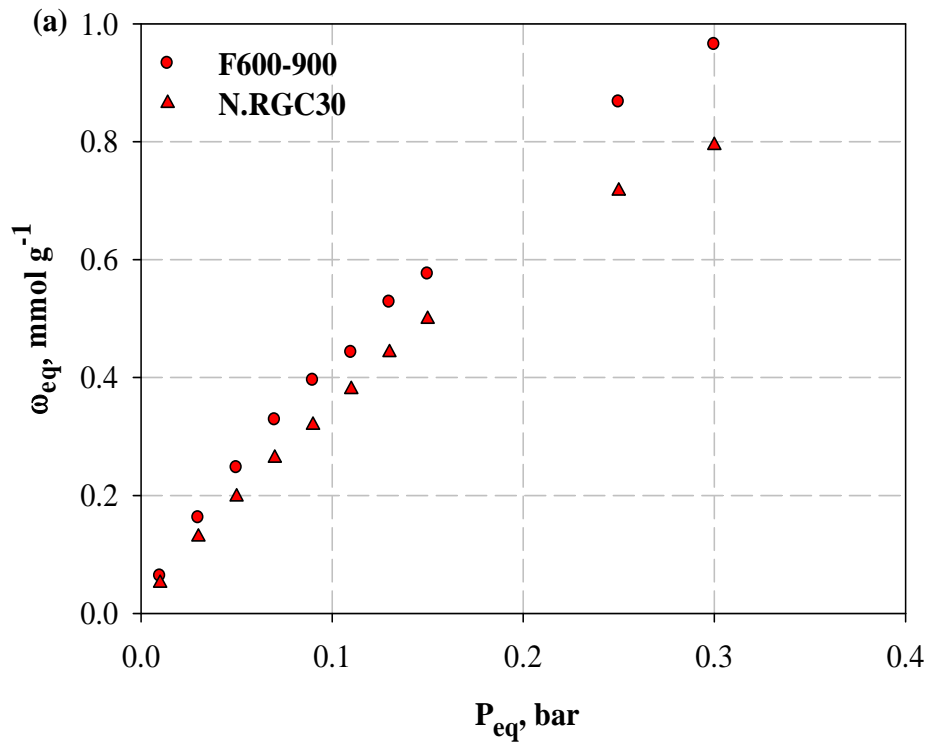
5.2 CO₂ capture performances on the investigated sorbents

5.2.1 CO₂ adsorption tests onto raw F600-900 and N.RGC30

Figure 5.13 depicts CO₂ adsorption isotherms obtained for raw F600-900 and N.RGC30 at (a) 30, (b) 50 and (c) 80°C in terms of the solid molar adsorption capacity ω_{eq} as a function of the pollutant equilibrium partial pressure in the gaseous phase (P_{eq}). It is here recalled that ω_{eq} values were derived by integration of the breakthrough curves obtained from kinetic runs at different CO₂ concentrations (1-30% by vol.) according to the procedure described in Section 4.4.1. Results evidence a reduction of CO₂ adsorption capacity when the temperature increases for both activated carbons, as a consequence of the exothermic character of physisorption (Plaza et al., 2007). In particular, under typical flue gas conditions ($P_{\text{eq}}=0.15$ bar) ω_{eq} is 0.575 mmol g⁻¹ at 30°C for F600-900 which is 1.8- and 4.2-times the values obtained at 50 and 80°C, respectively. Similarly, ω_{eq} for N.RGC30 at $P_{\text{eq}}=0.15$ bar reduces from 0.499 mmol g⁻¹ at 30°C to 0.276 and 0.139 mmol g⁻¹ at 50 and 80°C, respectively. As a general consideration CO₂ adsorption performances obtained in this work for F600-900 and N.RGC30 are comparable with those reported in the literature for raw activated carbons tested under similar experimental conditions (cf. Table 2.1 in Section 2.1.1).

A comparison of F600-900 and N.RGC30 adsorption isotherms at the different operating temperatures reveals that at 30°C the former sorbent displays higher CO₂ removal performances for all investigated pollutant equilibrium partial pressures, while differences reduce at 50°C to become practically negligible at 80°C. These results should be interpreted considering that at lower temperatures physisorption plays a major role in the pollutant capture and its contribution decreases at higher temperatures (Plaza et al., 2007). In this context, on the basis of the sorbents textural properties reported in Section 5.1 (with particular reference to Table 5.5) one would have expected higher CO₂ capture capacities for N.RGC30 sample because of its higher surface area and micropore volume. Nevertheless, as recently highlighted by Whaby et al. (2010 and 2012), the presence of a narrow micropore size distribution with well-defined pore size entrances (mainly pore diameters <5 Å) seems to be a key factor in determining CO₂ adsorption, because in narrow micropores the overlapping potential produces a more effective packing of CO₂ molecules. As a consequence, the narrower micropore size distribution with a prevailing contribution of very small pore diameters (<10 Å) observed for F600-900 solid should be responsible for its higher capture performances at 30°C. At intermediate temperature (50°C) physisorption contribution is less important and

consequently differences in CO₂ sorptive properties between the two activated carbons tend to reduce and become practically negligible at 80°C.



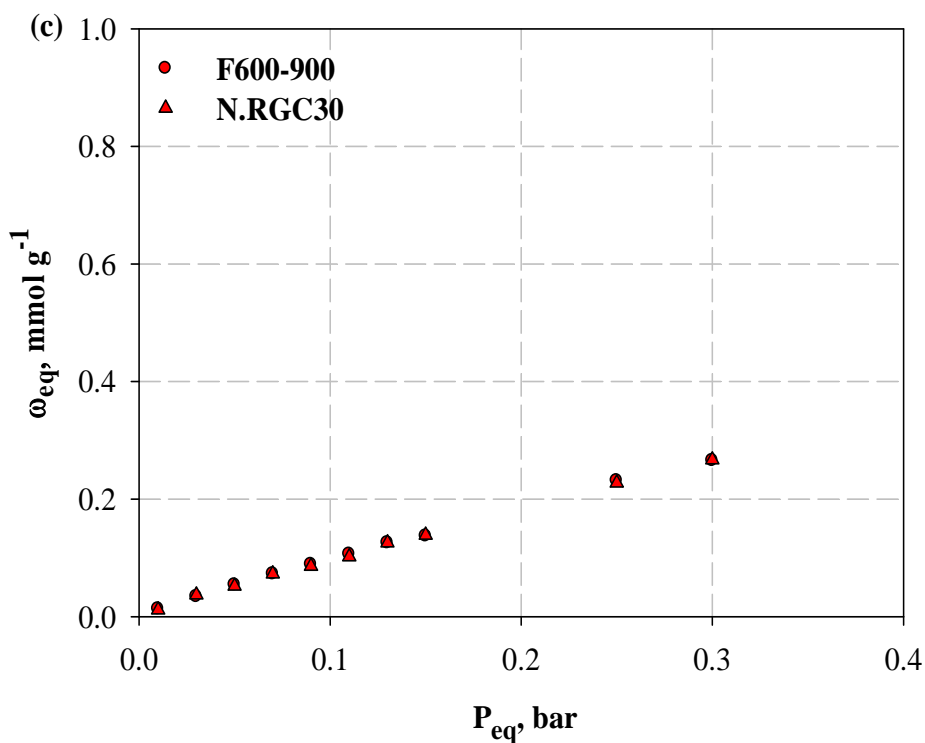


Figure 5.13 CO₂ adsorption isotherms obtained for raw F600-900 and N.RGC30 adsorbents at (a) 30, (b) 50 and (c) 80°C

The raw adsorbents dynamic adsorption performances are compared in Figures 5.14 and 5.15 which report the breakthrough curves of CO₂ on F600-900 and N.RGC30, respectively, at 30, 50 and 80°C adopting a 15% by vol. CO₂-concentrated gaseous stream, representative of a typical flue-gas composition.

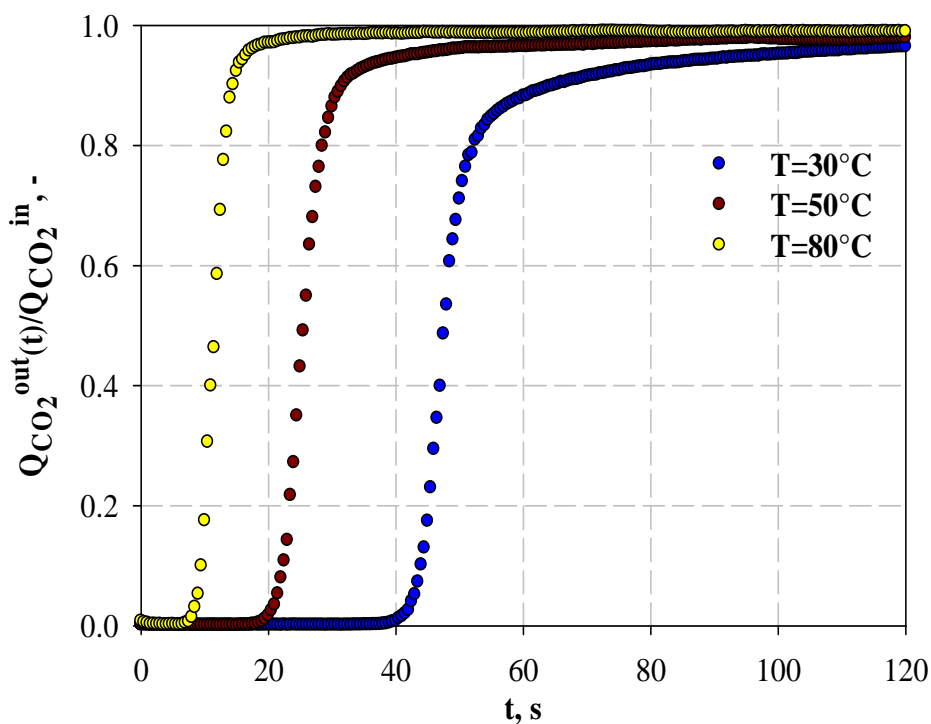


Figure 5.14 Breakthrough curves of CO₂ on raw F600-900 at 30, 50 and 80°C for a 15% by vol. CO₂ gaseous stream

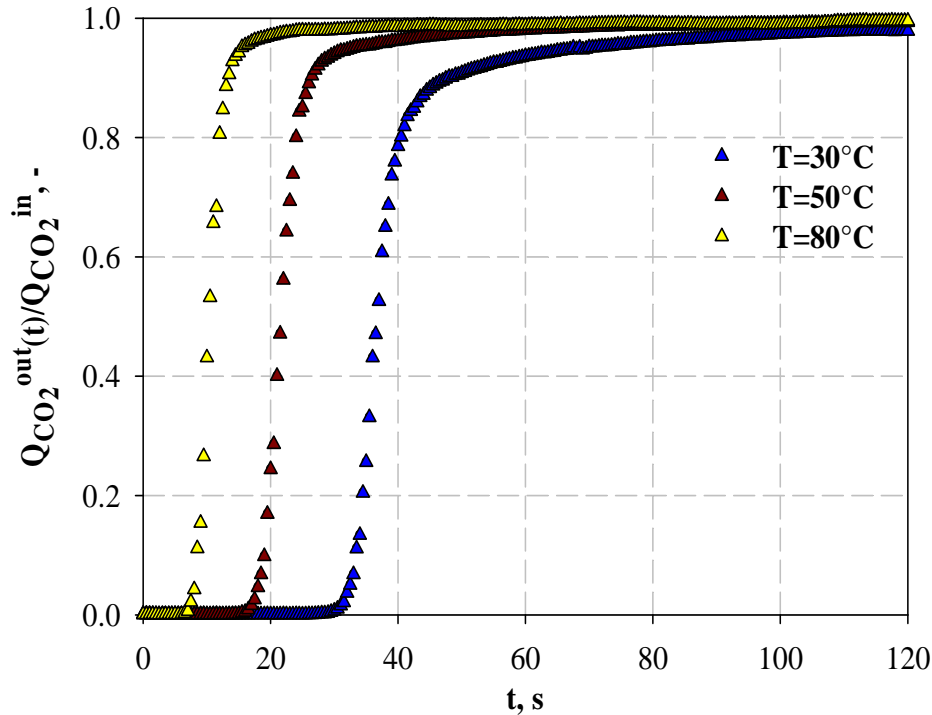


Figure 5.15 Breakthrough curves of CO₂ on raw N.RGC30 at 30, 50 and 80°C for a 15% by vol. CO₂ gaseous stream

As a general consideration, it can be observed that for each activated carbon the breakthrough curve shows a monotonic shift towards lower times as the temperature rises. For instance, the breakpoint time t_b ($Q_{CO_2}^{out}(t)/Q_{CO_2}^{in}=0.05$) is 43 s at 30°C for F600-900, a value 4.8-times greater than the one obtained at 80°C (9 s). In the case of N.RGC30 $t_b=32, 18$ and 8 s for adsorption temperatures of 30, 50 and 80°C. Moreover, higher temperatures determine faster adsorption kinetics as testified by the increasing slope of the sigmoid and the reduction of the equilibrium time t^* (for which CO₂ concentrations at the bed inlet and outlet are practically equal). As a matter of fact, t^* is approximately 2.7- and 2.2-times greater at 30°C with respect to 80°C for N.RGC30 (195 vs. 71 s) and F600-900 (293 vs. 131 s), respectively. These results can be interpreted considering that two factors determine faster adsorption kinetics at higher temperatures: i) the reduction of the adsorption capacity (lower number of active sites to be occupied) which allows higher diffusion rates; ii) an intrinsic increase in intraparticle diffusivity with temperature (mainly in micropores, cf. Sections 3.2 and 5.4.2) (Ruthven, 1984).

Considering that different amounts of F600-900 and N.RGC30 were used for adsorption experiments (15 and 13 g for F600-900 and N.RGC30 respectively, cf. Section 4.4.1), a comparison of the dynamic performances of the two sorbents on the basis of t_b is not feasible because breakthrough curves translate along time axis by varying the sorbent dose under

constant pattern conditions (Ruthven, 1984; McCabe et al., 1993). In this context, differences in mass transfer rates can be better evaluated by introducing a time parameter $\Delta\tau=t_{0.9}-t_b$ (with $t_{0.9}$ being the time for which $Q_{CO_2}^{out}(t)/Q_{CO_2}^{in}=0.9$) which is related to the slope of the linear part of the sigmoid: the smaller this parameter the steeper the breakthrough curve and, consequently, the faster adsorption kinetics. The values of $\Delta\tau$ derived from the kinetic patterns for F600-900 and N.RGC30 raw at 30, 50 and 80°C are listed in Table 5.6 together with the sorbents main microstructural parameters.

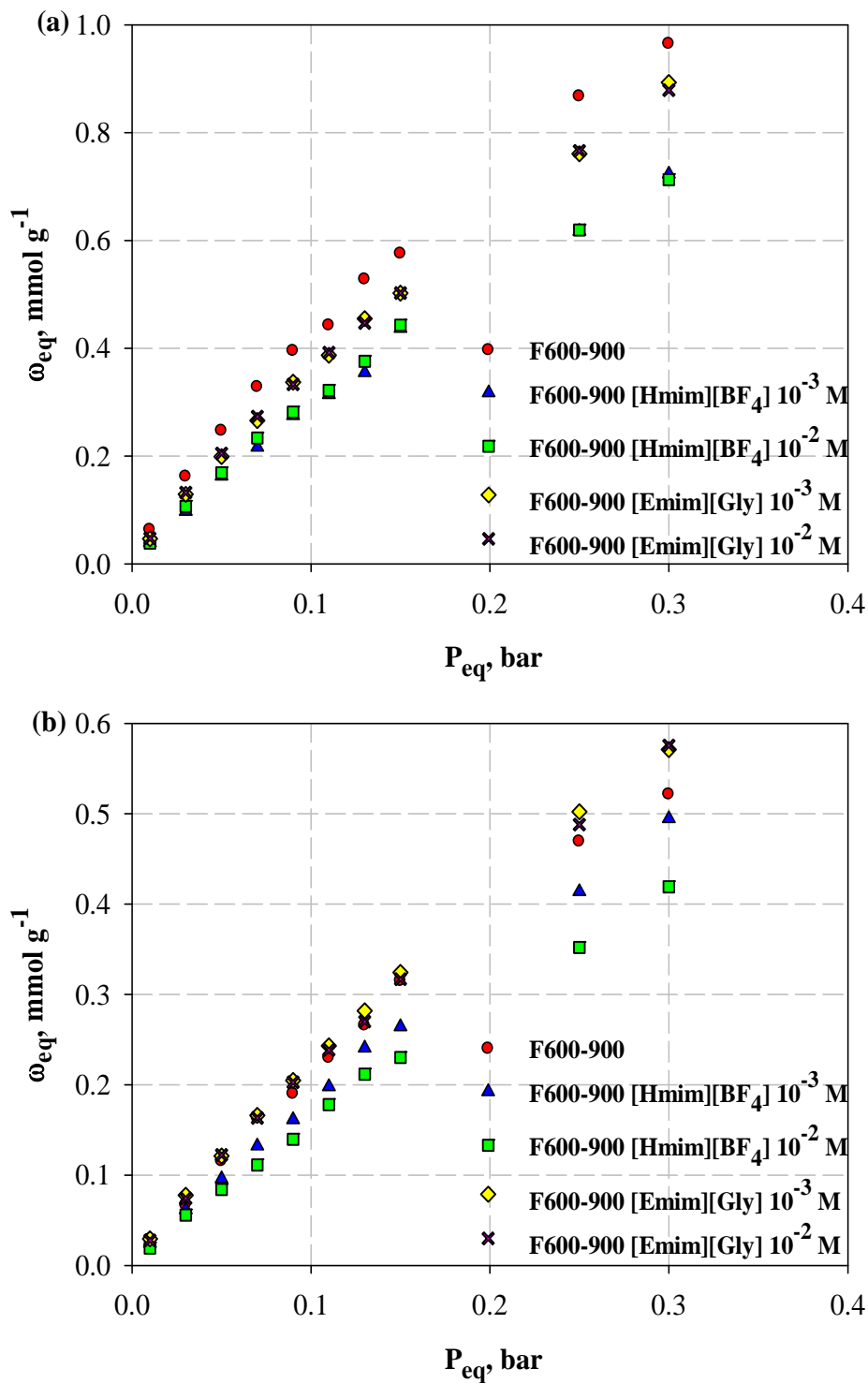
Table 5.6 Comparison between $\Delta\tau$ values obtained from kinetic adsorption tests at 30, 50 and 80°C and the main textural parameters derived for F600-900 and N.RGC30 activated carbons; $C_{CO_2}^{inlet}=15\%$ by vol.

Sample	$\Delta\tau$ [s]			Microstructural parameters		
	T=30°C	T=50°C	T=80°C	V_0 [cm ³ g ⁻¹]	V_n [cm ³ g ⁻¹]	V_{meso} [cm ³ g ⁻¹]
F600-900	22	10	5	0.41	0.32	0.17
N.RGC30	15	8	5	0.50	0.32	0.65

Results show that for each adsorbent $\Delta\tau$ value decreases from 30 to 80°C confirming faster adsorption kinetics at higher temperature; moreover, $\Delta\tau$ is generally higher for F600-900 sorbent with respect to N.RGC30 and differences reduce as the adsorption temperature rises (at 80°C the values practically coincide). These outcomes suggest faster mass transfer rates for N.RGC30 sorbent which can be ascribed to the larger contribution of mesopores ($V_{meso}=0.65$ and 0.17 cm³ g⁻¹ for N.RGC30 and F600-900, respectively) and to the presence of wider micropores (cf. V_0 and V_n values) with respect to F600-900 allowing a quicker diffusion of CO₂ molecules inside the adsorbent pores. The effect of the different textural parameters on the adsorbents dynamic adsorption performances becomes less important from 30 to 80°C because of the already-mentioned increase in intraparticle diffusion rates at higher temperatures.

5.2.2 CO₂ adsorption tests onto F600-900 raw and functionalized with [Hmim][BF₄]/[Emim][Gly]

Figure 5.16 reports CO₂ adsorption isotherms on F600-900 raw and impregnated with [Hmim][BF₄]/[Emim][Gly] ILs at different active phase concentrations and at (a) 30, (b) 50 and (c) 80°C.



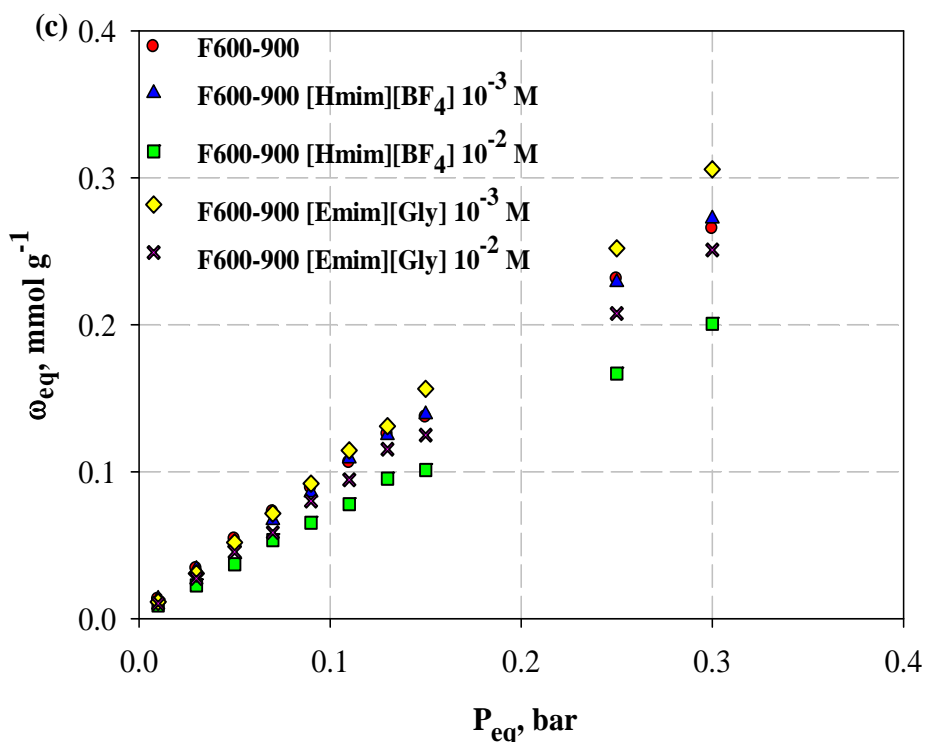


Figure 5.16 CO₂ adsorption isotherms on F600-900 raw and impregnated with [Hmim][BF₄]/[Emim][Gly] ILs at C°=5.6×10⁻³ and 2.2×10⁻² M and at a) 30, (b) 50 and (c) 80°C

A qualitative analysis of the adsorption isotherms denotes the following aspects:

- At 30°C F600-900 raw shows the highest CO₂ capture performances among the tested adsorbents in the whole P_{eq} range investigated. Moreover, [Emim][Gly] sorbents display higher ω_{eq} values with respect to [Hmim][BF₄] materials and adsorption isotherms at different impregnation conditions overlap for each ionic liquid examined.
- At 50°C [Emim][Gly] functionalized sorbents show similar adsorption capacities with respect to the raw material up to P_{eq} =0.15 bar, while an improving of the parent adsorbent capture performances are observed for higher pollutant concentrations; once again, [Hmim][BF₄] materials are characterized by worse adsorption performances which is more evident for the sample impregnated at C°=2.2×10⁻² M.
- At 80°C the ω_{eq} ranking is F600-900 [Emim][Gly] 10⁻³ M>F600-900 raw≈F600-900 [Hmim][BF₄]10⁻³ M>F600-900 [Emim][Gly] 10⁻² M>F600-900 [Hmim][BF₄]10⁻² M.

Before providing a quantitative correlation between the sorbents microstructural properties and their sorption capacities, it is fundamental to underline that many factors contribute in determining a complex phenomenology in CO₂ removal for the investigated systems. In particular, in the case of the raw activated carbon physisorption is the main active mechanism for CO₂ capture and its contribution decreases with temperature (Plaza et al.,

2007). Differently, dealing with impregnated samples, the CO₂ capture determined by the IL and the occlusion of the substrate pores act in opposite directions, the latter leading to a reduction in the contribution of the raw material adsorption. In addition, for both ILs the increase in temperature is detrimental for the capture process: [Hmim][BF₄] acts as a physical solvent towards CO₂ (solubility is typically equal to 0.05 mol_{CO₂}/mol_{IL} at room T and near atmospheric pressure), while [Emim][Gly] includes an amino-group in its structure which is potentially able to form carbamate with carbon dioxide via a reversible exothermic reaction following the same scheme described for commonly employed amine-based solvents (theoretical capture capacity under dry conditions 0.5 mol_{CO₂}/mol_{IL}) (Kim et al., 2005; Plaza et al., 2007; Krumdieck et al., 2008; Zhang et al. 2011; Kasahara et al., 2012). Moreover, the less sterically-hindered [Emim][Gly] molecule makes the access of CO₂ to its active site (amino-group) and in the sorbent pores potentially easier than in the case of [Hmim][BF₄]. Finally, it should be also considered that the dispersion of the active phase into the substrate pores could be altered both by temperature variations (influencing for example the IL surface tension and viscosity) and by interactions establishing with CO₂ molecules (with a further dependence on the amount of pollutant adsorbed).

In light of the aforementioned observations, Table 5.7 reports a comparison of the adsorption capacities obtained for the investigated sorbents under typical flue-gas conditions (CO₂ 15% by vol., $\omega_{\text{eq}}^{15\%}$) and the main quantitative parameters derived from porosimetric and TGA analyses (pore volume reduction and the specific amount of ionic liquid adsorbed on the substrate, see also Table 5.5).

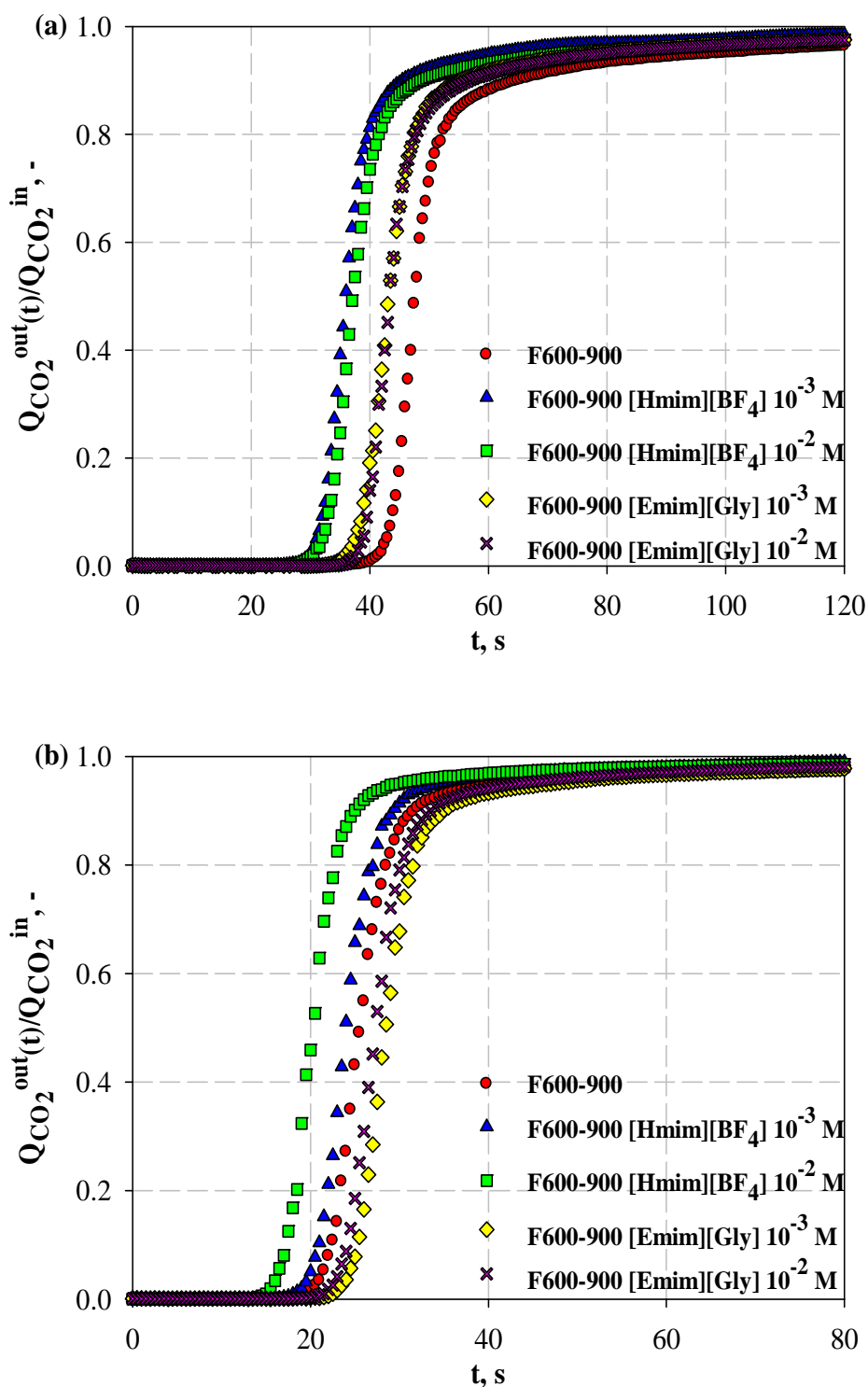
Table 5.7 Comparison among $\omega_{\text{eq}}^{15\%}$ values and the main parameters derived from porosimetric and TGA analyses for F600-900 raw and impregnated with [Hmim][BF₄] and [Emim][Gly] ILs

Sample	$\omega_{\text{eq}}^{15\%}$ [mmol g ⁻¹]			$(V_{0\text{-raw}} - V_{0\text{-impr}}) / V_{0\text{-raw}}$ %	mmol _{IL-ads} g ⁻¹ _{AC} (TGA)
	T=30°C	T=50°C	T=80°C		
F600-900	0.575	0.315	0.137		
F600-900 [Hmim][BF₄] 10⁻³ M	0.437	0.264	0.139	4.9	0.015
F600-900 [Hmim][BF₄] 10⁻² M	0.443	0.230	0.101	12.2	0.052
F600-900 [Emim][Gly] 10⁻³ M	0.502	0.324	0.157	4.9	0.028
F600-900 [Emim][Gly] 10⁻² M	0.502	0.317	0.125	12.2	0.057

Results suggest that at $T=30^{\circ}\text{C}$ the pores blocking induced by the presence of the ILs prevails on their contribution to CO_2 capture, thus determining a reduction of the adsorption performances of the functionalized sorbents with respect to the parent material. Moreover, for each IL, the higher pore volume reduction experienced under more concentrated impregnation condition is counterbalanced by the contribution to CO_2 capture determined by a higher amount of IL loaded. The higher $\omega_{\text{eq}}^{15\%}$ values obtained at 30°C for [Emim][Gly] solids with respect to [Hmim][BF₄] ones could be explained considering that, even if at fixed impregnation condition the pore clogging is the same for both ILs, a greater amount of the amino acid-based ionic liquid is adsorbed on the substrate (almost double at $C^{\circ}=5.6\times 10^{-3}$ M) and its capture capacity towards CO_2 is one order magnitude higher than in the case of [Hmim][BF₄] (0.05 and 0.5 mol_{CO₂}/mol_{IL} for [Hmim][BF₄] and [Emim][Gly] respectively). At 50°C the pore blocking effect on the functionalized sorbents adsorption capacities is generally reduced (due to the decreasing physisorption of the raw material) and it is balanced by the active phase CO_2 -capture contribution in the case of [Emim][Gly], while it persists for less CO_2 -affine [Hmim][BF₄] (to a greater extent for the sample obtained under more concentrated condition for which the pore volume reduction is higher). Finally, at 80°C pore clogging becomes negligible for F600-900 [Hmim][BF₄] 10^{-3} M sample while it is still important for the sample obtained at $C^{\circ}=2.2\times 10^{-2}$ M. Differences between [Hmim][BF₄] adsorbents could be ascribed to a very low CO_2 solubility in the IL at this temperature (even if solubility data at this temperature are not available in the literature), thus under more diluted impregnation condition the lower amount of IL charged and the higher spreading of the IL on the support surface (induced by a reduction of its surface tension) would make easier the access to F600-900 active sites with respect to F600-900 [Hmim][BF₄] 10^{-2} M sample. On the other hand, [Emim][Gly] is able to produce an increase in F600-900 CO_2 capture capacity only under more diluted impregnation condition ($\omega_{\text{eq}}^{15\%}$ is nearly 15% greater with respect to the parent material), thanks to a good compromise between IL loading, CO_2 affinity and pore accessibility, while the pore volume reduction prevails for the sorbent impregnated at $C^{\circ}=2.2\times 10^{-2}$ M.

The breakthrough curves obtained for F600-900 raw and impregnated with [Hmim][BF₄]/[Emim][Gly] ILs at different temperatures and for a 15% CO_2 gas stream are reported in Figure 5.17 ((a) 30°C , (b) 50°C and (c) 80°C).

As a general consideration, it can be observed that, as expected, the increase in the operating temperature determines faster adsorption kinetics for all the impregnated samples with a shift of the breakthrough curves towards lower times as a consequence of higher diffusion rates of CO₂ molecules in the sorbent pores. Moreover, the equilibrium times are approximately 10- and 3-times lower at 80°C with respect to 30°C for [Hmim][BF₄] and [Emim][Gly] sorbents, respectively.



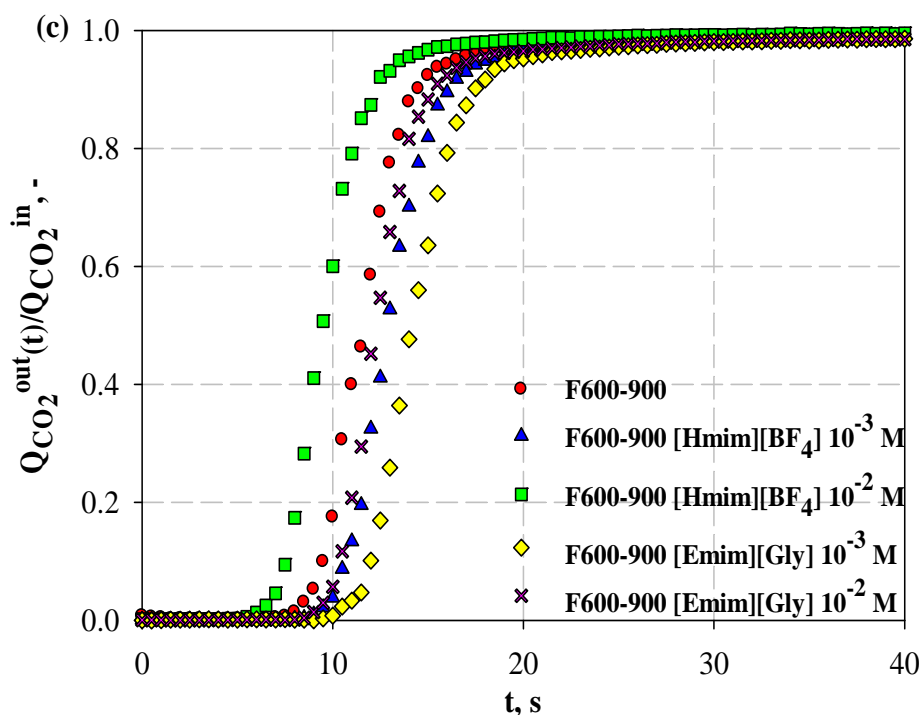


Figure 5.17 Breakthrough curves of CO₂ on F600-900 raw and impregnated with [Hmim][BF₄]/[Emim][Gly] for a 15% by vol. CO₂ gaseous stream at (a) 30, (b) 50 and (c) 80°C

A comparison of the adsorbents dynamic performances is provided in Table 5.8 which lists breakpoint times t_b and $\Delta\tau$ values (cf. Section 5.2.1) obtained from 15% CO₂ adsorption tests at 30, 50 and 80°C.

Table 5.8 Comparison between $\Delta\tau$ and t_b values obtained from kinetic adsorption tests at 30, 50 and 80°C for F600-900 raw and [Hmim][BF₄]/[Emim][Gly]-impregnated; $C_{CO_2}^{inlet}=15\%$ by vol.

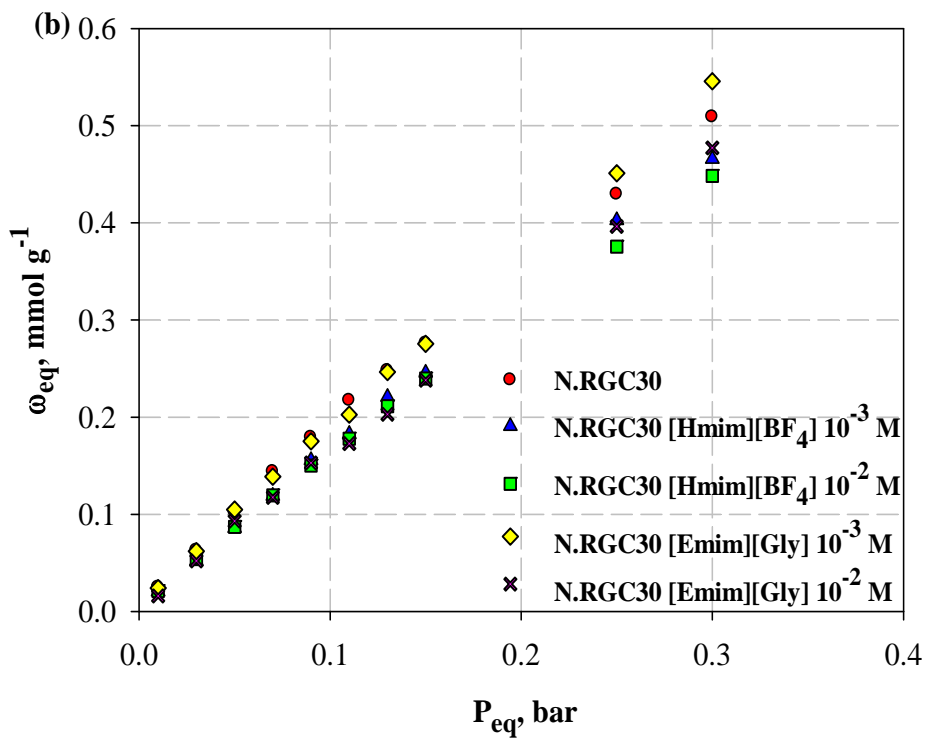
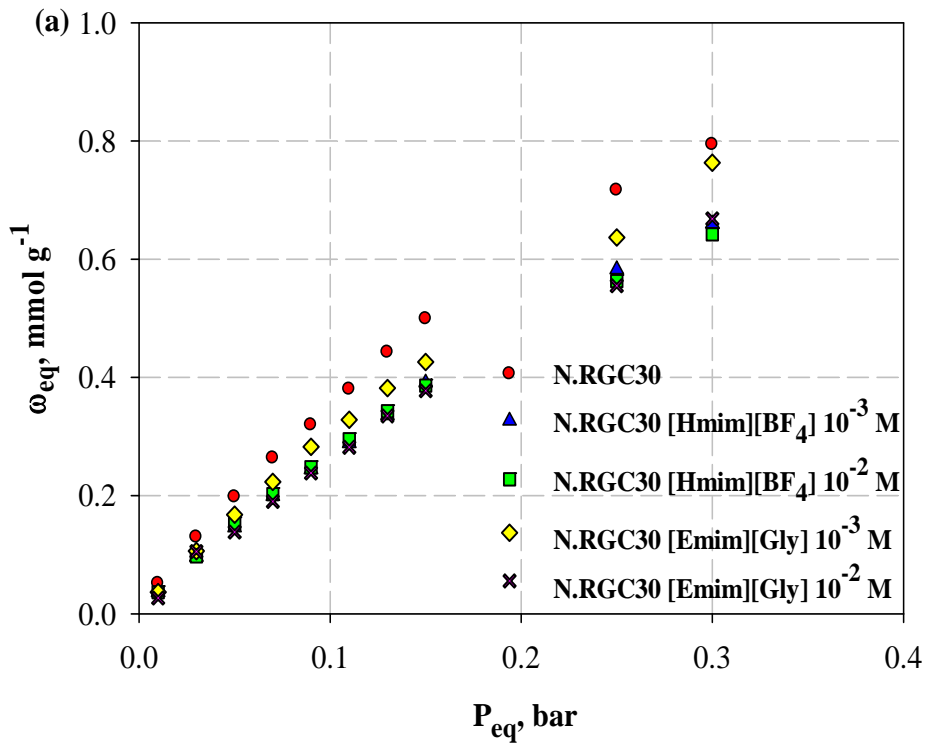
Sample	$\Delta\tau$ [s]			t_b [s]		
	T=30°C	T=50°C	T=80°C	T=30°C	T=50°C	T=80°C
F600-900	22	10	5	43	21	9
F600-900 [Hmim][BF ₄] 10 ⁻³ M	16	9	6	31	20	10
F600-900 [Hmim][BF ₄] 10 ⁻² M	17	9	5	32	16	7
F600-900 [Emim][Gly] 10 ⁻³ M	17	10	6	38	24	11
F600-900 [Emim][Gly] 10 ⁻² M	17	10	6	39	23	10

Results show that the ranking observed for breakpoint times at each temperature generally coincides with the one shown in Table 5.7 in terms of equilibrium adsorption capacities (1 s differences fall within the experimental error). In the case of F600-900

[Emim][Gly] 10^{-2} and 10^{-3} M, t_b values at 50°C are greater with respect to the one obtained for F600-900 raw (21, 24 and 23 s for F600-900 raw, [Emim][Gly] 10^{-3} and 10^{-2} M respectively), even if the adsorption capacities are practically equivalent: obviously, ω_{eq} value also depends on the sorbent capture contribution for times greater than t_b . The analysis of $\Delta\tau$ data highlights that the only significant difference in dynamic performances can be observed at 30°C for which this parameter is greater for F600-900 raw (slower adsorption kinetic) with respect to the impregnated materials (which display similar $\Delta\tau$ values); discrepancies are practically negligible at higher temperatures. This pattern could be explained considering that at lower temperature differences in adsorption capacities of the impregnated samples with respect to the parent one are greater, thus the higher the number of active sites to be occupied (for F600-900 raw) the slower the kinetics. As the temperature rises, ω_{eq} differences reduce and intraparticle diffusivity is higher, determining similar CO_2 capture kinetics. Moreover, it is here recalled that the pore size distribution of the substrate is not appreciably influenced by the impregnation process (cf. Section 5.1) and the only observed effect is a reduction in the total micropore volume (V_{meso} is practically constant): this parameter (V_{micro}) itself is not able to explain kinetic differences between the raw and impregnated materials. Vice versa the distribution of both ILs in the sorbent micropores (width of the IL film, positioning at the pore mouth, complete or partial pore filling etc.), which can be also influenced by the temperature and the capture process itself, is likely a further factor affecting the sorption kinetics for the impregnated samples.

5.2.3 CO₂ adsorption tests onto N.RGC30 raw and functionalized with [Hmim][BF₄]/[Emim][Gly]

The thermodynamic behaviour of N.RGC30 raw and impregnated with [Hmim][BF₄]/[Emim][Gly] ILs in the CO₂ capture process is illustrated in Figure 5.18 for adsorption temperatures of (a) 30, (b) 50 and (c) 80°C.



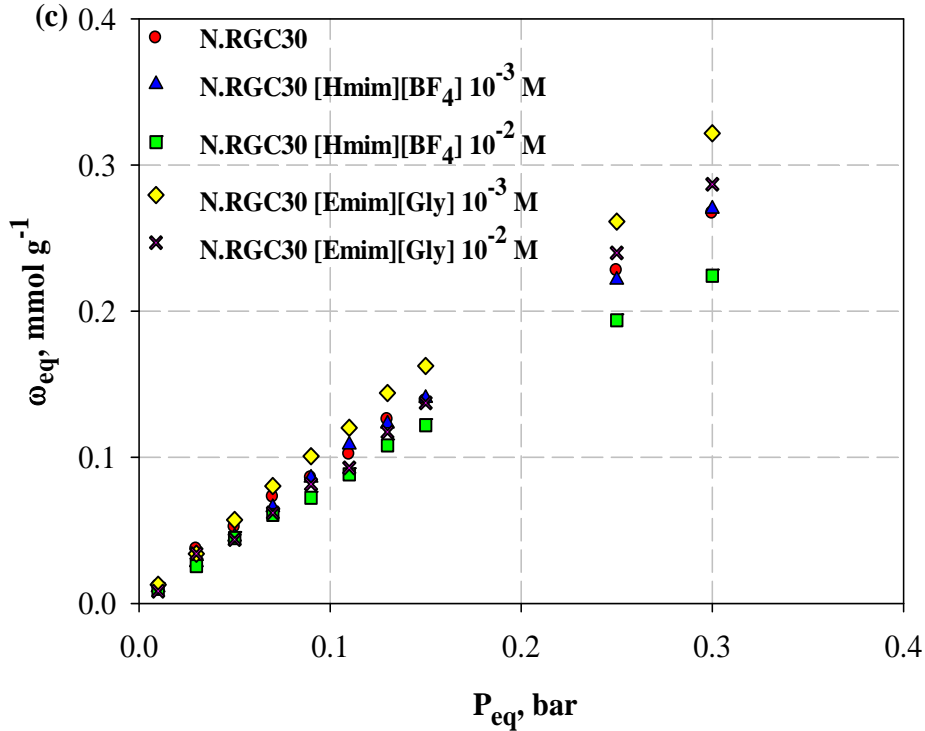


Figure 5.18 CO₂ adsorption isotherms on N.RGC30 raw and impregnated with [Hmim][BF₄]/[Emim][Gly] ILs at C°=5.6×10⁻³ and 2.2×10⁻² M and at a) 30, (b) 50 and (c) 80°C

The analysis of the adsorption isotherms reveals the complex effect of the temperature on CO₂ adsorption performances of the investigated adsorbents and the main aspects can be summarized as follows:

- For an adsorption temperature of 30°C the ω_{eq} ranking is N.RGC30 raw > N.RGC30 [Emim][Gly] 10⁻³ M > N.RGC30 [Emim][Gly] 10⁻² M ≈ N.RGC30 [Hmim][BF₄] 10⁻³ M ≈ N.RGC30 [Hmim][BF₄] 10⁻² M.
- At 50°C N.RGC30 raw and impregnated with [Emim][Gly] under more diluted impregnation conditions exhibit the highest ω_{eq} values and their isotherms practically overlap up to P_{eq} =0.15 bar, while for higher CO₂ concentrations the active phase determines an improvement of the adsorption capacity with respect to the parent sorbent. The other functionalized materials show generally similar adsorption performances except N.RGC30 impregnated with [Hmim][BF₄] at C°=2.2×10⁻² M which is characterized by worse capture capacities for P_{eq} >0.15 bar.
- Finally at 80°C, [Emim][Gly] ionic liquid is effective in ameliorating N.RGC30 capture capacities for all the investigated P_{eq} -range under more diluted impregnation conditions, while ω_{eq} is slightly greater for N.RGC30 [Emim][Gly] 10⁻² M with respect to the raw activated carbon only for CO₂ equilibrium partial pressures greater than those of a typical-flue gas. Moreover, N.RGC30 [Hmim][BF₄] 10⁻² M is again the worst CO₂

adsorbent, while the sample impregnated with the same IL at $C^{\circ}=5.6 \times 10^{-3}$ M is equivalent to the raw material.

In order to shed light on the intertwining among the impregnation conditions, the sorbent properties and their CO₂ capture capacities, Table 5.9 reports a comparison of the main parameters derived from TGA and porosimetric analyses for N.RGC30 raw and impregnated with [Hmim][BF₄]/[Emim][Gly] ILs and their adsorption capacities obtained under typical flue-gas conditions and for operating temperatures of 30, 50 and 80°C.

Table 5.9 Comparison among $\omega_{eq}^{15\%}$ values and the main parameters derived from porosimetric and TGA analyses for N.RGC30 raw and impregnated with [Hmim][BF₄] and [Emim][Gly] ILs

Sample	$\omega_{eq}^{15\%}$ [mmol g ⁻¹]			$(V_{0-raw} - V_{0-impr}) / V_{0-raw}$ %	mmol _{IL-ads} g ⁻¹ _{AC} (TGA)
	T=30°C	T=50°C	T=80°C		
N.RGC30	0.499	0.276	0.139		
N.RGC30 [Hmim][BF ₄] 10 ⁻³ M	0.391	0.246	0.141	6	0.013
N.RGC30 [Hmim][BF ₄] 10 ⁻² M	0.386	0.240	0.122	8	0.051
N.RGC30 [Emim][Gly] 10 ⁻³ M	0.426	0.275	0.163	2	0.027
N.RGC30 [Emim][Gly] 10 ⁻² M	0.381	0.238	0.137	8	0.057

Experimental data highlight that at 30°C pore blocking is the ruling factor in determining a reduction of the impregnated materials adsorption performances with respect to the parent one. In particular, the comparable micropore volume reduction observed for N.RGC30 [Hmim][BF₄] 10⁻² M and 10⁻³ M and N.RGC30 [Emim][Gly] 10⁻² M determines similar $\omega_{eq}^{15\%}$ values for these samples. Conversely, the lower micropore volume reduction determined by [Emim][Gly] at 10⁻³ M (2%) produces a less marked $\omega_{eq}^{15\%}$ decrease with respect to the parent material also for the possible access of CO₂ molecules to the IL active sites, which seems to be hindered in the case of higher IL loading. At 50°C the contribution of [Emim][Gly] active phase in CO₂ capture balances the pore clogging effect only under more diluted impregnation conditions making $\omega_{eq}^{15\%}$ values similar for the functionalized and raw activated carbon; for the other impregnated adsorbents the considerations expressed for an adsorption temperature of 30°C still hold at 50°C, even if differences in capture performances with respect to the parent material reduce for the lower contribution of physisorption of the latter

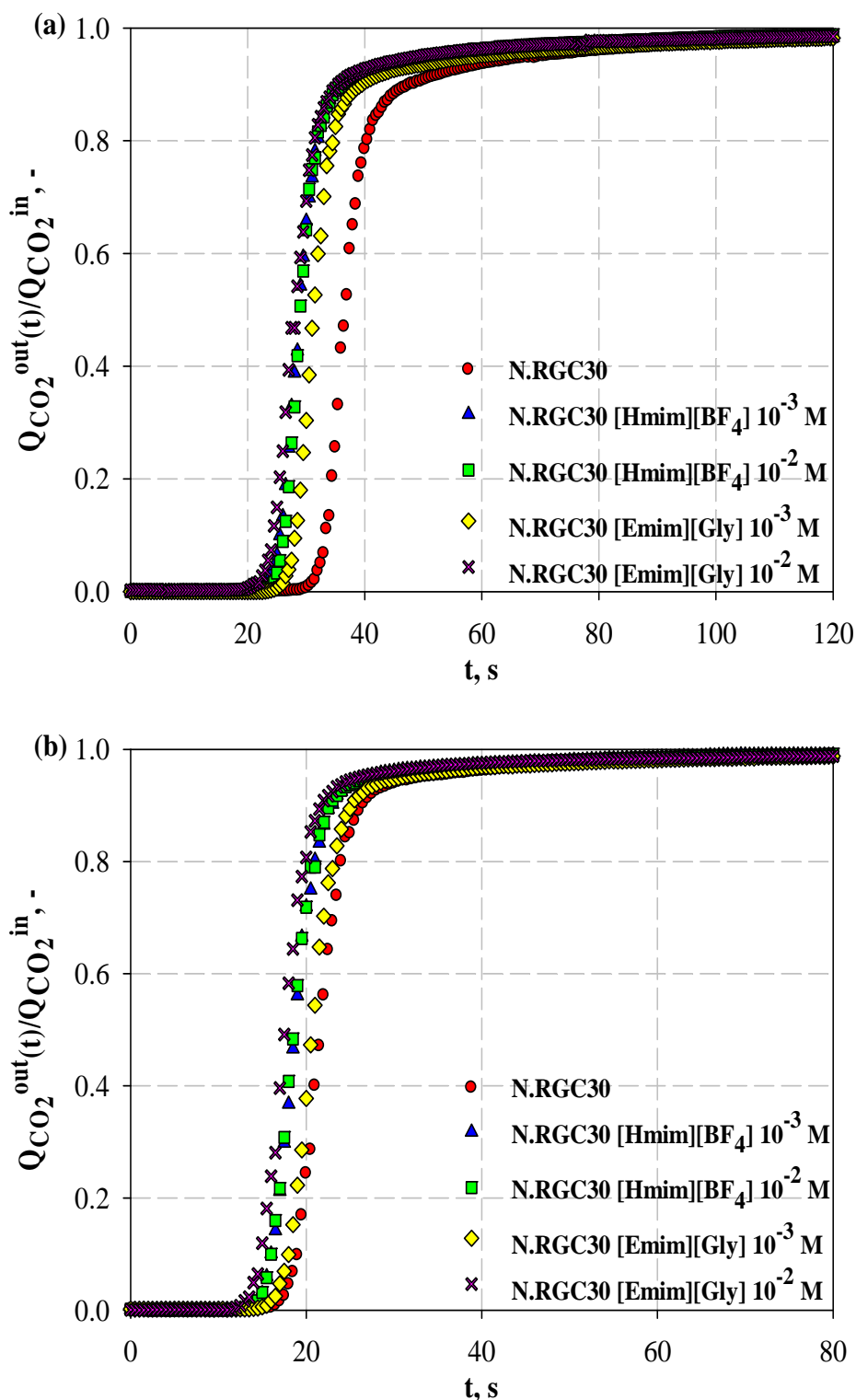
as the temperature rises. Finally, at 80°C the pore blocking is negligible for N.RGC30 [Hmim][BF₄] 10⁻³ M and N.RGC30 [Emim][Gly] 10⁻² M determining equivalent $\omega_{eq}^{15\%}$ values with respect to the parent material, while this effect is still important for N.RGC30 [Hmim][BF₄] 10⁻² M. In the case of N.RGC30 functionalized with [Emim][Gly] at C°=5.6×10⁻³ M, the active phase is able to determine an increase in CO₂ adsorption capacity when compared to the raw substrate ($\omega_{eq}^{15\%}$ is approximately 16% greater) thanks to stronger chemical interactions between acidic CO₂ molecules and basic amine groups and the easier accessibility in the sorbent pores determined by the low IL loading.

The considerations concerning the correlations between sorbent properties and their CO₂ capture capacities under typical flue-gas conditions can be generally extended to the whole P_{eq}-range, even if at 50 and 80°C and for CO₂ equilibrium partial pressures greater than 0.15 bar, the process driving force exerts a further role. For example, at 50°C the contribution in CO₂ capture exerted by [Emim][Gly] under more diluted conditions is prevailing with respect to pore blocking for P_{eq}>0.15 bar (producing an increase in adsorption capacities with respect to N.RGC30 raw), while they balance for lower process driving force; similar arguments are also valid for N.RGC30 [Emim][Gly] 10⁻² M tested at an adsorption temperature of 80°C.

The comparison of the dynamic performances in CO₂ capture process for both raw and ILs-functionalized N.RGC30 sorbents under typical flue-gas conditions (CO₂ 15% by vol.) is reported in Figure 5.19 for operating temperatures of (a) 30, (b) 50 and (c) 80°C. Table 5.10 lists the values of breakpoint time t_b and of the characteristic parameter $\Delta\tau$ derived from the kinetic profiles.

Results evidence, once again, that at higher temperatures the adsorption kinetics is faster for all the investigated sorbents with a monotonic decrease of characteristic breakpoint and saturation times. For example, N.RGC30 [Hmim][BF₄] 10⁻³ M experiences a saturation 3.5-times faster at 80°C with respect to 30°C (t^{*}=165 and 47s at 30 and 80°C), while in the case of N.RGC30 [Emim][Gly] 10⁻³ M, t^{*} is 1.6-times lower for the same temperature increase. Moreover the ranking of t_b values obtained for the different investigated samples is in good agreement with the one derived in terms of CO₂ adsorption capacities (cf. Tables 5.9 and 5.10). The comparison of $\Delta\tau$ data reveals that main kinetic differences can be identified at 30°C for which this parameters is higher for raw N.RGC30 with respect to the impregnated ones indicating slower capture kinetics for this sample. Moreover, N.RGC30 [Emim][Gly] 10⁻³ M displays a slightly higher value of $\Delta\tau$ with respect to the other functionalized materials and this can be ascribed to its lower difference in $\omega_{eq}^{15\%}$ when compared to raw material (cf. Table

5.9). At higher temperatures the intrinsic increase in intraparticle diffusivity and the reduced differences in adsorption capacity contribute in determining similar capture kinetics for all samples. Finally, the way in which the IL is dispersed in the substrate micropores (without affecting remarkably the substrate PSD, cf. Section 5.1) should also contribute in determining different adsorption kinetics for the impregnated samples with respect to the raw material especially at 30°C.



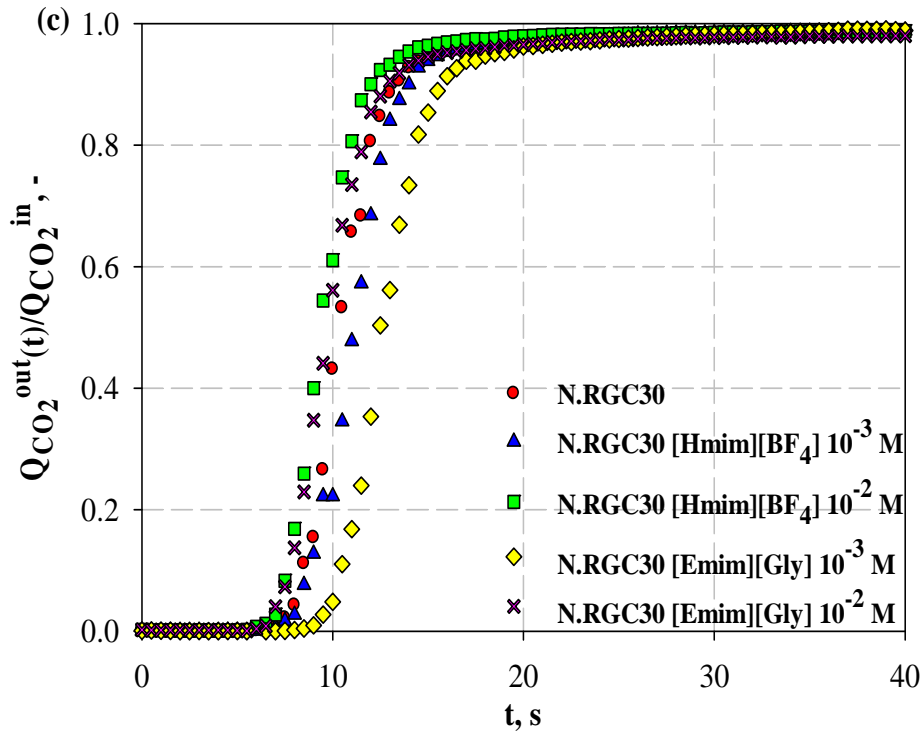


Figure 5.19 Breakthrough curves of CO₂ on N.RGC30 raw and impregnated with [Hmim][BF₄]/[Emim][Gly] for a 15% by vol. CO₂ gaseous stream at (a) 30, (b) 50 and (c) 80°C

Table 5.10 Comparison between $\Delta\tau$ and t_b values obtained from kinetic adsorption tests at 30, 50 and 80°C for N.RGC30 raw and [Hmim][BF₄]/[Emim][Gly]-impregnated; $C_{CO_2}^{inlet}=15\%$ by vol.

Sample	$\Delta\tau$ [s]			t_b [s]		
	T=30°C	T=50°C	T=80°C	T=30°C	T=50°C	T=80°C
N.RGC30	15	8	5	32	18	8
N.RGC30 [Hmim][BF ₄] 10 ⁻³ M	11	8	6	25	15	8
N.RGC30 [Hmim][BF ₄] 10 ⁻² M	11	8	5	25	15	7
N.RGC30 [Emim][Gly] 10 ⁻³ M	13	8	5	27	17	10
N.RGC30 [Emim][Gly] 10 ⁻² M	11	8	6	25	14	7

5.2.4 Intertwining among solids properties and CO₂ capture performances

Table 5.11 schematically summarizes the main results obtained in this work in terms of both sorbents CO₂ capture performances under typical flue-gas conditions (CO₂ 15% by vol.) and main parameters derived from TGA and porosimetric analyses.

As a general comment, it can be observed that for both activated carbons pores blocking induced by the presence of the ILs is the prevailing effect at 30°C which determines a worsening of CO₂ capture performances of each functionalized material with respect to the parent one, due to the main contribution of physisorption for the latter at lower temperatures. Moreover, the impregnation of F600-900 and N.RGC30 with [Hmim][BF₄] IL (a physical solvent for CO₂) appears to be not suitable (at least under the investigated experimental conditions) for flue-gas treatment, because the IL contribution to CO₂ capture does not counterbalance the reduction of the substrate adsorption performances induced by the pores obstruction, also at higher temperatures. On the other hand, the use of more-chemically CO₂ affine [Emim][Gly] IL can be potentially apt to ameliorate the parent carbon sorptive performances towards CO₂ at 80°C, even if at the current stage of the research the obtained adsorption capacities are still too low for a technical applicability of these materials in large scale CO₂ capture processes.

The main aspects derived from a deeper analysis of the effects of the impregnation conditions for each IL on the activated carbons capture performances are discussed in the following.

For [Hmim][BF₄], at 30°C both the impregnation conditions determine a similar percentage reduction of the raw materials $\omega_{eq}^{15\%}$ values (nearly 23%) despite a slightly higher pore volume reduction for F600-900 at $C^{\circ}=2.2 \times 10^{-2}$ M. Moreover, for both F600-900 and N.RGC30 functionalized with [Hmim][BF₄] under more diluted impregnation conditions differences in adsorption capacity with respect to raw substrates reduce as the temperature rises and the pores clogging effect becomes negligible at 80°C. The impregnation of F600-900 with [Hmim][BF₄] at $C^{\circ}=2.2 \times 10^{-2}$ M determines a practically constant percentage reduction of $\omega_{eq}^{15\%}$ values with respect to the raw material as the temperature increases, while in the case of N.RGC30 impregnated with the same IL and adopting the same initial concentration the pore blocking effect on the adsorption performances is less relevant at 80°C. In this context, differences between F600-900 and N.RGC30 impregnated at a higher [Hmim][BF₄] concentration could be related to the combined effects of a larger contribution of wider micropores for N.RGC30 and temperature on a more favourable IL dispersion in the sorbent

pores. This means that for N.RGC30, as the temperature increases, a better distribution of the IL on the substrate pores surface makes the access of CO₂ molecules to the adsorbent active sites easier than in the case of F600-900.

For both F600-900 and N.RGC30 impregnated with [Emim][Gly] at $C^{\circ}=5.6 \times 10^{-3}$ M comparable amounts of IL adsorbed produce similar effects on the adsorption capacity when the temperature increases. In particular, each functionalized material displays similar adsorption capacity with respect to the raw substrate at 50°C, while at 80°C the active phase is able to ameliorate the parent activated carbons capture performances thanks to a good compromise between IL loading and pore accessibility (i.e. a low pore volume reduction). In the case of higher [Emim][Gly] loading, N.RGC30 functionalized material displays similar adsorption capacity with respect to the raw one at 80°C, while F600-900 [Emim][Gly] 10^{-2} M is equivalent to the raw material at 50°C and slightly worse at 80°C. This pattern cannot be directly justified on the basis of the different textural properties of the investigated activated carbons, but should be somehow related to a very complex effect of the temperature on the distribution of this IL into the sorbents pores (hardly explicable with the information currently available).

As an additional remark, it should be considered that it is a really hard task trying to discriminate the contribution to CO₂ capture determined by each IL with respect to the one exerted by the parent material: a better understanding of the effect of the temperature on the IL distribution on the substrate pores will be helpful in this direction.

To the best of our knowledge, similar findings concerning the effects of the impregnation conditions on CO₂ sorptive properties of microporous activated carbons functionalized with ILs have not yet been reported in the literature. Nevertheless, it is worthy of mentioning the work of Plaza et al. (2007) in which an activated carbon (Norit CGP Super) impregnated with different amine-based compounds was employed for CO₂ capture. Authors observed that at room temperature the active phases are not able to exert their peculiar capture properties because of a prevailing pore blocking effect; at higher temperature, this phenomenon is still prevailing but to a less extent because of the reduced contribution of physisorption of the parent material. Finally, they evidenced an increase of the raw material capture performances only for the activated carbon impregnated with diethylentriamine (with the highest nitrogen content) and tested at temperatures greater than 60°C.

Table 5.11 Comparison among $\omega_{eq}^{15\%}$ values and the main parameters derived from porosimetric and TGA analyses for the sorbents investigated in this work

Sample	$\omega_{eq}^{15\%}$ [mmol g ⁻¹]			V_0 [cm ³ g ⁻¹]	V_n [cm ³ g ⁻¹]	$(V_{0-raw} - V_{0-impr}) / V_{0-raw}$ %	mmol _{IL-ads} g ⁻¹ _{AC} (TGA)
	T=30°C	T=50°C	T=80°C				
F600-900	0.575	0.315	0.137	0.41	0.32		
F600-900 [Hmim][BF₄] 10⁻³ M	0.437	0.264	0.139	0.39	n.a.†	4.9	0.015
F600-900 [Hmim][BF₄] 10⁻² M	0.443	0.230	0.101	0.36	n.a.†	12.2	0.052
F600-900 [Emim][Gly] 10⁻³ M	0.502	0.324	0.157	0.39	n.a.†	4.9	0.028
F600-900 [Emim][Gly] 10⁻² M	0.502	0.317	0.125	0.36	n.a.†	12.2	0.057
N.RGC30	0.499	0.276	0.139	0.50	0.32		
N.RGC30 [Hmim][BF₄] 10⁻³ M	0.391	0.246	0.141	0.47	n.a.†	6	0.013
N.RGC30 [Hmim][BF₄] 10⁻² M	0.386	0.240	0.122	0.46	n.a.†	8	0.051
N.RGC30 [Emim][Gly] 10⁻³ M	0.426	0.275	0.163	0.49	n.a.†	2	0.027
N.RGC30 [Emim][Gly] 10⁻² M	0.381	0.238	0.137	0.46	n.a.†	8	0.057

† not available

Table 5.12 reports a comparison of the adsorbents dynamic performances at different temperatures (for a 15% CO₂ gas stream) in terms of $\Delta\tau$ analysis together with the solids main microstructural parameters. It is once again recalled that the different sorbent doses used for adsorption tests (15 and 13 g for F600-900 and N.RGC30 sorbents series, respectively) do not allow to define kinetics differences between N.RGC30 and F600-900 materials on the basis of breakpoint times. Results underline that main differences can be observed at 30°C, where generally higher $\Delta\tau$ values obtained for F600-900 functionalized solids suggest slower kinetics for these sorbents, while differences reduce at higher temperatures to become practically negligible at 80°C. Once again, the occurrence of wider micropores and the greater contribution of mesopores for N.RGC30 adsorbents should determine faster CO₂ diffusion rates with respect to F600-900 impregnated materials. Moreover, the generally lower adsorption capacity observed for N.RGC30 impregnated materials at 30°C (cf. Table 5.11) also contributes in determining faster kinetics. At higher temperatures, intraparticle diffusivity increases (see also Section 5.4.2) and differences in adsorption capacity reduce making the sorbents kinetically equivalent in the capture process at 80°C.

Table 5.12 Comparison between $\Delta\tau$ values obtained from kinetic adsorption tests at 30, 50 and 80°C and the main textural parameters derived for the sorbents investigated in this work; $C_{CO_2}^{inlet}=15\%$ by vol.

Sample	$\Delta\tau$ [s]			Microstructural parameters		
	T=30°C	T=50°C	T=80°C	V_0 [cm ³ g ⁻¹]	V_n [cm ³ g ⁻¹]	V_{meso} [cm ³ g ⁻¹]
F600-900	22	10	5	0.41	0.32	0.17
F600-900 [Hmim][BF₄] 10⁻³ M	16	9	6	0.39	n.a. [†]	0.16
F600-900 [Hmim][BF₄] 10⁻² M	17	9	5	0.36	n.a. [†]	0.16
F600-900 [Emim][Gly] 10⁻³ M	17	10	6	0.39	n.a. [†]	0.16
F600-900 [Emim][Gly] 10⁻² M	17	10	6	0.36	n.a. [†]	0.16
N.RGC30	15	8	5	0.50	0.32	0.65
N.RGC30 [Hmim][BF₄] 10⁻³ M	11	8	6	0.47	n.a. [†]	0.65
N.RGC30 [Hmim][BF₄] 10⁻² M	11	8	5	0.46	n.a. [†]	0.65
N.RGC30 [Emim][Gly] 10⁻³ M	13	8	5	0.49	n.a. [†]	0.65
N.RGC30 [Emim][Gly] 10⁻² M	11	8	6	0.46	n.a. [†]	0.65

[†] not available

5.3 Adsorption/desorption cycles and regeneration experiments for F600-900 raw

In this Section preliminary adsorption/desorption and regeneration experiments carried out on the sorbent which displayed the highest adsorption capacity among all the investigated experimental conditions, namely raw F600-900 tested at 30°C (cf. Table 5.11), are shown.

It is worthy to mention that exploratory CO₂ adsorption/desorption tests over 3 consecutive cycles at 30°C have been performed on [Hmim][BF₄] and [Emim][Gly] functionalized sorbents (not shown here for the sake of brevity) and results showed that the process is reversible for these materials.

In Figure 5.20 CO₂ equilibrium adsorption capacity of raw F600-900 is reported over 10 consecutive adsorption/desorption cycles at 30°C and for a 15% CO₂ gas stream.

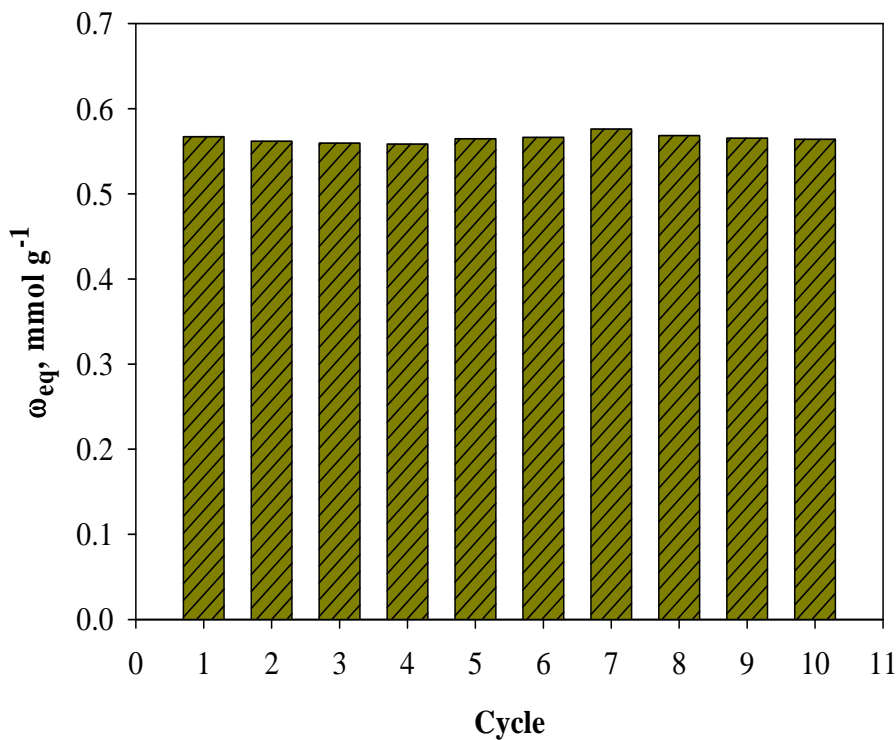
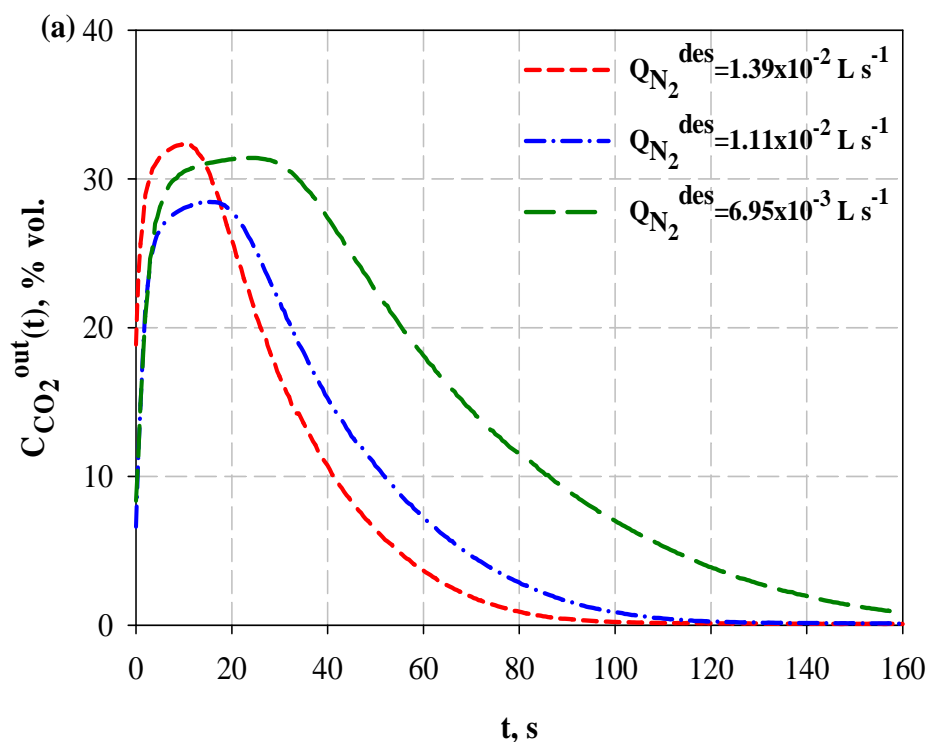


Figure 5.20 Equilibrium adsorption capacity of raw F600-900 obtained over 10 adsorption/desorption cycles at 30°C; $C_{\text{CO}_2}^{\text{inlet}}=15\%$ by vol.

Results indicate that the value of ω_{eq} is practically constant upon the number of cycles and consequently, F600-900 can be completely regenerated (reversible adsorption). This behaviour has been commonly observed in the literature for activated carbons and is ascribed to the establishment of weak interactions between CO₂ molecules and the sorbent surface active sites (physisorption) (Choi et al., 2009; Sayari et al., 2011). In comparison, sorbents such as those calcium oxide-based suffer from a rapid degradation of CO₂ capture capability

during multiple carbonation/calcination cycles caused by pore blocking and adsorbent sintering, thus requiring a continuous make-up of fresh sorbent (Abanades and Alvarez, 2003).

Figure 5.21 reports the time-dependent CO₂ outlet concentration profiles obtained during the regeneration of F600-900 activated carbon (previously saturated with a 15% CO₂ gaseous stream at 30°C) carried out with desorption temperatures of (a) 60 and (b) 100°C and adopting three different N₂ purge flow rate levels ($6.95 \times 10^{-3} \text{ L s}^{-1}$, $1.11 \times 10^{-2} \text{ L s}^{-1}$, $1.39 \times 10^{-2} \text{ L s}^{-1}$, evaluated at T=20°C and P=1 bar).



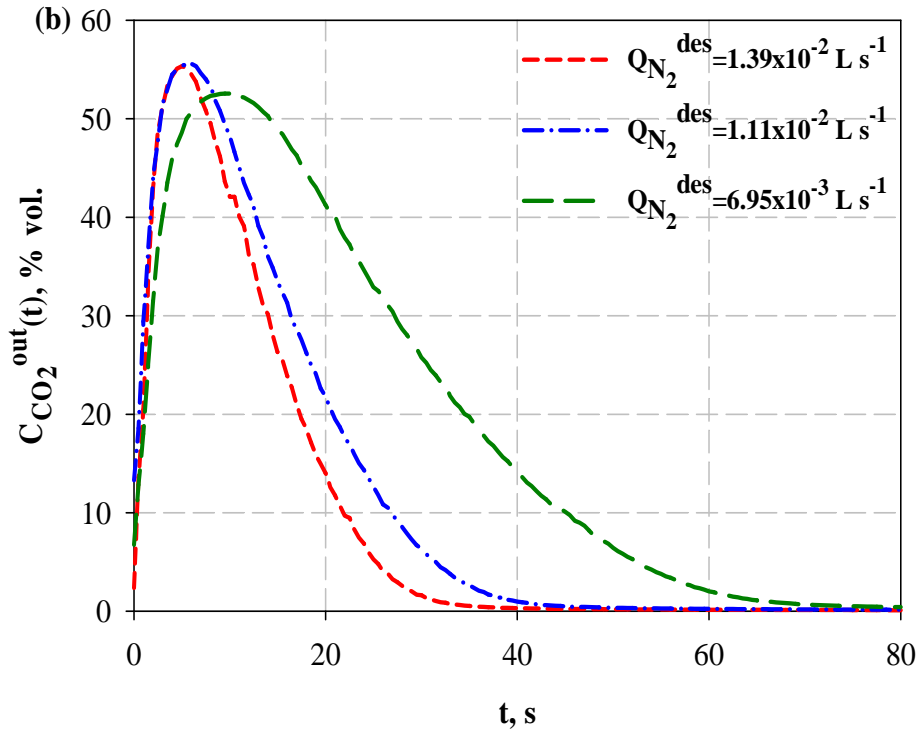


Figure 5.21 CO₂ concentration profiles obtained from regeneration experiments of raw F600-900 as a function of N₂ purge flow rate at (a) 60 and (b) 100°C (adsorption step: $C_{CO_2}^{inlet}=15\%$ by vol., $T=30^\circ C$)

From a qualitative point of view, experimental results evidence that for both regeneration temperatures all the concentration profiles reach a maximum in CO₂ outlet concentration for relatively low desorption times, indicating that most of the adsorbed pollutant is quickly removed from the solid. The regeneration curve becomes narrower as the N₂ flow rate increases, thus testifying a faster desorption process associated to an increase in the gas velocity through the packed-bed (higher stripping rate). However, the concentration profiles show quite long tails indicating that residual CO₂ desorption takes place slowly when the driving force decreases. Finally, for each investigated purge flow rate, an increment in the desorption temperature determines a positive effect on the regeneration kinetic, which can be ascribed to a decrease of CO₂ adsorption capacity (thermodynamic factor) coupled to an increase in the pollutant intraparticle diffusivity (kinetic factor).

The main quantitative parameters obtained from post-processing of regeneration profiles at different N₂ purge flow rates ($Q_{N_2}^{des}$) and desorption temperatures ($T_{60^\circ C}^{des}$ and $T_{100^\circ C}^{des}$), according to the procedure described in Section 4.4.2, are listed in Table 5.13. It is here recalled that $\bar{C}_{CO_2}^i$, $V_{CO_2}^i$ and $V_{N_2}^i$ represent the mean CO₂ concentration in the desorbing flow, the total CO₂ volume desorbed and the purge gas volume fed to the column up to time t_i , respectively (computed for recovery percentages $i=50, 70, 80$ and 90%).

Table 5.13 Main parameters obtained from regeneration experiments of F600-900 raw activated carbon

	$Q_{N_2}^{des}$ [L s ⁻¹]	ω_{eq} [mmol g ⁻¹]	ω_{des} [mmol g ⁻¹]	t_{50} [s]	t_{70} [s]	t_{80} [s]	t_{90} [s]	$V_{N_2}^{50}$ [L]	$V_{N_2}^{70}$ [L]	$V_{N_2}^{80}$ [L]	$V_{N_2}^{90}$ [L]	$\bar{C}_{CO_2}^{50}$ [% vol.]	$\bar{C}_{CO_2}^{70}$ [% vol.]	$\bar{C}_{CO_2}^{80}$ [% vol.]	$\bar{C}_{CO_2}^{90}$ [% vol.]
$T_{60^\circ C}^{des}$	6.95x10 ⁻³	0.559	0.569	33	50	62	80	0.229	0.348	0.431	0.556	29.5	28.6	27.0	24.5
	1.11x10 ⁻²	0.565	0.561	25	37	46	61	0.278	0.411	0.511	0.677	25.4	24.4	22.8	19.9
	1.39x10 ⁻²	0.566	0.554	17	25	32	44	0.236	0.348	0.445	0.612	30.4	28.6	26.8	23.1
$T_{100^\circ C}^{des}$	6.95x10 ⁻³	0.567	0.557	15	22	28	37	0.104	0.153	0.195	0.257	47.0	46.4	43.7	40
	1.11x10 ⁻²	0.562	0.559	9	13	16	21	0.100	0.144	0.178	0.233	49.4	48.2	46.2	42.3
	1.39x10 ⁻²	0.560	0.555	7	11	13	17	0.097	0.153	0.181	0.236	47.7	47.0	45.7	42.2

It is worthy to observe that the comparison between ω_{eq} and ω_{des} values, obtained from the integration of the adsorption and desorption kinetic profiles respectively, allows the verification of the CO₂ mass balance for each test. Results confirm the positive effects on the desorption kinetics induced by an increase of both $Q_{N_2}^{des}$ and desorption temperature. As a matter of fact, at a fixed desorption temperature, the time required to obtain a defined CO₂ recovery percentage monotonically decreases with the N₂ purge flow rate: for example, at both temperatures, t_{50} and t_{90} approximately double when $Q_{N_2}^{des}$ decreases from 1.39×10^{-2} L s⁻¹ to 6.95×10^{-3} L s⁻¹. Moreover, a similar trend for t_i is observed when the desorption temperature increases: for $Q_{N_2}^{des} = 1.39 \times 10^{-2}$ L s⁻¹, t_{50} and t_{90} at $T_{100^\circ C}^{des}$ are nearly 0.4-times the corresponding values determined at $T_{60^\circ C}^{des}$. The results obtained in terms of $\bar{C}_{CO_2}^i$ reveal even more interesting features. For each $Q_{N_2}^{des}$ and for each temperature, when the desired CO₂ recovery level is increased the mean CO₂ concentration in the desorbing stream decreases. In fact, as the recovery percentage increases the time required for desorption is higher, the desorption rate decreases with time due to a lowering in the driving force and, consequently, a greater purge volume is required to remove residual adsorbed CO₂, determining a dilution effect. Differently, for each temperature and for each fixed CO₂ recovery level, $\bar{C}_{CO_2}^i$ does not substantially vary when comparing the values obtained at 1.39×10^{-2} L s⁻¹ and 6.95×10^{-3} L s⁻¹. In fact, from eq. (4.5) (Section 4.4.2), at fixed regeneration level $V_{CO_2}^i$ is constant but $V_{N_2}^i$ depends on both desorption time and purge flow rate ($Q_{N_2}^{des} t_i$, in eq. (4.5)): this product is comparable at the highest and lowest purge flow rate investigated determining equivalent concentration levels. From data reported in Table 5.13, it can be also highlighted that for $T_{60^\circ C}^{des}$ a recovery level of 90% adopting the lowest N₂ flow rate allows to obtain a desorbing gas with $\bar{C}_{CO_2}^i \approx 25\%$, while the mean CO₂ concentration only slightly increases for a 50% solid regeneration ($\bar{C}_{CO_2}^i \approx 30\%$), but this would eventually produce a significant reduction in the sorbent utilization time, if a subsequent adsorption cycle has to be performed. A regeneration temperature of 100°C appears to be the best operating condition to obtain higher $\bar{C}_{CO_2}^i$ values: a more concentrated gas is obtained by recovering 90% of the adsorbed CO₂ with respect to $T_{60^\circ C}^{des}$ at the same regeneration level and for $Q_{N_2}^{des} = 6.95 \times 10^{-3}$ L s⁻¹ and with a halved desorption time ($t_{90} = 80$ and 37 s for $T_{60^\circ C}^{des}$ and $T_{100^\circ C}^{des}$, respectively). Finally, regeneration

levels of 70% and 80%, obtained at 100°C and for $Q_{N_2}^{des} = 1.11 \times 10^{-2} \text{ L s}^{-1}$, can be identified as the optimal solutions among those investigated, as a compromise between the amount of CO₂ recovered, its concentration in the desorbed gas (46-48% by vol.) and time required to perform that recovery.

5.4 Adsorption thermodynamics and kinetics modelling

In this Section, modelling analysis (using equations described in Chapter 3) of both adsorption isotherms and breakthrough curves, experimentally determined for all the solids investigated in this work, is presented.

5.4.1 Thermodynamic aspects

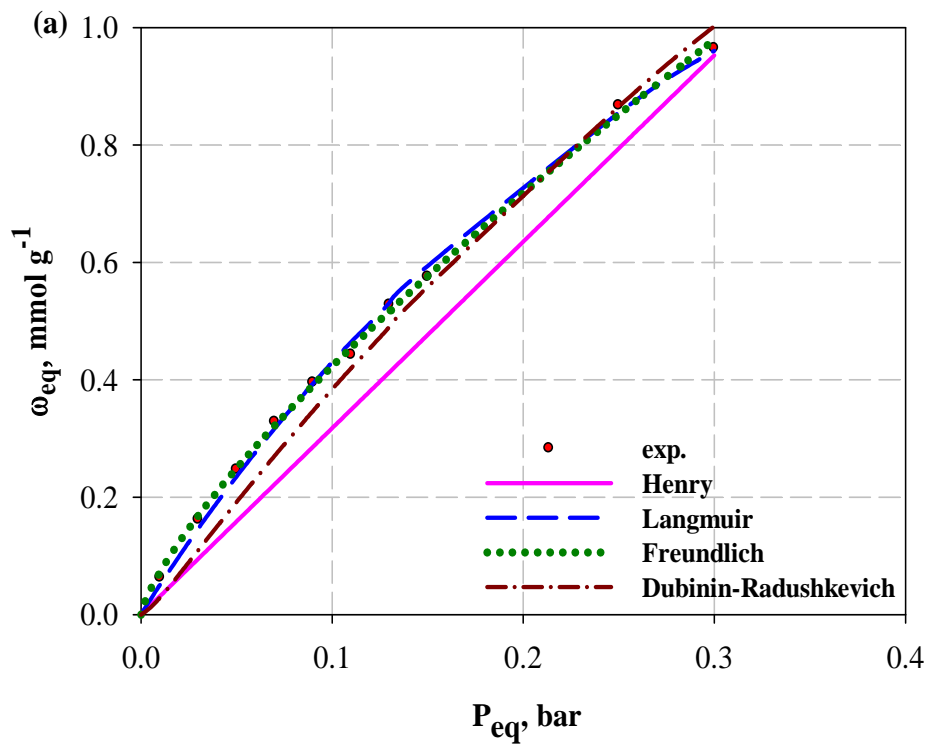
Tables 5.14 and 5.15 list the main parameters obtained from the application of Henry/Langmuir/Freundlich/Dubinin-Radushkevich models to the adsorption isotherms obtained at 30, 50 and 80°C for F600-900 and N.RGC30 both raw and ILs-functionalized.

It is highlighted that: i) for the Langmuir model a simultaneous fitting of the adsorption isotherms at different temperatures was performed by imposing a unique ω_{\max} value (temperature-independent) according to the recommendation provided in Ruthven (1984); ii) for Dubinin-Radushkevich model, the characteristic energy E was obtained by simultaneously fitting equilibrium data at different temperatures according to eq. (3.5) (cf. Chapter 3), and for each solid the micropore volume determined from N_2 porosimetric data at -196°C (cf. Chapter 5) was imposed as a constant parameter. Moreover for DR model, the molar volume of the liquid adsorbate and the pseudo-vapor pressure were computed according to the expressions reported in Do (1998) and Saha et al. (2011).

As a general consideration, it can be observed that the Henry model provides the poorest quality of data fitting for all sorbents as testified by the lowest values of the determination coefficient R^2 above all at 30°C; at 80°C the model provides a better fitting of adsorption isotherms due to a more linear trend of adsorption data (cf. also Figure 5.22). Similarly, the DR model is not adequate to interpret satisfactorily adsorption isotherms above all at higher temperatures and this is possibly related to the absence of adsorption data at high pressures for a proper fitting of the characteristic curve (eq. (3.5)). Freundlich and Langmuir models determine the best fitting of equilibrium data for all the investigated materials and experimental conditions as testified by the highest R^2 values (practically unitary for both). In particular, for each sorbent K_L and K_F values decrease with temperature, due to the exothermic nature of the adsorption process (Ruthven, 1984; Do, 1998). It is interesting to observe that in all the cases, the values of the Freundlich heterogeneity parameter $1/n$ do not differ too much from unity, which clearly indicates that the sorbent surfaces are practically energetically homogeneous in the CO_2 capture process, also in the case of functionalized sorbents (*vide infra*) (Do, 1998).

Finally, in the case of Freundlich model it is possible to observe a general better agreement between the ranking derived in terms of the affinity parameter (K_F) and those observed for the adsorption capacities of the investigated sorbents with respect to a comparison on the basis of the Langmuir constant K_L . For instance, when comparing the values of this parameter for the raw activated carbons, we obtain $K_F=2.45$ and 2.03 at 30°C and 0.80 and 0.81 at 80°C for F600-900 and N.RGC30 respectively, which agrees with the general trend of the adsorption isotherms with temperature described in Section 5.2.1 (higher CO_2 capture capacities for F600-900 at 30°C while equivalent adsorption performances at 80°C).

As an example, Figure 5.22 reports the comparison between experimental adsorption isotherms and thermodynamic models predictions for F600-900 raw at (a) 30, (b) 50 and (c) 80°C .



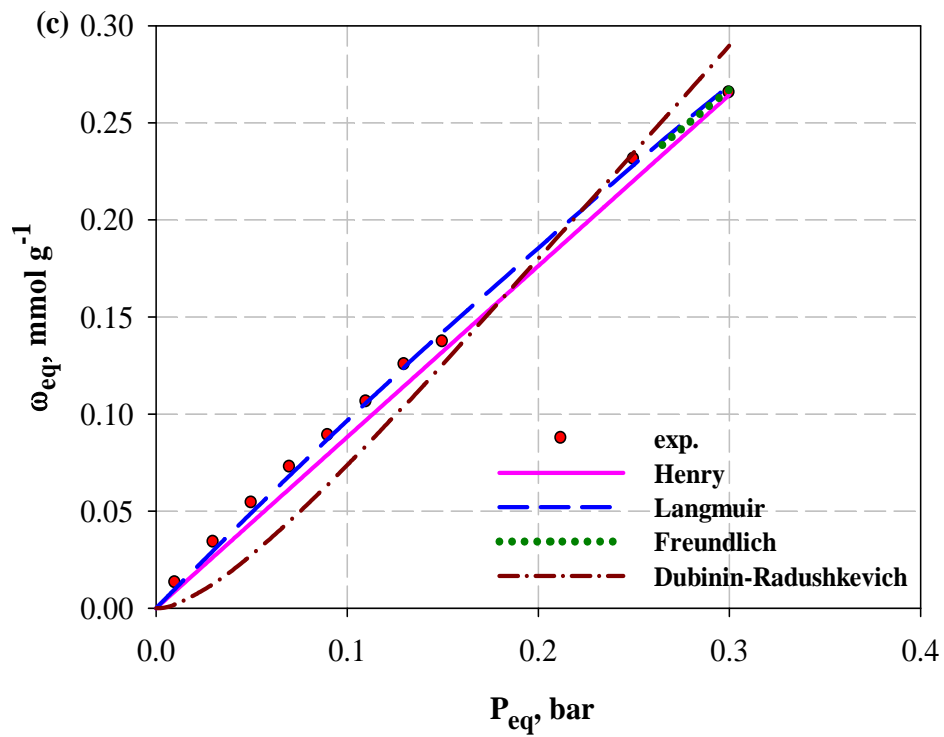
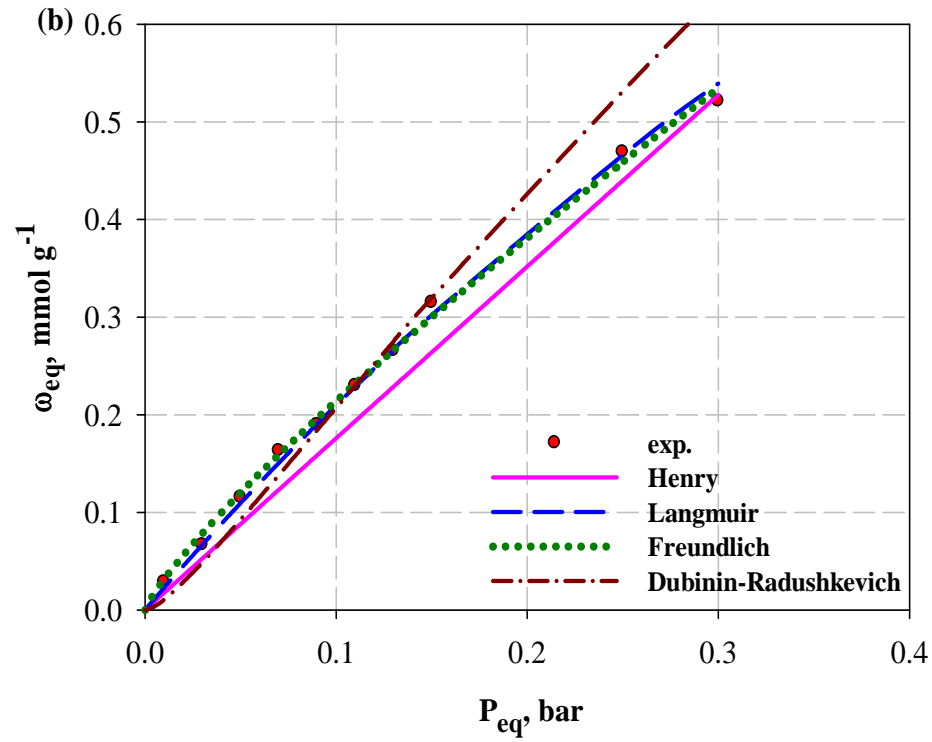


Figure 5.22 Comparison between experimental adsorption isotherms (symbols) and Henry, Langmuir, Freundlich and Dubinin-Radushkevich models (lines) for F600-900 raw at (a) 30, (b) 50 and (c) 80°C

Table 5.14 Main parameters of Henry, Langmuir, Freundlich and Dubinin-Radushkevich models for CO₂ adsorption onto F600-900 raw and impregnated with [Hmim][BF₄]/[Emim][Gly] ILs at 30, 50 and 80°C

			F600-900	F600-900 [Hmim][BF ₄] 10 ⁻³ M	F600-900 [Hmim][BF ₄] 10 ⁻² M	F600-900 [Emim][Gly] 10 ⁻³ M	F600-900 [Emim][Gly] 10 ⁻² M
Henry	K _H [mmol g ⁻¹ bar ⁻¹]	T=30°C	3.18	2.38	2.35	2.95	2.87
		T=50°C	1.76	1.63	1.38	1.91	1.89
		T=80°C	0.88	0.92	0.66	1.01	0.83
	R ²	T=30°C	0.922	0.969	0.970	0.966	0.951
		T=50°C	0.965	0.989	0.982	0.977	0.983
		T=80°C	0.990	0.994	0.994	0.999	0.996
Langmuir	K _L [bar ⁻¹]	T=30°C	2.07	1.31	1.8	1.28	1.49
		T=50°C	0.91	0.79	0.87	0.75	0.84
		T=80°C	0.40	0.41	0.37	0.34	0.32
	ω _{max} [mmol g ⁻¹]		2.51	2.54	2.01	3.19	2.81
	R ²	T=30°C	0.998	0.998	0.999	0.998	0.999
		T=50°C	0.997	0.999	0.999	0.999	0.999
T=80°C		0.998	0.997	0.999	0.999	0.998	
Freundlich	K _F [mmol g ⁻¹ bar ^{-1/n}]	T=30°C	2.45	1.95	1.85	2.45	2.32
		T=50°C	1.46	1.46	1.20	1.62	1.65
		T=80°C	0.80	0.88	0.61	1.00	0.78
	1/n	T=30°C	0.76	0.82	0.78	0.83	0.81
		T=50°C	0.83	0.90	0.88	0.86	0.88
		T=80°C	0.91	0.95	0.93	0.99	0.95
	R ²	T=30°C	0.999	0.999	0.998	0.996	0.999
		T=50°C	0.999	0.999	0.999	0.999	0.999
		T=80°C	0.999	0.997	0.999	0.997	0.998
Dubinin Radushkevich	ω _{max} [mmol g ⁻¹]	T=30°C	8.85	8.42	7.77	8.42	7.77
		T=50°C	8.42	8.01	7.39	8.01	7.39
		T=80°C	7.81	7.43	6.86	7.43	6.86
	E [kJ mol ⁻¹]		9.36	9.05	9.09	9.36	9.41
	R ²	T=30°C	0.978	0.976	0.972	0.987	0.990
		T=50°C	0.975	0.967	0.977	0.975	0.980
		T=80°C	0.975	0.686	0.898	0.895	0.945

Table 5.15 Main parameters of Henry, Langmuir, Freundlich and Dubinin-Radushkevich models for CO₂ adsorption onto N.RGC30 raw and impregnated with [Hmim][BF₄]/[Emim][Gly] ILs at 30, 50 and 80°C

			N.RGC30	N.RGC30 [Hmim][BF ₄] 10 ⁻³ M	N.RGC30 [Hmim][BF ₄] 10 ⁻² M	N.RGC30 [Emim][Gly] 10 ⁻³ M	N.RGC30 [Emim][Gly] 10 ⁻² M
Henry	K _H [mmol g ⁻¹ bar ⁻¹]	T=30°C	2.64	2.20	2.12	2.48	2.18
		T=50°C	1.68	1.56	1.48	1.78	1.57
		T=80°C	0.88	0.89	0.75	1.05	0.95
	R ²	T=30°C	0.921	0.964	0.944	0.967	0.970
		T=50°C	0.981	0.995	0.991	0.996	0.998
		T=80°C	0.990	0.997	0.992	0.998	0.996
Langmuir	K _L [bar ⁻¹]	T=30°C	2.04	1.20	1.60	1.06	0.89
		T=50°C	1.04	0.74	0.94	0.67	0.57
		T=80°C	0.48	0.39	0.43	0.37	0.32
	ω _{max} [mmol g ⁻¹]		2.10	2.52	1.98	3.14	3.15
	R ²	T=30°C	0.999	0.999	0.999	0.999	0.997
		T=50°C	0.999	0.999	0.999	0.997	0.995
T=80°C		0.998	0.999	0.999	0.999	0.992	
Freundlich	K _F [mmol g ⁻¹ bar ^{-1/n}]	T=30°C	2.03	1.82	1.68	2.07	1.83
		T=50°C	1.45	1.44	1.33	1.70	1.53
		T=80°C	0.81	0.84	0.68	1.01	1.03
	1/n	T=30°C	0.76	0.83	0.79	0.83	0.84
		T=50°C	0.87	0.93	0.91	0.95	0.98
		T=80°C	0.92	0.95	0.91	0.96	0.98
	R ²	T=30°C	0.998	0.999	0.999	0.999	0.998
		T=50°C	0.999	0.999	0.999	0.999	0.998
		T=80°C	0.999	0.999	0.999	0.999	0.992
Dubinin Radushkevich	ω _{max} [mmol g ⁻¹]	T=30°C	10.78	10.15	9.93	10.58	9.93
		T=50°C	10.27	9.65	9.45	10.06	9.45
		T=80°C	9.53	8.96	8.76	9.34	8.76
	E [kJ mol ⁻¹]		8.84	8.67	8.64	8.80	8.67
	R ²	T=30°C	0.931	0.917	0.910	0.925	0.918
		T=50°C	0.928	0.942	0.933	0.955	0.955
		T=80°C	0.730	0.501	0.616	0.508	0.534

The energetic aspects of the adsorption phenomena for the investigated systems were evaluated by computing the isosteric heat of adsorption q_{st} as a function of the specific loading ω by means of the Clausius-Clapeyron equation applied to experimental adsorption data at different temperatures (cf. eq. (3.8) in Section 3.1). The q_{st} vs. ω trends are reported in Figure 5.23 for both (a) F600-900 based and (b) N.RGC30 materials.

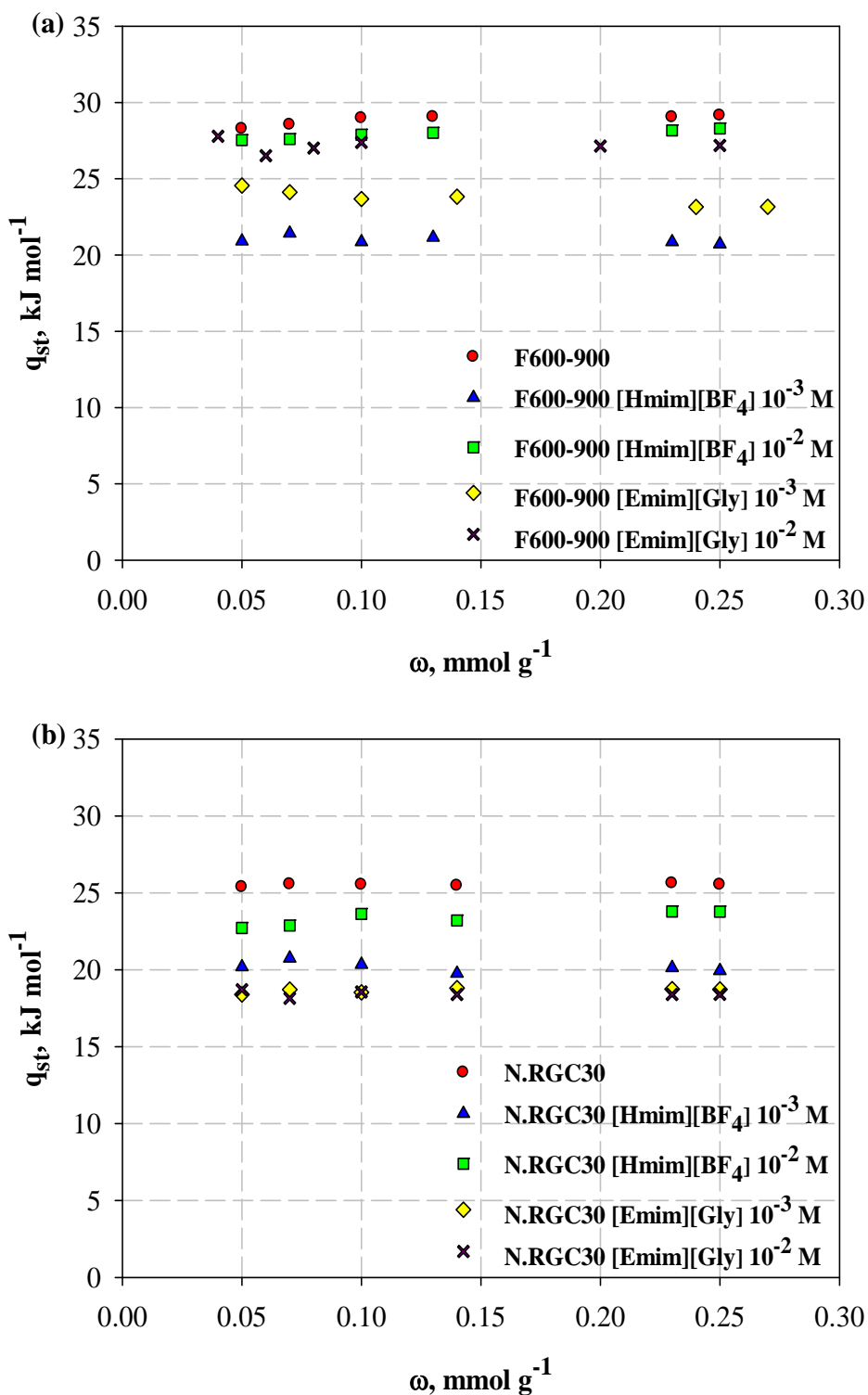


Figure 5.23 Isosteric heat of adsorption as a function of the specific loading for (a) F600-900 and (b) N.RGC30 adsorbents both raw and functionalized with [Hmim][BF₄]/[Emim][Gly] ILs

As it can be observed, the isosteric heat of adsorption is practically constant with loading for all the investigated adsorbents, indicating that the surfaces are energetically homogeneous towards CO₂ capture (Chakraborty et al., 2006), in agreement with the observations derived from thermodynamic modelling analysis. For impregnated materials, the low amounts of active phase charged do not appreciably modify the overall surface energetic homogeneity of the parent substrate thus determining a constant q_{st} value with loading. In this context, it is hard at the current stage of the research to understand the interplay of the contributions of the substrate active sites and the ones belonging to the ionic liquid to CO₂ capture, and consequently to explain the trends observed for the functionalized materials in terms of interaction energies. On the other hand, the mean values of the isosteric heat of adsorption obtained for the raw activated carbons are 28.8 and 25.5 kJ mol⁻¹ for F600-900 and N.RGC30 respectively: this confirms that the presence of a narrower micropore size distribution with a prevailing contribution of very small pore diameters (<10 Å) observed for F600-900 produces stronger interactions with CO₂ molecules with respect to N.RGC30 and consequently higher adsorption performances above all at lower temperatures (cf. Section 5.2.1).

5.4.2 Kinetic aspects

The main kinetic parameters determined from the modelling analysis of breakthrough curves (according to the theoretical frameworks described in Section 3.2) obtained at different operating temperatures and for a 15% CO₂ gas stream are reported in Tables 5.16 and 5.17 for F600-900 and N.RGC30 sorbents series, respectively. It is here recalled that mass and momentum balance equations were numerically solved with Aspen Adsim™ software adopting a linear driving force approximation (LDF) for the mass transfer rate; moreover the only fitting parameter of the model was the micropore diffusivity D_{micro} , whereas the external and macropore (Knudsen) mass transfer coefficients were calculated from gas/solids properties (cf. Section 3.2). Figure 5.24 reports, as an example, the comparison of the experimental and theoretical breakthrough curves obtained for raw F600-900 for a typical flue-gas composition and at (a) 30, (b) 50 and (c) 80°C.

As a general consideration, it is highlighted that the Freundlich thermodynamic model was adopted as equilibrium isotherm in the rate of adsorption equation (3.13) (cf. Section 3.2) because it supplied slightly better numerical solutions with respect to the Langmuir isotherm. Noteworthy, the computed fixed-bed Péclet number was higher than 100 in all cases, thus it was possible to consider a plug-flow for all the investigated systems (Inglezakis and Pouloupoulos, 2006); in addition, the pressure drops across the fixed bed, calculated from Ergun's equation (3.14), were practically negligible (order of magnitude 10^{-3} bar).

The general features inferable from a comparison among film, macropore and micropore diffusion resistances are summarized in the following.

- Micropore diffusion mechanism represents the rate-determining step of the adsorption process in almost all the investigated systems. As the temperature increases, differences between micropore and macropore diffusion resistances tend to reduce, and in any case the CO₂ transport through the external fluid film is very fast (negligible film-diffusion resistance). D_{micro} is generally 2 or 3 orders of magnitude lower than D_{macro} at 30°C, and while the former has a strong dependence on temperature the latter only slightly increases from 30 to 80°C.
- When comparing each raw activated carbon with the corresponding functionalized materials, it can be observed that micropore diffusion resistance is higher for the former and differences diminish with temperature to become practically negligible at 80°C. This behaviour should be once again imputed to the already described trends in adsorption capacity and micropore diffusivity together with the possible influence of

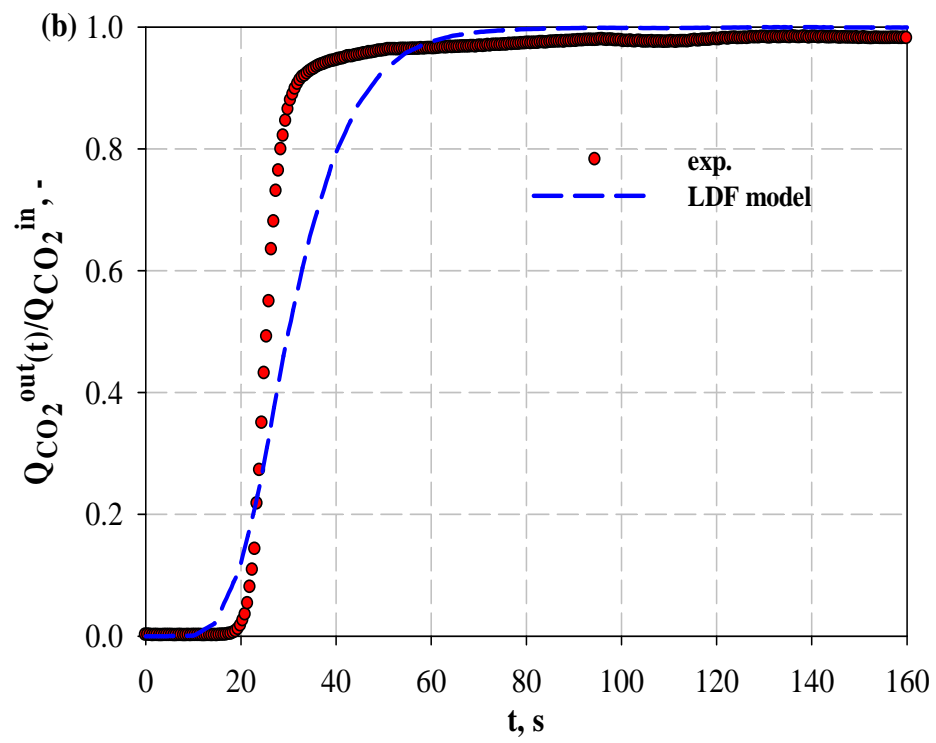
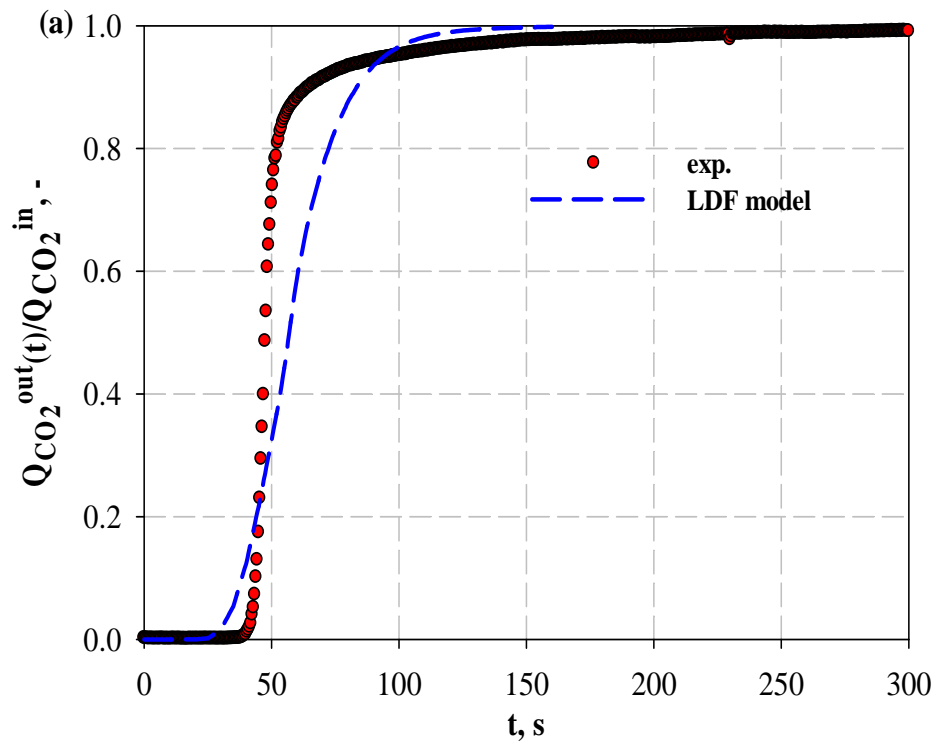
the temperature on the IL distribution inside the sorbent pores in the case of impregnated adsorbents (cf. also Sections 5.2.2 and 5.2.3). Finally, for N.RGC30 sorbents, the diffusion resistances are generally lower than those observed for F600-900 materials and differences reduce with temperature: this testifies again the important role exerted by both the occurrence of wider micropores and the greater contribution of mesopores for N.RGC30 adsorbents with respect to F600-900 ones in determining faster kinetics above all at lower temperatures. The observations here provided confirm the results discussed in terms of $\Delta\tau$ analysis in the previous Sections.

Table 5.16 Main kinetic parameters derived from mathematical modelling of breakthrough curves for CO₂ adsorption onto F600-900 raw and impregnated with [Hmim][BF₄]/[Emim][Gly] ILs at 30, 50 and 80°C; C_{CO₂}^{inlet}=15% by vol.

			F600-900	F600-900 [Hmim][BF ₄] 10 ⁻³ M	F600-900 [Hmim][BF ₄] 10 ⁻² M	F600-900 [Emim][Gly] 10 ⁻³ M	F600-900 [Emim][Gly] 10 ⁻² M
Film diffusion	$\frac{d_p}{6k_{ext}}$ [s]	T=30°C	1.37x10 ⁻³	1.37x10 ⁻³	1.37x10 ⁻³	1.37x10 ⁻³	1.37x10 ⁻³
		T=50°C	1.23x10 ⁻³	1.23x10 ⁻³	1.23x10 ⁻³	1.23x10 ⁻³	1.23x10 ⁻³
		T=80°C	1.08x10 ⁻³	1.08x10 ⁻³	1.08x10 ⁻³	1.08x10 ⁻³	1.08x10 ⁻³
Macropore diffusion	$\frac{d_p^2}{60\varepsilon_p D_{macro}}$ [s]	T=30°C	0.15	0.16	0.16	0.16	0.16
		T=50°C	0.15	0.15	0.15	0.15	0.15
		T=80°C	0.14	0.14	0.15	0.14	0.15
	D _{macro} [m ² s ⁻¹]	T=30°C	1.13x10 ⁻⁷	1.13x10 ⁻⁷	1.13x10 ⁻⁷	1.13x10 ⁻⁷	1.13x10 ⁻⁷
		T=50°C	1.17x10 ⁻⁷	1.17x10 ⁻⁷	1.17x10 ⁻⁷	1.17x10 ⁻⁷	1.17x10 ⁻⁷
		T=80°C	1.22x10 ⁻⁷	1.22x10 ⁻⁷	1.22x10 ⁻⁷	1.22x10 ⁻⁷	1.22x10 ⁻⁷
Micropore diffusion	$\frac{d_p^2}{60HD_{micro}}$ [s]	T=30°C	3.82	1.10	1.21	1.22	1.72
		T=50°C	1.08	0.24	0.60	1.20	0.65
		T=80°C	0.34	0.22	0.31	0.05	0.40
	D _{micro} [m ² s ⁻¹]	T=30°C	1.60x10 ⁻¹⁰	8.52x10 ⁻¹⁰	7.32x10 ⁻¹⁰	6.19x10 ⁻¹⁰	4.24x10 ⁻¹⁰
		T=50°C	1.15x10 ⁻⁹	6.26x10 ⁻⁹	2.75x10 ⁻⁹	9.76x10 ⁻¹⁰	1.79x10 ⁻⁹
		T=80°C	7.13x10 ⁻⁹	1.15x10 ⁻⁸	1.12x10 ⁻⁸	5.26x10 ⁻⁸	7.06x10 ⁻⁹

Table 5.17 Main kinetic parameters derived from mathematical modelling of breakthrough curves for CO₂ adsorption onto N.RGC30 raw and impregnated with [Hmim][BF₄]/[Emim][Gly] ILs at 30, 50 and 80°C; C_{CO₂}^{inlet}=15% by vol.

			N.RGC30	N.RGC30 [Hmim][BF ₄] 10 ⁻³ M	N.RGC30 [Hmim][BF ₄] 10 ⁻² M	N.RGC30 [Emim][Gly] 10 ⁻³ M	N.RGC30 [Emim][Gly] 10 ⁻² M
Film diffusion	$\frac{d_p}{6k_{ext}}$ [s]	T=30°C	1.60x10 ⁻³	1.60x10 ⁻³	1.60x10 ⁻³	1.60x10 ⁻³	1.60x10 ⁻³
		T=50°C	1.44x10 ⁻³	1.44x10 ⁻³	1.44x10 ⁻³	1.44x10 ⁻³	1.44x10 ⁻³
		T=80°C	1.26x10 ⁻³	1.26x10 ⁻³	1.26x10 ⁻³	1.26x10 ⁻³	1.26x10 ⁻³
Macropore diffusion	$\frac{d_p^2}{60\varepsilon_p D_{macro}}$ [s]	T=30°C	0.09	0.10	0.10	0.09	0.10
		T=50°C	0.09	0.10	0.10	0.09	0.10
		T=80°C	0.09	0.10	0.10	0.10	0.10
	D _{macro} [m ² s ⁻¹]	T=30°C	2.10x10 ⁻⁷	2.10x10 ⁻⁷	2.10x10 ⁻⁷	2.10x10 ⁻⁷	2.10x10 ⁻⁷
		T=50°C	2.11x10 ⁻⁷	2.11x10 ⁻⁷	2.11x10 ⁻⁷	2.11x10 ⁻⁷	2.11x10 ⁻⁷
		T=80°C	2.12x10 ⁻⁷	2.12x10 ⁻⁷	2.12x10 ⁻⁷	2.12x10 ⁻⁷	2.12x10 ⁻⁷
Micropore diffusion	$\frac{d_p^2}{60HD_{micro}}$ [s]	T=30°C	1.66	0.54	0.51	0.63	0.61
		T=50°C	0.30	0.15	0.15	0.14	0.18
		T=80°C	0.15	0.15	0.08	0.07	0.08
	D _{micro} [m ² s ⁻¹]	T=30°C	5.89x10 ⁻¹⁰	9.34x10 ⁻¹⁰	9.58x10 ⁻¹⁰	6.95x10 ⁻¹⁰	8.33x10 ⁻¹⁰
		T=50°C	2.41x10 ⁻⁹	5.89x10 ⁻⁹	5.57x10 ⁻⁹	5.23x10 ⁻⁹	4.46x10 ⁻⁹
		T=80°C	9.57x10 ⁻⁹	2.15x10 ⁻⁸	2.02x10 ⁻⁸	1.75x10 ⁻⁸	2.03x10 ⁻⁸



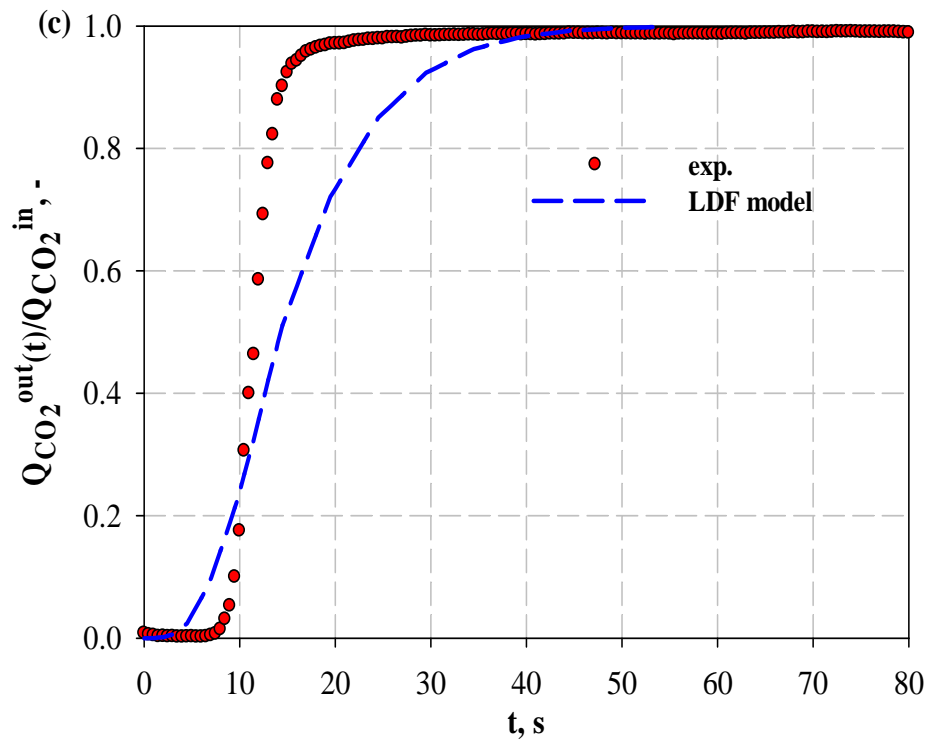


Figure 5.24 Comparison between experimental (symbols) and theoretical (lines) breakthrough curves obtained for F600-900 raw at (a) 30, (b) 50 and (c) 80°C; $C^{inlet}CO_2=15\%$ by vol.

CHAPTER 6

CONCLUSIONS AND FUTURE PERSPECTIVES

The need of developing high performance and cost-effective post-combustion purification systems for CO₂ capture has recently stimulated the research of new adsorbents materials with tailored microstructural and chemical properties. Contextually, the use of supported ionic liquid phase materials (SILP) is a very attractive but limitedly explored investigation area. In this PhD project the effect of confining ionic liquids (ILs) into activated carbons characterized by different porosimetric structures on their CO₂ capture performances under typical flue-gas conditions has been investigated. The obtained results have provided a deeper understanding in this field with respect to the available scientific literature.

CO₂ adsorption tests have been carried in model flue-gas streams onto two commercial activated carbons, namely Filtrasorb 400 and Nuchar RGC30, both raw and functionalized with either 1-hexyl-3-methylimidazolium tetrafluoroborate [Hmim][BF₄] or 1-ethyl-3-methylimidazolium glycine [Emim][Gly] ILs adopting different impregnation conditions (5.6×10^{-3} and 2.2×10^{-2} M).

Results obtained for raw activated carbons have confirmed, in agreement with previously literature findings, that the presence of a narrower micropore size distribution with a prevailing contribution of very small pore diameters ($<10 \text{ \AA}$) observed for Filtrasorb 400 is a key factor in determining higher CO₂ capture capacities above all at low temperature (30°C); on the other hand, the sorbents are equivalent in the purification process at 80°C because of the reduced contribution of physisorption at higher temperatures, as expected in exothermal processes. These experimental evidences have been also corroborated by the higher value of the isosteric heat derived for Filtrasorb 400 solid, testifying stronger interactions with CO₂ molecules with respect to Nuchar RGC30 activated carbon.

Thermodynamic adsorption results onto [Hmim][BF₄]-functionalized sorbents suggest that the impregnation of micro and micro-mesoporous activated carbons with this IL (a physical solvent for CO₂) is not suitable for CO₂ removal from flue-gas (at least under the investigated impregnation conditions), because the active phase contribution in the pollutant capture is not able to balance the reduction of the substrate adsorption performances induced by the pores obstruction, also at higher temperatures. Conversely, the functionalization of both activated carbons with a more CO₂ chemically-affine IL (i.e. [Emim][Gly]) under more diluted impregnation condition can ameliorate the parent carbons CO₂ adsorption

performances at 80°C and for a typical 15% CO₂ flue-gas stream (while pores blocking is dominant at 30°C) thanks to a good compromise between IL loading and pore accessibility (low pore volume reduction). Nevertheless, the improvement in CO₂ adsorption capacity determined by [Emim][Gly] is still not adequate for the potential application of these materials in large-scale flue-gas purification systems.

Dynamic adsorption results on the investigated sorbents highlighted the important role played by both a greater contribution of mesopores and the presence of wider micropores for Nuchar RGC30-based materials in determining faster capture kinetics with respect to Filtrasorb 400 sorbents, in particular at low temperature. As the temperature increases the reduced differences in adsorption capacity coupled with the increase in intraparticle diffusivity make the two classes of sorbents kinetically equivalent in the purification process. Furthermore, modelling analysis of breakthrough curves allowed identifying micropore diffusion as the rate-determining step of CO₂ adsorption, for almost all the analysed systems.

Preliminary regeneration studies on raw Filtrasorb 400, which displayed the highest capture performances among all the adsorbents investigated, showed a complete regenerability of this sorbent under multiple adsorption/desorption cycles. Moreover, desorption experiments carried out on Filtrasorb 400 (after a solid saturation with a 15% CO₂ gas stream at 30°C) at different temperatures (60 °C and 100°C) and N₂ flow rates (6.95×10^{-3} L s⁻¹, 1.11×10^{-2} L s⁻¹, 1.39×10^{-2} L s⁻¹) evidenced that regeneration levels of 70 and 80% obtained at 100°C and adopting a 1.11×10^{-2} L s⁻¹ purge flow rate can be considered as the optimal solutions among those investigated, being a fair compromise between CO₂ concentration in the desorbing flow (46-48%) and time necessary to perform the recovery.

As a general consideration, the results obtained in this work encourage future research efforts in the field of porous activated carbons functionalization with amine-based ILs as a potential route to improve their CO₂ capture performances, in particular at high temperatures at which the parent material contribution is quite low to allow a cost-effective treatment of a real flue-gas. In this context, the choice of activated carbons characterized by larger mean pore diameters (i.e. mainly mesoporous) could be apt to favour a higher dispersion of the ionic liquid over the substrate surface avoiding the undesired pore clogging effect. The synergistic collaboration with research groups belonging to different fields of investigation (Chemical Engineering, Inorganic and Organic Chemistry) could be an important strategy to foster the development of highly CO₂-affine SILP materials and accelerate their applicability in post-combustion systems, aiming at the following goals: i) synthesis of amine-based ILs characterized by reduced molecular sizes to minimize potential pore blocking; ii)

development of new functionalization protocols, e.g. covalent tethering of the IL to the support surface which could be an interesting option for both minimizing the amount of active phase used, with consequent economic benefits, and avoiding the continuous redistribution of the liquid phase inside the sorbent pores induced by temperature variations; iii) adsorption tests in multicomponent systems including the presence of NO_x, SO₂ and water vapour; iv) dedicated tests using different reactor configurations (fluidized-bed, circulating fluidized beds etc.); v) regeneration studies aimed at maximizing CO₂ concentration in the desorbing flow (for subsequent storage of the pollutant) while minimizing energy requirements.

Bibliography

Abanades J.C. and Alvarez D., Conversion limits in the reaction of CO₂ with lime. *Energy & Fuels* 17 (2003) 308-315.

Abanades J.C., Rubin E.S. and Anthony E.J., Sorbent cost and performance in CO₂ capture systems. *Industrial & Engineering Chemistry Research* 43 (2004) 3462-3466.

An J. and Rosi N., Tuning MOF CO₂ adsorption properties via cation exchange. *Journal of the American Chemical Society* 132 (2010) 5578-5579.

Aroua M.K., Daud W.M.A.W., Yin C.Y. and Adinata D., Adsorption capacities of carbon dioxide, oxygen, nitrogen and methane on carbon molecular basket derived from polyethyleneimine impregnation on microporous palm shell activated carbon. *Separation and Purification Technology* 62 (2008) 609-613.

Balsamo M., Di Natale F., Erto A., Lancia A., Montagnaro F. and Santoro L., Arsenate removal from synthetic wastewater by adsorption onto fly ash. *Desalination* 263 (2010) 58-63.

Balsamo M., Di Natale F., Erto A., Lancia A., Montagnaro F. and Santoro L., Gasification of coal combustion ash for its reuse as adsorbent. *Fuel* 106 (2013) 147-151.

Bara J.E., Gabriel C.J., Hatakeyama E.S., Carlisle T.K., Lessmann S., Noble R.D. and Gin D.L., Improving CO₂ selectivity in polymerized room-temperature ionic liquid gas separation membranes through incorporation of polar substituents. *Journal of Membrane Science* 321 (2008) 3-7.

Bates E.D., Mayton R.D., Ntai I. and Davis Jr. J.H., CO₂ capture by a Task-Specific Ionic Liquid. *Journal of the American Chemical Society* 124 (2002) 926-927.

Belmabkhout Y. and Sayari A., Adsorption of CO₂ from dry gases on MCM-41 silica at ambient temperature and high pressure. 2: Adsorption of CO₂/N₂, CO₂/CH₄ and CO₂/H₂ binary mixtures. *Chemical Engineering Science* 64 (2009) 3729-3735.

Berlier K. and Frère M., Adsorption of CO₂ on activated carbon: simultaneous determination of integral heat and isotherm of adsorption. *Journal of Chemical & Engineering Data* 41 (1996) 1144-1148.

Blamey J., Anthony E.J., Wang J. and Fennel P.S., The calcium looping cycle for large scale CO₂ capture. *Progress in Energy and Combustion Science* 36 (2010) 260-279.

Boschetti A., Montagnaro F., Rienzo C. and Santoro L., A preliminary investigation on the use of organic ionic liquids as green solvents for acylation and oxidation reactions. *Journal of Cleaner Production* 15 (2007) 1797-1805.

Bourbigou H.O., Magna L. and Morvan D., Ionic liquids and catalysis: Recent progress from knowledge to applications. *Applied Catalysis A: General* 373 (2010) 1-56.

Brúder P. and Svendsen H.F., Capacity and kinetics of solvents for post-combustion CO₂ capture. *Energy Procedia* 23 (2012) 45-54.

Chakraborty A., Saha B.B., Koyama S. and Ng K.C., On the thermodynamic modeling of the isosteric heat of adsorption and comparison with experiments. *Applied Physics Letters* 89 (2006) 171901.

Chang F.Y., Chao K.J., Cheng H.H. and Tan C.S., Adsorption of CO₂ onto amine-grafted mesoporous silicas. *Separation and Purification Technology* 70 (2009) 87-95.

Chew T.L., Ahmad A.L. and Bathia S., Ordered mesoporous silica (OMS) as an adsorbent and membrane for separation of carbon dioxide (CO₂). *Advances in Colloid and Interface Science* 153 (2010) 43-57.

Choi S., Drese J.H. and Jones C.W., Adsorbent materials for carbon dioxide capture from large anthropogenic point sources. *ChemSusChem* 2 (2009) 796-854.

Coppola A., Montagnaro F., Salatino P. and Scala F., Attrition of limestone during fluidized bed calcium looping cycles for CO₂ capture. *Combustion Science and Technology* 184 (2012a) 929-941.

Coppola A., Montagnaro F., Salatino P. and Scala F., Fluidized bed calcium looping: The effect of SO₂ on sorbent attrition and CO₂ capture capacity. *Chemical Engineering Journal* 207-208 (2012b) 445-449.

Crosthwaite J.M., Muldoon M.J., Dixon J.N.K., Anderson J.L. and Brennecke J.F., Phase transition and decomposition temperatures, heat capacities and viscosities of pyridinium ionic liquids. *Journal of Chemical Thermodynamics* 37 (2005) 559-568.

Delgado J.A., Uguina M.A., Sotelo J.L. and Ruíz B., Fixed-bed adsorption of carbon dioxide-helium, nitrogen-helium and carbon dioxide-nitrogen mixtures onto silicalite pellets. *Separation and Purification Technology* 49 (2006) 91-100.

Devadas M., Ramalingam B., Ramesh K., Tasrif M. and Sharrat P., CO₂ capture by adsorption on mesoporous MCM-68 solid sorbent materials. 21st International Symposium on Chemical Reaction Engineering, Philadelphia, USA (2010).

Ding Y. and Alpay E., Equilibria and kinetics of CO₂ adsorption on hydrotalcite adsorbent. *Chemical Engineering Science* 55 (2000) 3461-3474.

Do D.D., Adsorption analysis: equilibria and kinetics. Series on Chemical Engineerings vol. 2, Imperial College Press (1998).

Do D.D. and Wang K., A new model for the description of adsorption kinetics in heterogeneous activated carbon. *Carbon* 36 (1998) 1539-1554.

Dubin M.M. and Radushkevich L.V., Equation of the characteristic curve of activated charcoal. Proceedings of the Academy of Sciences, Physical Chemistry Section, U.S.S.R 55 (1947) 331-333.

Eddaoudi M., Kim J., Rosi N., Vodak D., Wachter J., O'Keefe M. and Yaghi O., Systematic design of pore size and functionality in isoreticular MOFs and their application in methane storage. *Science* 295 (2002) 469-472.

Figuerola J.D., Fout T., Plasynski S., McIlvried H. and Srivastava R.D., Advances in CO₂ capture technology-The U.S. Department of Energy's Carbon Sequestration Program. *International Journal of Greenhouse Gas Control* 2 (2008) 9-20.

García S., Gil M.V., Martín C.F., Pis J.J., Rubiera F. and Pevida C., Breakthrough adsorption study of a commercial activated carbon for pre-combustion CO₂ capture. *Chemical Engineering Journal* 171 (2011) 549-556.

Gomes V.G. and Yee K.W.K., Pressure swing adsorption for carbon dioxide sequestration from exhaust gases. *Separation and Purification Technology* 28 (2002) 161-171.

Gray M.L, Soong Y., Champagne K.J., Pennline H., Baltrus J.P., Stevens Jr. R.W., Khatri R., Chuang S.S.C. and Filburn T., Improved immobilized carbon dioxide capture sorbents. *Fuel Processing Technology* 86 (2005) 1449-1455.

Hasib-ur-Rahman M., Sijaj M. and Larachi F., Ionic liquids for CO₂ capture-Development and progress. *Chemical Engineering and Processing* 49 (2010) 313-322.

Herzog H., Meldon J. and Hatton A., Advanced post-combustion CO₂ capture. Report prepared for the Clean Air Task Force (2009).

Hughes R.W., Lu D.Y., Anthony E.J. and Macchi A., Design, process simulation and construction of an atmospheric dual fluidized bed combustion system for in situ CO₂ capture using high-temperature sorbents. *Fuel Processing Technology* 86 (2005) 1523-1531.

Inglezakis V.J. and Pouloupoulos S.G., Adsorption, Ion Exchange and Catalysis. Design of operations and environmental application. Elsevier (2006).

International Energy Agency (IEA), Energy Technology Perspectives (2010). <http://www.iea.org/techno/etp/etp10/English.pdf>.

Jang H.T., Park Y.K., Ko Y.S., Lee J.Y. and Margandan B., Highly siliceous MCM-48 from rice husk ash for CO₂ adsorption. *International Journal of Greenhouse Gas Control* 3 (2009) 545-549.

Kanniche M., Gros-Bonnivard R., Jaud P., Valle-Marcos J., Amann J.M. and Bouallou C., Pre-combustion, post-combustion and oxy-combustion in thermal power plant for CO₂ capture. *Applied Thermal Engineering* 30 (2010) 53-62.

Kasahara S., Ishigami T and Matsuyama H., Amino acid ionic liquid-based facilitated transport membranes for CO₂ separation. *Chemical Communications* 48 (2012) 6903-6905.

Khalil S.H., Aroua M.K. and Daud W.M.A.W., Study on the improvement of the capacity of amine-impregnated commercial activated carbon beds for CO₂ adsorbing. *Chemical Engineering Journal* 183 (2012) 15-20.

- Kim Y.S., Choi W.Y., Jang J.H., Yoo K.P. and Lee C.S., Solubility measurement and prediction of carbon dioxide in ionic liquids. *Fluid Phase Equilibria* 228-229 (2005) 439-445.
- Kittel J., Idem R., Gelowitz D., Tontiwachwuthikul P., Parrain G. and Bonneau A., Corrosion in MEA units for CO₂ capture: pilot plant studies. *Energy Procedia* 1 (2009) 791-797.
- Kolding H., Fehrmann R. and Riisager A., CO₂ Capture technologies: Current status and new directions using supported ionic liquid phase (SILP) absorbers. *Science China Chemistry* 55 (2012) 1648-1656.
- Krumdieck S., Wallace J. and Curnow O., Compact, low energy CO₂ management using amine solution in a packed bubble column. *Chemical Engineering Journal* 135 (2008) 3-9.
- Krutyeva M., Grinberg F., Furtado F., Galvosas P., Kärger J., Silvestre-Albero A., Sepulveda-Escribano A., Silvestre-Albero J. and Rodríguez-Reinoso F., Characterization of carbon materials with the help of NMR methods. *Microporous and Mesoporous Materials* 120 (2009) 91-97.
- Lee Z.H., Lee T.K., Bhatia S. and Mohamed A.R., Post-combustion carbon dioxide capture: Evolution towards utilization of nanomaterials. *Renewable and Sustainable Energy Reviews* 16 (2012) 2599-2609.
- Lemus J., Palomar J., Gilarranz M.A. and Rodriguez J.J., Characterization of supported ionic liquid phase (SILP) materials prepared from different supports. *Adsorption* 17 (2011) 561-571.
- Leofanti G., Padovan M., Tozzola G. and Venturelli B., Surface area and pore texture of catalysts. *Catalysis Today* 41 (1998) 207-219.
- Li F. and Fan L.S., Clean coal conversion processes—progress and challenges. *Energy & Environmental Science* 1 (2008) 248-267.
- Lu C., Bai H., Wu B., Su F. and Hwang J.F., Comparative study of CO₂ capture by carbon nanotubes, activated carbons, and zeolites. *Energy & Fuels* 22 (2008) 3050-3056.
- Marsh H. and Rodríguez-Reinoso F., *Activated Carbon*. Elsevier Science & Technology Books (2006).
- McCabe W.L., Smith J.C. and Harriot P., *Unit Operations of Chemical Engineering*. McGraw-Hill 5th edition (1993).
- Metz B., Davidson O., de Coninck H., Loos M. and Meyer L., *International Panel on Climate Change (IPCC) Carbon dioxide capture and storage*. Cambridge University Press (2005).
- Montagnaro F., Salatino P. and Scala F., The influence of temperature on limestone sulfation and attrition under fluidized bed combustion conditions. *Experimental Thermal and Fluid Science* 34 (2010) 352-358.

Morlay C. and Joly J.P., Contribution to the textural characterization of Filtrasorb 400 and other commercial activated carbons commonly used for water treatment. *Journal of Porous Materials* 17 (2010) 535-543.

Muhammad N., Man Z.B., Bustam M.A., Mutalib M.I.A, Wilfred C.D. and Rafiq S., Synthesis and thermophysical properties of low viscosity amino acid-based ionic liquids. *Journal of Chemical & Engineering Data* 56 (2011) 3157-3162.

Na B.K., Koo K.K., Eum H.M., Lee H. and Song H.K., CO₂ recovery from flue gas by PSA process using activated carbon. *Korean Journal of Chemical Engineering* 18 (2001) 220-227.

Neimark A.V., Lin Y., Ravikovitch P.I and Thommes M., Quenched solid density functional theory and pore size analysis of micro-mesoporous carbons. *Carbon* 47 (2009) 1617-1628.

Patrick J.W., *Porosity in Carbons: Characterization and Applications*. Halsted Press (1995).

Perry R.H. and Green D.W., *Perry's Chemical Engineers' Handbook*. McGraw Hill, 7th edition (1997).

Plaza M.G., Pevida C., Arenillas A., Rubiera F. and Pis J.J., CO₂ capture by adsorption with nitrogen enriched carbons. *Fuel* 86 (2007) 2204-2212.

Plaza M.G., Pevida C., Arias B., Feroso J., CasaL M.D., Martin C.F., Rubiera F. and Pis J.J., Development of low-cost biomass-based adsorbents for postcombustion CO₂ capture. *Fuel* 88 (2009) 2442-2447.

Plaza M.G., Pevida C., Pis J.J. and Rubiera F., Evaluation of the cyclic capacity of low-cost adsorbent for post-combustion CO₂ capture. *Energy Procedia* 4 (2011) 1228-1234.

Polanyi M., Theories of the adsorption of gases. A general survey and some additional remarks. *Transaction of the Faraday Society* 28 (1932) 316-333.

Rege S.U. and Yang R.T., A novel FTIR method for studying mixed gas adsorption at low concentrations: H₂O and CO₂ on NaX zeolites and γ -alumina. *Chemical Engineering Science* 56 (2001) 3781-3796.

Roquerol J., Llewellyn P. and Rouquerol F., Is the BET equation applicable to microporous adsorbents?. *Studies in Surface Science and Catalysis* 160 (2007) 49-56.

Ruthven D.M., *Principles of adsorption and adsorption processes*. John Wiley & Sons (1984).

Saha B.B., Jribi S., Koyama S. and El-Sharkawy I.I., Carbon dioxide adsorption isotherms on activated carbons. *Journal of Chemical & Engineering Data* 56 (2011) 1974-1981.

Saha D., Bao Z., Jia F. and Deng S., Adsorption of CO₂, CH₄, N₂O and N₂ on MOF-5, MOF-177, and zeolite 5A. *Environmental Science & Technology* 44 (2010) 1820-1826.

Samanta A., Zhao A., Shimizu G.K.H., Sarkar P. and Gupta R., Post-combustion CO₂ capture using solid sorbents: A review. *Industrial & Engineering Chemistry Research* 51 (2012) 1438-1463.

- Sayari A., Belmabkhout Y. and Serna-Guerrero R., Flue gas treatment via CO₂ adsorption. *Chemical Engineering Journal* 171 (2011) 760-774.
- Serna-Guerrero R. and Sayari A., Modeling adsorption of CO₂ on amine-functionalized mesoporous silica. 2: Kinetics and breakthrough curves. *Chemical Engineering Journal* 161 (2010) 182-190.
- Shafeeyan M.S., Daud W.M.A.W., Houshmand A. and Shamiri A., A review on surface modification of activated carbon for carbon dioxide adsorption. *Journal of Analytical and Applied Pyrolysis* 89 (2010) 143-151.
- Shen C., Grande C.A., Li P., Yu J. and Rodrigues A.E., Adsorption equilibria and kinetics of CO₂ and N₂ on activated carbon beads. *Chemical Engineering Journal* 160 (2010) 398-407.
- Shen C., Yu J., Li P., Grande C.A. and Rodrigues A.E., Capture of CO₂ from flue gas by vacuum pressure swing adsorption using activated carbon beads. *Adsorption* 17 (2011) 179-188.
- Shim H.L., Udayakumar S., Yu J.I and Park D.W., Synthesis of cyclic carbonate from allyl glycidyl ether and carbon dioxide using ionic liquid-functionalized amorphous silica. *Catalysis Today* 148 (2009) 350-354.
- Silvestre-Albero J., Silvestre-Albero A., Rodríguez-Reinoso F. and Thommes M., Physical characterization of activated carbons with narrow microporosity by nitrogen (77.4 K), carbon dioxide (273 K) and argon (87.3 K) adsorption in combination with immersion calorimetry. *Carbon* 50 (2012) 3128-3133.
- Silvestre-Albero J., Whaby A., Sepúlveda-Escribano A., Martínez-Escandell M., Kaneko K. and Rodríguez-Reinoso F., Ultrahigh CO₂ adsorption capacity on carbon molecular sieves at room temperature. *Chemical Communications* 47 (2011) 6840-6842.
- Sjostrom S., Krutka H., Starns T. and Campbell T., Pilot test results of post-combustion CO₂ capture using solid sorbents. *Energy Procedia* 4 (2011) 1584-1592.
- Soriano A.N., Doma Jr. B.T. and Li M.H., Carbon dioxide solubility in some ionic liquids at moderate pressures. *Journal of the Taiwan Institute of Chemical Engineers* 40 (2009) 387-393.
- Strube R. and Manfrida G., CO₂ capture in coal-fired power plants-Impact on plant performance. *International Journal of Greenhouse Gas Control* 5 (2011) 710-726.
- Tanaka S., Kida K., Fujimoto H., Makino T and Miyake Y., Self-assembling imidazolium-based ionic liquids in rigid nanopores induces anomalous CO₂ adsorption at low pressure. *Langmuir* 27 (2011) 7991-7995.
- Tang J., Tang H., Sun W., Radosz M. and Shen Y., Poly(ionic liquid)s as new materials for CO₂ absorption. *Journal of Polymer Science: Part A: Polymer Chemistry* 43 (2005) 5477-5489.
- Tlili N., Grévillet G. and Vallières C., Carbon dioxide capture and recovery by means of TSA and/or VSA. *International Journal of Greenhouse Gas Control* 3 (2009) 519-527.

Udayakumar S., Raman V., Shim H.L. and Park D.W., Cycloaddition of carbon dioxide for commercially-imperative cyclic carbonates using ionic liquid-functionalized porous amorphous silica. *Applied Catalysis A: General* 368 (2009) 97-104.

Udayakumar S., Shim H.L., Raman V. and Park D.W., The complete optimization of ionic liquid-functionalized porous amorphous silica under one-pot synthesis conditions. *Microporous and Mesoporous Materials* 129 (2010) 149-155.

Wahby A., Silvestre-Albero J., Sepúlveda-Escribano A. and Rodríguez-Reinoso F., CO₂ adsorption on carbon molecular sieves. *Microporous and Mesoporous Materials* 164 (2012) 280-287.

Whaby A., Ramos-Fernández J.M., Martínez-Escandell M., Sepúlveda-Escribano A., Silvestre-Albero J. and Rodríguez-Reinoso F., High-surface-area carbon molecular sieves for selective CO₂ adsorption. *ChemSusChem* 3 (2010) 974-981.

Xue Z., Zhang Z., Han J., Chen Y. and Mu T., Carbon dioxide capture by a dual amino ionic liquid with amino-functionalized imidazolium cation and taurine anion. *International Journal of Greenhouse Gas Control* 5 (2011) 628-633.

Yang H., Xu Z., Fan M., Gupta R., Slimane R.B. and Bland A.E., Progress in carbon dioxide separation and capture: A review. *Journal of Environmental Sciences* 20 (2008) 14-27.

Yong Z., Mata V.G. and Rodrigues A.E., Adsorption of carbon dioxide on chemically modified high surface area carbon-based adsorbents at high temperature. *Adsorption* 7 (2001) 41-50.

Zhang J., Zhang S., Dong K., Zhang Y., Shen Y. and Lv X., Supported absorption of CO₂ by tetrabutylphosphonium amino acid ionic liquids. *Chemistry A European Journal* 12 (2006b) 4021-4026.

Zhang J., Sun J., Zhang X., Zhao Y. and Zhang S., The recent development of CO₂ fixation and conversion by ionic liquid. *Greenhouse Gases Science and Technology* 1 (2011) 142-159.

Zhang S., Chen Y., Li F., Lu X., Dai W. And Mori R., Fixation and conversion of CO₂ using ionic liquids. *Catalysis Today* 115 (2006a) 61-69.